TECHNISCHE UNIVERSITÄT MÜNCHEN

Institute for
Experimental Physics E21

Annual Report 2006

Annual Report 2006

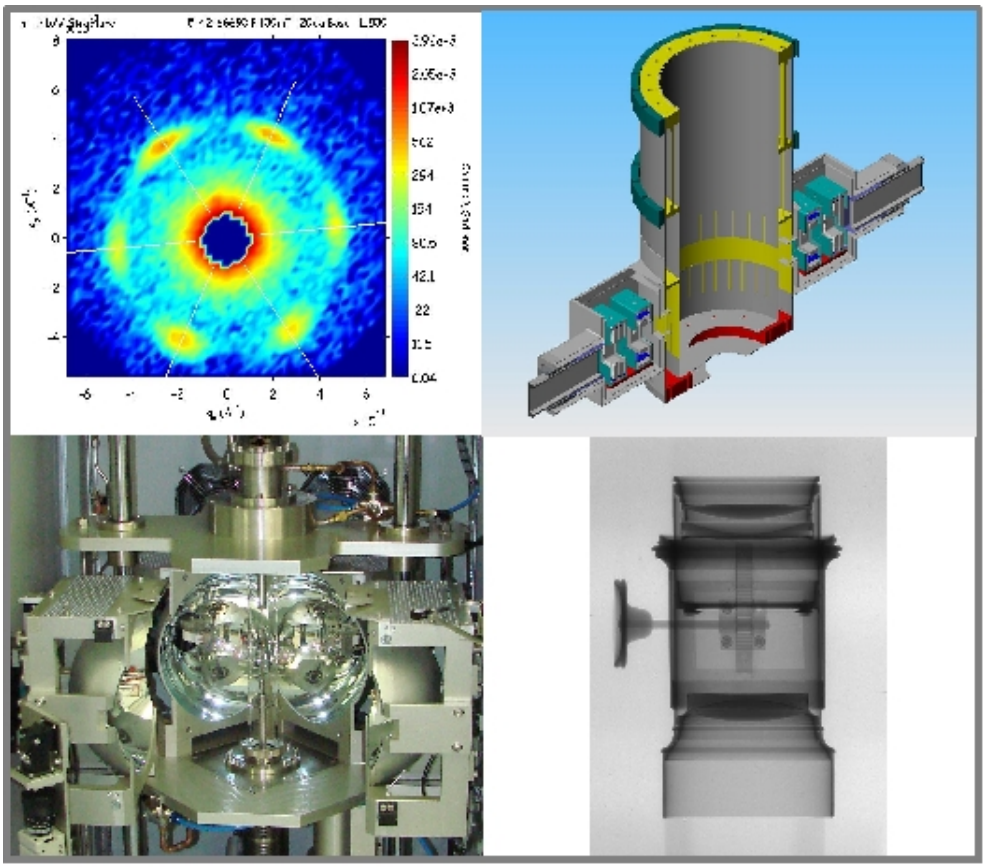

Cover page

Top/left:	Scattering pattern of the vortex lattice in Ta showing a hexagonal symmetry (section 1.7).
Top/right:	Cross section of MuPAD (section 6.2).
Bottom/left:	Central part of our ultra-high-vacuum image furnace for intermetallic compounds (section 6.10).
Bottom/right:	Neutron tomography of a camera lens, manufactured by Voigtländer & Sohn, Vienna (1860)(Deutsches Museum).

Annual Report 2006

of the Institute for Experimental Physics E21
Prof. Dr. P. Böni
Technical University Munich

Annual Report 2006
of the Institute for Experimental Physics E21
published: Jan. 2007
Layout by Nikolas Arend, Florian Grünauer, Stefan Legl
Edited by Stefan Legl
http://e21.frm2.tum.de

Technical University Munich
James-Franck-Straße
85747 Garching, Germany

Phone: +49-89-289-14711
Fax: +49-89-289-14713

Contents

Preface

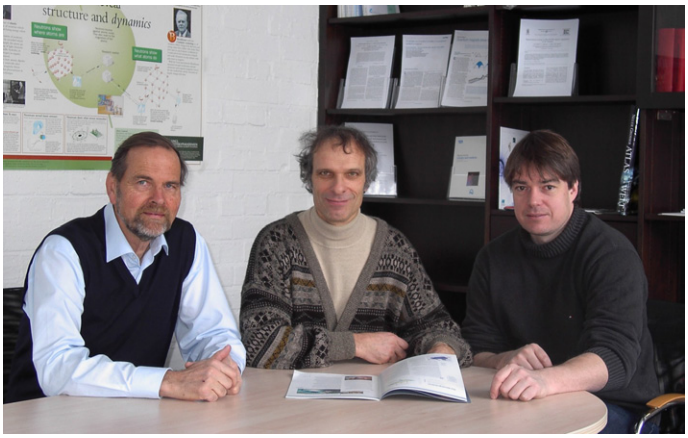

With this report we present a review of the activities at our institute in 2006. As in previous years the research areas covered at E21 remain highly diverse ranging from fundamental research on magnetic and superconducting materials, over applied physics and materials science to selected problems in particle physics. In all of these activities 2006 has been a highly rewarding year. At FRM-II the fourth beam line of E21, the neutron resonance spin echo spectrometer RESEDA, was taken into operation where first experiments resulted in beautiful data. The beam lines ANTARES and MIRA were running on schedule throughout the record 260 days of operation of FRM-II. Unfortunately operation of the world's most intense positron source, NEPOMUC, is still seriously hampered by magnetic stray fields when the 15 Tesla magnet is being used on PANDA.

At the Physik-Department major refurbishments of our new laboratories have been completed. Our 16 Tesla superconducting magnet system has been commissioned and experiments at ultra low temperatures are now running. Further, an image furnace was transferred from Karlsruhe to Munich and taken into operation for the preparation of metallic and oxide single crystals. On this occasion Christian Pfleiderer organized a joined DGKK and EU-CMA workshop on September 28 and 29, 2006 for an exchange of ideas and experiences of the leading groups in this field in Germany and Austria.

Many of the unique spin echo techniques that were developed in the past two decades starting at E21, as combined with our laboratory techniques, have already let to a number of exciting scientific results. Examples are ultra-precise measurements of the lattice constant of materials under extreme conditions, lifetime measurements of excitations in the μeV regime, and high-resolution measurements in magnetic fields using the MIEZE technique. Key results have been published in various journals including Nature and Physical Review Letters. We are grateful for being able to begin harvesting the tremendous efforts that were put into setting up the laboratories and beam lines.

Regarding the scientific staff at E21 we are very glad that PD Dr. Christoph Morkel joined E21 again after a long spell as deputy technical director of FRM-II. He greatly enjoys being back in science and looks forward to continuing his studies in the field of liquids.

Besides a large teaching load, where we cover first year experimental physics (C. Pfleiderer), condensed matter physics (P. Böni), reactor physics (K. Schreckenbach) and neutron physics (C. Morkel) six PhD and six diploma thesis have been completed during 2006. Several guest students from the USA and the UK have enjoyed extended stays at E21. We further contributed in various ways to the general activities of the Physik-Department, e.g., the Münchner Physik Kolloquium, the Festkörperkolloquium and the Girl's day. At FRM-II members of E21 guided the impressive number of about 140 officially registered tours.

Last but not least major social highlights during 2006 have been a day of skiing in St. Johann, Tyrol, a bicycle tour from Garching to lake Pulling followed by a visit of the beer garden at Weihenstephan in Freising, a visit at the Oktoberfest and a 'Klausabend' in December at our institute. This brings us to thank all of our collaborators and in particular the large number of young scientists at E21 for their enthusiasm and dedication and their efforts to maintain a very friendly and open atmosphere at our institute.

Garching, January 2007

Peter Böni Christian Pfleiderer Klaus Schreckenbach

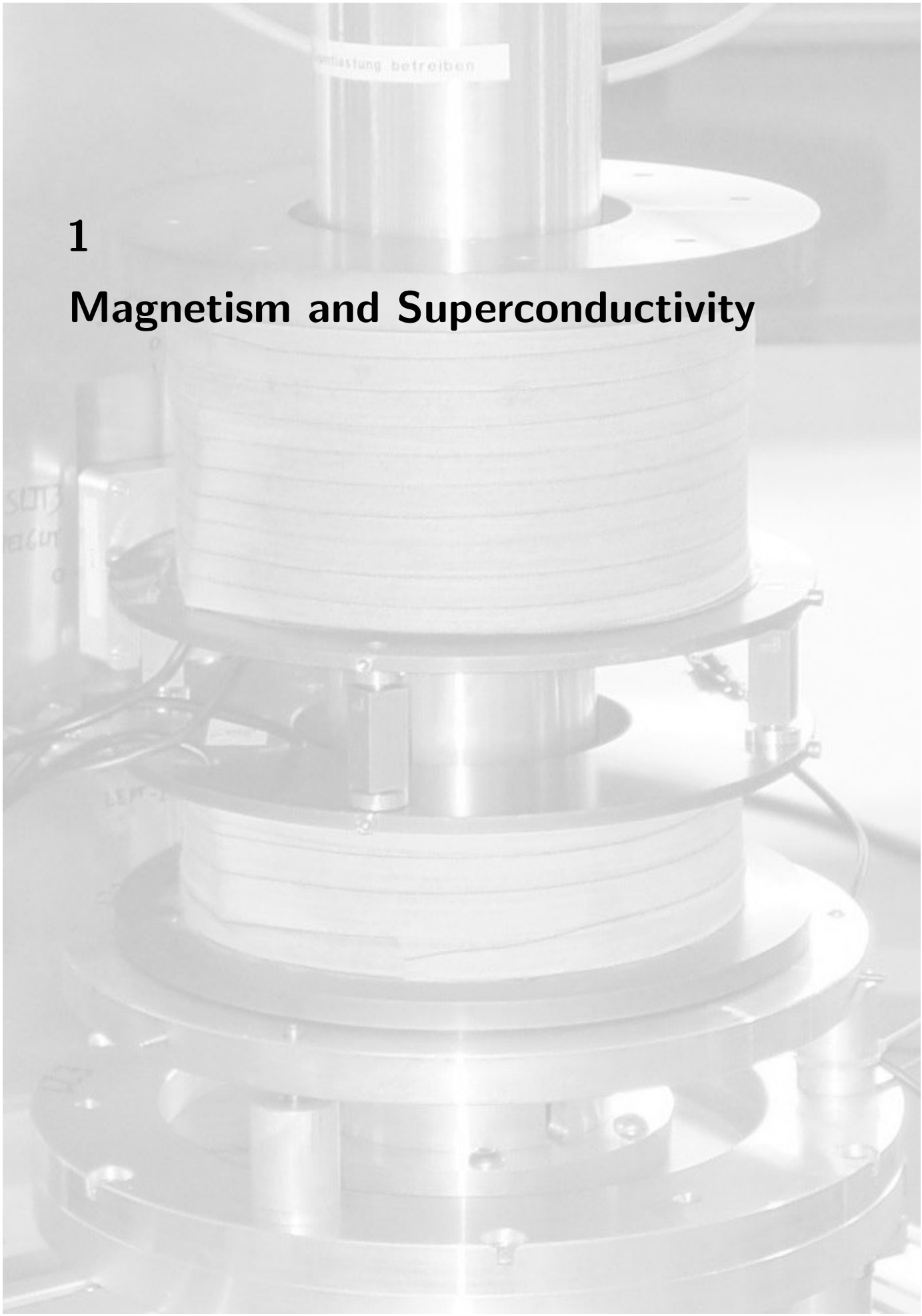

1

Magnetism and Superconductivity

1.1 Spontaneous skyrmion ground states in magnetic metals

U. K. Rößler [1], **A. Bogdanov** [1], **C. Pfleiderer** [2, 3, 4]
[1] *IFW Dresden, P.O. Box 270116, D–01171 Dresden, Germany*
[2] *Technische Universität München, Physics Department, Institute E21, D-85748 Garching, Germany*
[3] *Physikalisches Institut, Universität Karlsruhe, D-76128 Karlsruhe, Germany*
[4] *Forschungszentrum Karlsruhe, Institut für Festkörperphysik, D-76021 Karlsruhe, Germany*

Since the 1950s Heisenberg and others addressed the problem how to explain the appearance of countable particles in continuous fields [1]. Stable localized field configurations were searched as ingredient of a general field theory of elementary particles. As an exception Skyrme's model succeeded to describe nuclear particles as localized states, so-called 'skyrmions', within a non-linear field theory [2]. Skyrmions are a characteristic of non-linear continuum models ranging from microscopic to cosmological scales [3, 4, 5, 6]. Skyrmionic states have been found under non-equilibrium conditions, or when stabilised by external fields or the proliferation of topological defects. Examples are Turing patterns in classical liquids [7], spin textures in quantum Hall magnets [8], or the blue phases in liquid crystals [9], respectively. However, it is believed that skyrmions cannot form spontaneous ground states like ferromagnetic or antiferromagnetic order in magnetic materials.

We have shown theoretically [10] that this assumption is wrong and that skyrmion textures may form spontaneously in condensed matter systems with chiral interactions without the assistance of external fields or the proliferation of defects. We show this within a phenomenological continuum model, that is based on a few material-specific parameters that may be determined from experiment. As a new condition not considered before, we allow for softened amplitude variations of the magnetisation - a key property of, for instance, metallic magnets. Our model implies that spontaneous skyrmion lattice ground states may exist quite generally in a large number of materials, notably at surfaces and in thin films as well as in bulk compounds, where a lack of space inversion symmetry leads to chiral interactions. Illustrations are shown in Fig. 1 and Fig. 2.

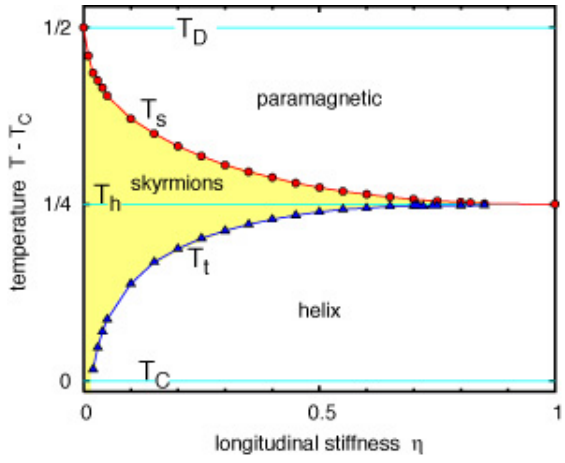

Figure 1: Phase diagram of a chiral ferromagnet in terms of temperature versus longitudinal stiffness-parameter (T, η). The diagram is based on the stability of cylindrical skyrmions (see Ref. [10] for further details).

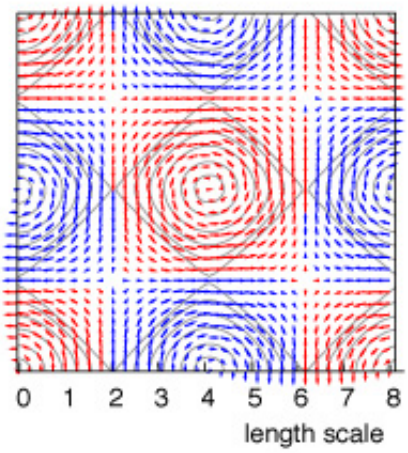

Figure 2: Structure of a two-dimensional skyrmion lattice, derived as minimum energy solution for our model. The ground-state has four-fold symmetric lattice structure, and net magnetization direction of the skyrmion cores is staggered. Red/blue signals local magnetization direction with positive/negative components arbitrarily taken perpendicular to the two-dimensional plane. For the core-regions of the skyrmions, lines of constant modulus, m =const, are shown as contour lines in the base-plane. This result applies to thin magnetic films with broken inversion symmetry made from isotropic or cubic (crystallographic class T) metallic materials.

References

[1] W. Heisenberg. *Einführung in die einheitliche Feldtheorie der Elementarteilchen*. Hirzel, Stuttgart, 1967.
[2] T. H. Skyrme. A non-linear field theory. *Proc. Royal Soc. London, Ser. A*, 260:127–138, 1961.
[3] R. Durrer, M. Kunz, and A. Melchiorri. Cosmic structure formation with topological defects. *Phys. Rep.*, 364:1–81, 2002.
[4] C. Bäuerle, Yu. M. Bunkov, S. N. Fisher, H. Godfrin, and G. R. Pickett. Laboratory simulation of cosmic string formation in the early universe using superfluid ^{3}He. *Nature*, 382:332–334, 1996.
[5] L. Brey, H. A. Fertig, R. Cote, and A. H. MacDonald. Skyrme crystal in a two-dimensional electron gas. *Phys. Rev. Lett.*, 75:2562–2565, 1995.
[6] U. Al' Khawaja and H. T. C. Stoof. Skyrmions in a ferromagnetic Bose-Einstein condensate. *Nature*, 411:918–920, 2001.
[7] M. C. Cross and P. C. Hohenberg. Pattern formation outside of equilibrium. *Rev. Mod. Phys.*, 65:852–1112, 1993.
[8] S. L. Sondhi, A. Karlhede, S. A. Kivelson, and E. H. Rezayi. Skyrmions and the crossover from the integer to the fractional quantum hall effect at small zeeman energies. *Phys. Rev. B*, 47:16419–19426, 1993.
[9] D. C. Wright and N. D. Mermin. Crystalline liquids — the blue phases. *Rev. Mod. Phys.*, 61:385–432, 1989.
[10] U. K. R. Rößler, A. N. Bogdanov, and C. Pfleiderer. Spontaneous skyrmion ground states of magnetic metals. *Nature*, 442:797–800, 2006.

1.2 Pressure dependence of the magnetization of URu_2Si_2

C. Pfleiderer [1, 2, 3], **J. Mydosh** [4], **M Vojta** [5]
[1] *Technische Universität München, Physics Department, Institute E21, D-85748 Garching, Germany*
[2] *Physikalisches Institut, Universität Karlsruhe, D-76128 Karlsruhe, Germany*
[3] *Forschungszentrum Karlsruhe, Institut für Festkörperphysik, D-76021 Karlsruhe, Germany*
[4] *II. Physikalisches Institut, Universität zu Köln, Zülpicher Str. 77, 50937 Köln, Germany*
[5] *Institut für Theorie der Kondensierten Materie, Universität Karlsruhe, 76128 Karlsruhe, Germany*

The ground state of URu_2Si_2 changes from so-called hidden order (HO) to large-moment antiferromagnetism (LMAF) under hydrostatic pressure in excess of ∼14 kbar. We report the dc-magnetization $M(B, T, p)$ of URu_2Si_2 for magnetic fields B up to 12 T, temperatures T in the range 2 to 100 K, and pressure p up to 17 kbar [1]. Typical magnetization data for the tetragonal c-axis at ambient and high pressure are shown in Fig. 1. Characteristic scales such as the coherence temperature T^*, the transition temperature T_0, and the anisotropy in the magnetization depend only weakly on the applied pressure.

However, the discontinuity in $\partial M/\partial T$ at T_0, which measures the magnetocaloric effect, decreases nearly 50% up to 17 kbar for M and B parallel to the tetragonal c-axis, while it increases 15-fold for the a-axis. Key features of the pressure dependence of the magnetization are summarized in Fig. 2. Our findings suggest that the HO and LMAF phases have an astonishing degree of similarity in their physical properties, but a key difference is the magnetocaloric effect near T_0 in the basal plane.

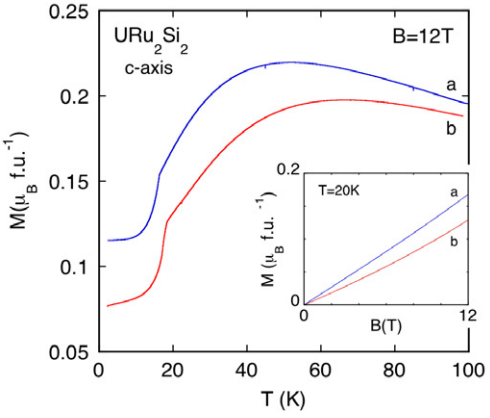

Figure 1: Magnetization M of URu_2Si_2 versus temperature T in the range 2 to 100 K, for a field of $B = 12$ T applied along the tetragonal c-axis. (a) ambient pressure; (b) $p = 15.9$ kbar. The inset displays typical data of $M(B)$ for $T = 20$ K, where the nonlinearity in curve (b) is due to the suppression of T_0 under magnetic field.

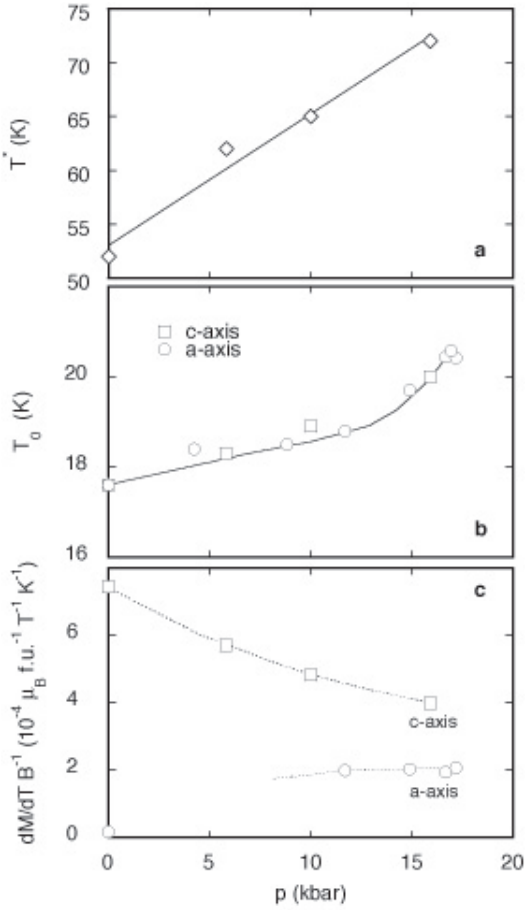

Figure 2: Pressure dependencies of the coherence temperature T^*, the transition temperature T_0, and the total height of the anomaly in $\partial M/\partial T$. Lines are guides to the eye. (a) The temperature T^* of the maximum in $M(T)$ increases nearly 30% under pressure up to ∼20 kbar. (b) The transition temperature T_0 increases weakly under pressure, with a pronounced change of slope around 14 kbar. The change of slope suggests that the border between HO and LMAF is crossed, and may be used to define $p_c \approx 14$ kbar. (c) The total height of the anomaly at T_0 seen in $\partial M/\partial T$. For the c-axis $\partial M/\partial T$ decreases by nearly 50%, while $\partial M/\partial T$ increases nearly 15-fold for the basal plane a-axis. It is interesting to note that the height of the anomaly $\partial M/\partial T$ for the a-axis is already maximal below the p_c and remains constant between 12 and 17 kbar. The data point for the a-axis at $p = 0$ was recorded without pressure cell.

References

[1] C. Pfleiderer, J. A. Mydosh, and Vojta M. Pressure dependence of the magnetization in uru2si2. *Phys. Rev. B*, 74:104412, 2006.

1.3 Study of the critical scattering in MnSi in the vincinity of T_C by means of Spherical Neutron Polarimetry (SNP)

M. Janoschek [1, 3], **R. Georgii** [1, 2], **C. Pfleiderer** [1], **P. Böni** [1]
[1] *Physics Department E21, Technical University Munich, 85747 Garching, Germany*
[2] *ZWE FRM-II, Technical University Munich, 85747 Garching, Germany*
[3] *Laboratory for Neutron Scattering ETHZ & PSI, CH-5232 Villigen PSI, Switzerland*

MnSi crystallises in the cubic space group $P2_13$ with the lattice parameter $a = 4.558$ Å. MnSi is an itinerant-electron ferromagnet with a Curie temperature T_C of about 29 K and an ordered magnetic moment of 0.4 μ_B on each Mn site. Its magnetic structure in zero field is a long-period ferromagnetic spiral with the propagation vector $(2\pi/a)(\zeta, \zeta\,\zeta)$ with $\zeta = 0.017$ resulting in a period of approximately 180 Å [1, 2] along the [111] direction.

MnSi attracts presently high interest due to the speculation about an intermediate phase between the helical and the paramagnetic phase that may be triggered by soft longitudinal fluctuations in MnSi. Roessler *et al.* [3] predict that the magnetic state may form skyrmion patterns in this phase, e.g. the pinning of the spiral is cancelled by the fluctuations. The skyrmion condensate may only be stable when a variation of amplitude of the magnetisation is allowed. This intermediate magnetic ground state should in principle be observable by means of *Spherical Neutron Polarimetry* (SNP) as this technique is very sensitive to changes in the magnetic structure [4, 5, 6].

For the experiment the MuPAD option [5, 6] was installed on the very cold neutron instrument MIRA. In this SNP setup we used MIRA in the small angle diffraction mode with a wavelength of 9.7 Å. The sample was adjusted on the instrument to fulfill the Bragg-condition on the magnetic satellite reflection (0.017, 0.017, 0.017). In order to have enough intensity to perform full polarization analysis in the vicinity of T_C we adjusted MIRA to use the full beam divergence thus sacrificing Q-resolution (Slit after monochromator 15mmx50mm, circular slit in front of the sample $\oslash = 13$ mm).

When the optimum crystal position was adjusted we started measuring the temperature dependence of all matrix elements of the polarization matrix (Fig. 1). A polarization value of about 83 % (s. e.g. Table 1) was observed on the xx, yx and zx terms of the matrix in the helical magnetic phase. This is due to the chiral term $i(\mathbf{M} \times \mathbf{M})$ that is generated by the anisotropic Dzyaloshinski-Moriya (DM) interaction [7, 8] arising from the non-central arrangement of the Mn moments in the unit cell. The chiral term additionally polarizes the neutron beam. All other terms are small and interpreted to be zero. This observation is a direct signature of a helical spin arrangement if the scattering vector $\mathbf{Q}$ is parallel to the propagation vector of the helix. However, when the temperature is increased through the transition temperature T_{c1} the three terms xx, yx and zx slowly start decreasing until they go to zero at approximately $T_{c2} = 31.5$ K. A similar decrease of the polarization of the neutrons was observed by Okorokov et al. [9] using longitudinal polarization analysis. The effect can be interpreted either in terms of a destabilization of the direction of the magnetic spirals or in terms of an intermediate phase. The latter scenario is more likely in the light of specific heat measurements performed on the same sample [10].

The measured diagonal elements of the polarization matrix using MuPAD are compatible with previous experiments with polarized neutrons using longitudinal polarization analysis. However, by considering the off-diagonal terms of the polarization matrix, new information concerning the proposition of an intermediate phase in MnSi by Rößler et al. [3] is made available that will be analyzed in more detail.

		Measurement			Theory		
P_{out}		x	y	z	x	y	z
P_{in}	x	0.836(7)	0.07(1)	0.09(1)	1	0	0
	y	0.880(1)	0.062(3)	0.091(3)	1	0	0
	z	0.880(1)	0.059(3)	0.083(3)	1	0	0

Table 1: Polarization matrix as measured at the magnetic satellite reflection (0.017 0.017 0.017) at $T \approx 20$ K is shown together with the expected matrix for the helical magnetic structure. The elements, where the x-component of the final polarization vector is measured are reduced from 1 due to the incomplete polarization of the neutron beam.

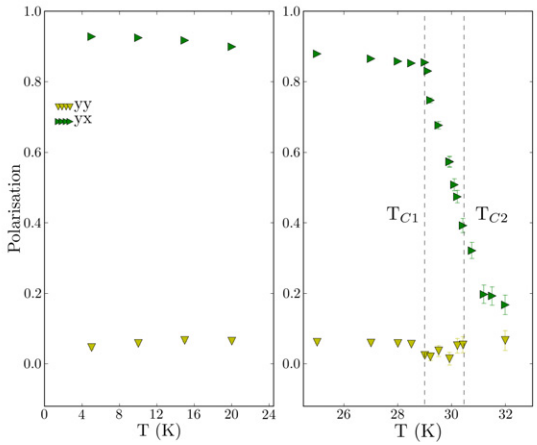

Figure 1: The temperature dependence of the matrix measured at the magnetic satellite reflection (0.017, 0.017, 0.017) is shown. Remarkable is the smooth transition from the helical phase below T_{c1} to the paramagnetic phase above T_{c2}. The T-dependence of the diagonal elements agrees qualitatively with previous measurements by Okorokov et al. [9] using longitudinal polarization analysis.

References

[1] G. Shirane, R. Cowley, C. Majkrzak, J.B. Sokoloff, B. Pagonis, C. H. Perry, and Y. Ishikawa. *Physical Review B*, 28(11), 1983.
[2] B. Roessli, P. Böni, W.E. Fischer, and Y. Endoh. *Phys. Rev. Lett.*, 88(23), 2002.
[3] U. K. Rößler, A. N. Bogdanov, and C. Pfleiderer. *Nature*, 442:797–801, 2006.
[4] F. Tasset. *Physica B*, 156-157:627, 1989.
[5] M. Janoschek. Master's thesis, Technical University Munich, http://mupad.wired-things.de, 2004.
[6] M. Janoschek, S. Klimko, B. Roessli, M. Medarde, and P. Böni. *Annual Report E21*, page 21, 2005.
[7] L. Dzyaloshinskii. *J. Phys. Chem Solids*, 4:241, 1958.
[8] T. Moriya. *Phys. Rev.*, 120:91, 1960.
[9] A. I. Okorokov et al. *Physica B*, 350, 2004.
[10] D. Lamago, R. Georgii, and P. Böni. *Physica B*, 359-361:1171, 2005.

1.4 Pressure dependence of the magnetization in ferromagnetic Pr_5Si_3

S. Legl [1], **C. Pfleiderer** [1], **D. Souptel** [2], **G. Behr** [2]
[1] *Technische Universität München, Physics Department, Institute E21, D-85748 Garching, Germany*
[2] *IFW Dresden, P.O. Box 270116, D–01171 Dresden, Germany*

Pr_5Si_3 is a rare example of a ferrromagnetic Pr-compound. It orders ferromagnetically below $T_c = 50\,\mathrm{K}$. The ferromagnetic state is strongly anisotropic, where the basal plane in the hexagonal crystal structure is the easy magnetic plane. We have measured the specific heat of single-crystals of Pr_5Si_3 with a PPMS-system at different static magnetic fields up to 9 T. The low temperature magnetization and DC-susceptibility under magnetic field up to 9 T, were measured with a vibrating sample magnetometer (VSM) at pressures up to 18 kbar, where non-magnetic miniature clamp type pressure cells were used as described in Ref. [1].

Fig. 1 shows the specific heat versus temperature at ambient field, $B = 5\,\mathrm{T}$ and $B = 9\,\mathrm{T}$ with the field parallel to the easy plane. A pronounced anomaly characteristic of a second order phase transition is observed. Magnetic field suppresses and shifts the entropy to higher temperatures. The behavior is that expected of a conventional ferromagnetic transition.

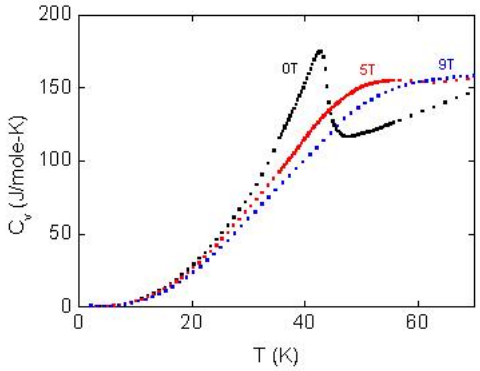

Figure 1: Specific heat versus temperature at selected magnetic fields applied parallel to the easy plane.

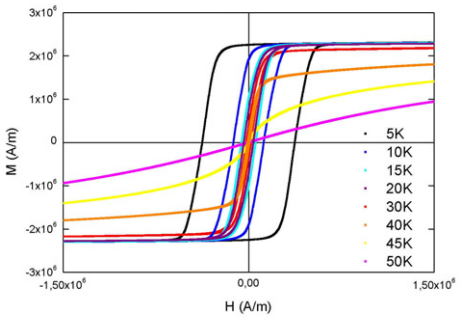

Figure 2: Magnetization as a function of magnetic field up to 2 T for various T.

Fig. 2 shows the magnetization as a function of magnetic field up to 2 T for various temperatures. The ordered magnetic moment of $2.2\,\mu_B/\mathrm{Pr}$ is consistent with [2]. Typical magnetization data under pressure are shown in fig. 3. Hysteresis loops were recorded at $T = 5\,\mathrm{K}$ for various pressures up to 18 kbar. While the ordered magnetic moment is essentially unchanged under pressure we observe the appearance of a shoulder with increasing pressure. This is consistent with a ferrimagnetic component that is stabilized under pressure. The inverse susceptibility versus temperature at $B = 0.1\,\mathrm{T}$ (not shown) follows a Curie-Weiss dependence above the Curie temperature with some deviations around 85 K that may be related to changes of pressure when the pressure transmitter (a methanol-ethanol mixture) freezes out. The effective Curie-Weiss moment of $3.87\,\mu_B/\mathrm{Pr}$ is consistent with [2].

The magnetization and DC-susceptibility identify PR_5Si_3 as a ferromagnetic Pr-compound with low T_c and reduced ordered moment. In specific heat measurements the pronounced thermodynamic transition is observed, with a weak field dependence. To search for a ferromagnetic quantum phase transitions in this compound very large pressures will be applied in the near future using a Bridgman anvil cell.

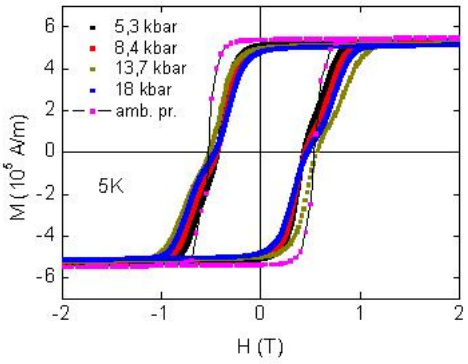

Figure 3: Magnetization as function of magnetic field up to 2 T at $T = 5\,\mathrm{K}$ for various pressures. Under application of pressure up to 18 kbar a shoulder emerges that suggests the stabilization of a ferrimagnetic component.

References

[1] C. Pfleiderer and A. Huxley. Pressure dependence of the magnetization in the ferromagnetic superconductor UGe_2. *Phys. Rev. Lett.*, 89:147005, 2002.
[2] D. Souptel et al. Floating zone growth and characterization of Pr_5Si_3 single crystals. *Journal of Crystal Growth*, 273:311–319, 2004.

1.5 Longitudinal Fluctuations in EuS

Detlef Görlitz [1], **Peter Böni** [2], **R. Georgii** [2, 3]
[1] *Institut für Angewandte Physik und Zentrum für Mikrostrukturforschung, Jungiusstr. 11, 20355 Hamburg*
[2] *Physics Department E21, Technische Universität München, 85747 Garching*
[3] *ZWE FRM-II, Technische Universität München, 85747 Garching*

The purpose of the SANS experiment was an investigation of the longitudinal and transverse magnetic fluctuations in a prototype Heisenberg ferromagnet EuS with respect to the magnetization (Fig. 1), in particular the influence of the dipolar interaction on the small angle scattering. We used a multi-platelet sample of EuS on MIRA.

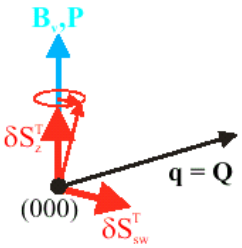

Figure 1: Scattering geometry for the SANS experiment. The magnetic field $\mathbf{B_v}$ is responsible for saturating the sample. The longitudinal fluctuations δS_z are given by the non spin flip scattering and the spin waves δS_{SW} by the spin flip cross section.

The neutron beam with a wavelength of 9.7 Å was vertically polarized. The sample was mounted in the closed cycle cryostat inside a room temperature bore of a Helmholtz magnet. The sample temperature was varied between 15 K and 90 K using a Lakeshore temperature controller. Below T_C= 16.4 K, at each temperature the magnet supplied a field strong enough to expel the domain walls in order to achieve a single domain state of homogeneous magnetization with a small internal field of the order of some 10 Oe. The neutron flight path between polarizer and cryostat as well as between cryostat and area detector was kept in a vertically guide field using permanent magnets in order to maintain the polarization of the neutrons. The polarization analysis of the scattered neutrons was performed utilizing a spin flipping device and a bender. An effective flipping ratio across the area detector of R = 11.6 was achieved. A typicla result is shown in Fig. 3.

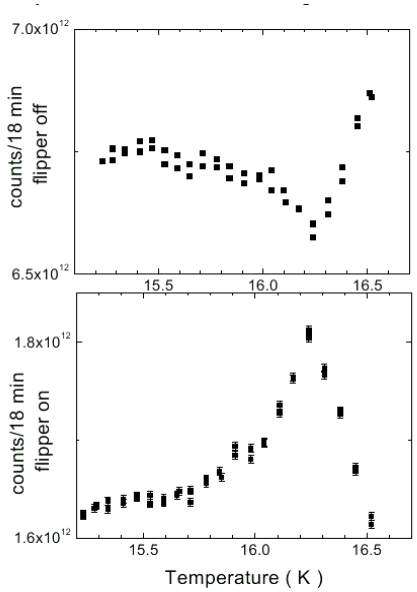

Figure 2: Temperature dependence of the integrated intensity of spin wave and longitudinal scattering in EuS. The data clearly exhibits the expected divergence near T_C.

We succeeded for the first time to separate the magnetic fluctuations in a SANS experiment into longitudinal and transverse excitations with respect to the sample magnetization. The integrated intensities as exemplified in Fig. 2 show the expected divergences at T_C. Please note, that the intensity of the direct beam has not been subtracted yet from the data. A remarkable and unexpected result is that the intensity of the longitudinal fluctuations is reduced when approaching T_C. This cannot be the result of multiple scattering often appearing in SANS experiments because this should be the same for the spin-flip and the non-spin-flip-channel. A reasonable explanation could be a different dynamics of longitudinal and transverse fluctuations. This issue is a topic of the detailed analysis of the data and further investigations.

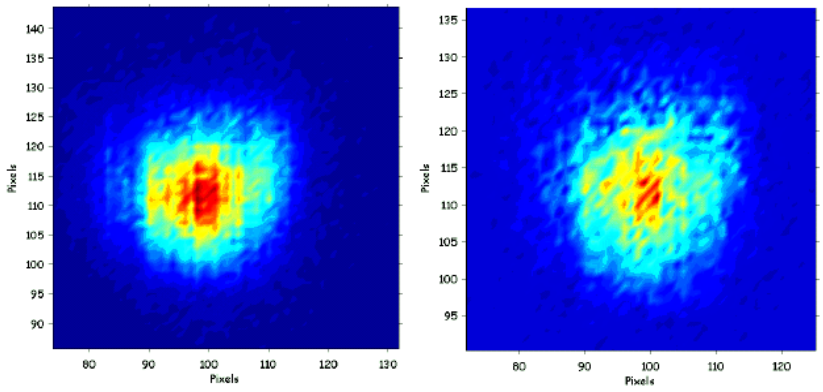

Figure 3: Example of SANS data as measured at 16.04 K just below T_C. The left and the right panel show the non- spin-flip and the spin flip data, respectively. Non-critical scattering at T=34 K has been subtracted already. The deconvolution of the instrument function is not performed yet.

1.6 Helical paramagnons in MnSi

Peter Böni [1], **Wolfgang Häussler** [1, 2], **Christian Pfleiderer** [1]
[1] *Physics Department E21, Technical University Munich, 85747 Garching, Germany*
[2] *ZWE FRM-II, Technical University Munich, 85747 Garching, Germany*

The cubic ferromagnet MnSi was considered to be one of the ideal realisations of a weak itinerant ferromagnet [1, 2], where the carriers of the magnetism are identified with the conduction electons. Ishikawa et al. have shown many years ago [3] that the critical magnetic scattering could indeed be interpreted in terms of a Fermi-liquid model predicting for the linewidth of the paramagnetic fluctuations

$$\Gamma = A_{it} q(q^2 + \kappa^2), \qquad (1)$$

where A_{it} is a diffusion constant, q the reduced momentum transfer and κ the inverse correlation length. However, the data was also compatible with the predictions of dynamical scaling theory, i.e.

$$\Gamma = A_{ds} f(\kappa/q) q^{2.5}, \qquad (2)$$

where $f(\kappa/q)$ is a dynamical scaling function. Although, Eq. 1 can also be cast into the form of a scaling function, the major difference between the two expressions is that in the picture of dynamical scaling, the critical fluctuations are included, while the itinerant picture is based on a mean field theory with enhanced long wavelength spin fluctuations [4].

It is well known that due to the lack of inversion symmetry in MnSi, a long wavelength spiral with a pitch of 180 Å develops below $T_C = 29.5$ K due to the Dzyaloshinski-Moriya interaction. The influence of the spiral could be neglected in the interpretation of the previous data by Ishikawa et al. [3] because he performed the experiments at rather large q values. However, as dynamical scaling is only valid for vanishing q and energy transfers, it is important to perform the neutron scattering experiments as close as possible to the magnetic Bragg peaks, i.e near the magnetic satellite positions.

We have investigated the life time of the magnetic fluctuations by means of the spin-echo spectrometer RESEDA at the FRM-II. RESEDA is particularly well suited for these experiments because it allows to perform measurements at very small q-values. Therefore, a velocity selector for the definition of the wavelength of the incident neutrons can be used leading to a gain in intensity of approximately a factor of 10 when compared with a cold triple-axis spectrometer. Indeed, the scattering by the magnetic satellites of MnSi was so strong that an absorber had to be used in order to prevent the neutron detector from saturation. We have used three different modes for covering the full dynamic range of RESEDA, namely the spin-echo mode, the resonance spin-echo mode and the resonance spin-echo mode with bootstrap coils [5].

Figure 1 shows the measured intermediate scattering function $S(q,t)$ of paramagnetic scattering as measured at 4 different q-values at $T = 31$ K. The lifetime of the critical fluctuations decreases with increasing q-values when measured with respect to the magnetic Bragg peak.

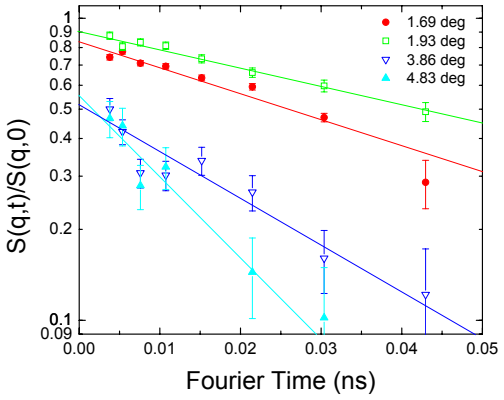

Figure 1: Intermediate scattering functions for scattering angles of 1.69^0, 1.93^0, 3.86^0, and 4.83^0 as measured at $T = 31$ K. The slope of the lines increases with increasing scattering angle.

The q-dependence of the measured linewidth Γ is shown in Fig. 2. The accuracy of the date corresponds roughly to the size of the symbols. All measured values are smaller than the data reported by Ishikawa et al. [3]. There is a hint that Γ increases again for $q < k$ ($k = 2\pi/180$ Å^{-1}) indicating that the slowest dynamics is indeed concentrated on the ring of scattering with a diameter $|k|$ that appears due to the pronounced softening of the helimagnons propagating transverse and perpendicular to the wavevector $\mathbf{k}$ of the spiral [6, 7].

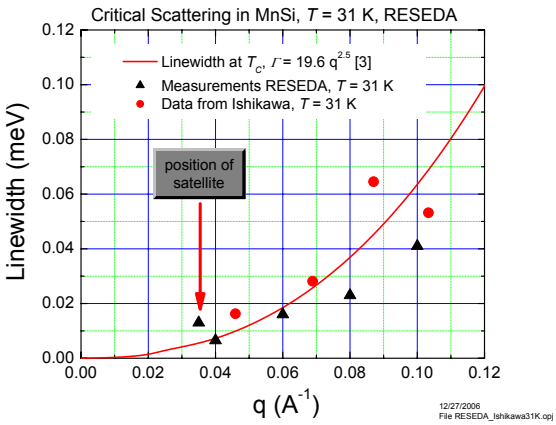

Figure 2: Wavevector dependence of the helical paramagnons in MnSi as measured at $T = 31$ K. The filled circles and the solid line show the data from Ishikawa et al. [3]. The new high-resolution data indicates that the linewidth is smaller than the data using a cold-triple axis spectrometer.

References

[1] T. Moriya. Spin fluctuations in itinerant electron magnetism. *Springer, Berlin, 1985*, 1985.
[2] G. G. Lonzarich and L. Taillefer. *J. Phys. C*, 18:4339, 1985.
[3] Y. Ishikawa, Y. Noda, Y. J. Uemura, C. F. Majrkzak, and G. Shirane. *Phys. Rev. B*, 31:5884, 1985.
[4] Y. Endoh and P. Böni. *J. Phys. Soc. Jpn.*, 75:111002, 2006.
[5] Thomas Keller, Robert Golub, and Roland Gähler. In *Scattering and Inverse Scattering in Pure and Applied Science*, pages 1264–86. Academic Press, San Diego, CA, 2002.
[6] T. R. Kirkpatrick and D. Belitz. *Phys. Rev. B*, 72:180402(R), 2005.
[7] S. V. Maleyev. *Phys. Rev. B*, 73:174402, 2006.

1.7 Vortex lattice structures in superconductors

Sebastian Mühlbauer [1], **Peter Böni** [1], **Christian Pfleiderer** [1], **Robert Georgii** [1, 2], **E. M. Forgan** [3], **M. Laver** [3], **E. Bauer** [4], **M.B. Maple** [5]

[1] *Technische Universität München, Physics Department E21, D-85747 Garching, Germany*
[2] *ZWE FRM-II, Technische Universität München, D-85747 Garching, Germany*
[3] *School of Physics and Astronomy, Condensed Matter Group, Birmingham, UK*
[4] *Institut für Festkörperphysik, Technische Universität Wien, Austria*
[5] *Physics/IPAPS – 0319, University of California, USA*

Small angle neutron scattering (SANS) directly maps the vortex lattice (VL) of a superconductor, revealing both individual sample properties as i.e. pinning potentials and purity - but also reflecting the symmetry of the underlying Fermi-surface as well as the symmetry of the superconducting wavefunction ψ. Especially in high-T_c and heavy-fermion superconductors, the symmetry of ψ is of great interest to figure out recent questions on the pairing mechanism in these compounds, which might be of so called unconventional nature. As the symmetry of the VL is influenced by possible anisotropies of the underlying Fermi-surface, possible non-local corrections to the free energy and ψ itself, classical superconductors are recently reinvestigated as model systems, where certain parameters can be tuned precisely.

Vortex structures in Niobium

Niobium (Nb) is a classical type-II superconductor, characterized with a Ginzburg-Landau parameter $\kappa = 0.8$. With the magnetic field applied along the four-fold (100) direction, a variety of VL symmetries is observed, namely a high-field and low-field square, a scalene and isosceles phase, all breaking the crystal symmetry [1]. These symmetries may be explained by non local corrections to the Eilenberger [2] equations in the form of $\cos 4\phi$ [3], leading to two separated square phases and additionally $\cos 8\phi$, allowing the VL symmetry breaking the crystal symmetry. Measurements on a pure Nb sample have also been performed on the diffractometer MIRA, an example is shown in Fig. 1.

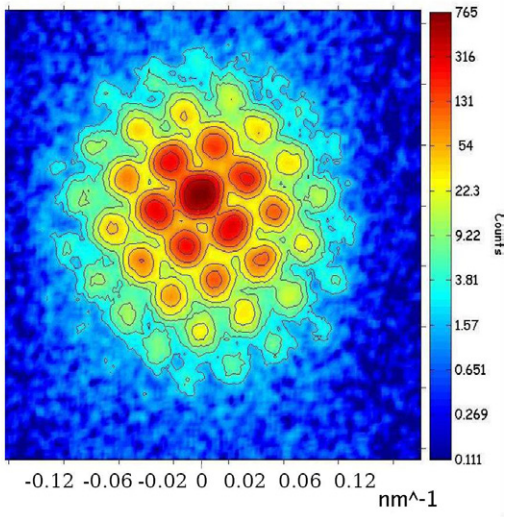

Figure 1: Scattering pattern of the VL in Nb, showing the fourier transform of the magnetic field distribution. A distorted sixfold symmetry is observed in 120 mT 2.9 K

Polarised small angle neutron scattering on Niobium

Polarised neutron scattering on a VL is restrained by the sample environment magnetic field, forcing the neutron spin parallel to the VL direction. This leads to a spin independent scattering intensity and no signal in the spin-flip channels. Due to the height of the magnetic potential of a single vortex, no Zeemann splitting is observed. But measurements, performed on the instrument SANS 2 at GKSS and on MIRA show a clear polarisation dependency in the VL Bragg peaks. The signal is clearly related to the onset of superconductivity, as shown in Fig. 2. As expected, no spin-flip signal is observed, ruling out strange VL spaghetti structures causing the polarisation dependence. Further measurements by E. M. Forgan [4] show a major purity dependence of the observed polarisation dependent signal, leading to the assumption that this effect may be caused by interference between nuclear scattering from impurities, which is spin independent, and magnetic scattering from the VL, which is spin dependent. As the VL is pinned by impurities and therefore distorted, a spatial correlation between some impurities and the VL positions may exist.

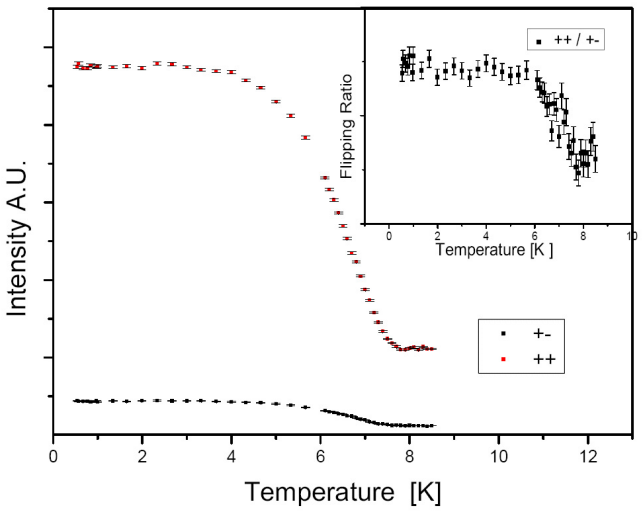

Figure 2: Integrated intensity of a VL Bragg peak. The $++$ and the $+-$ channel is shown as a function of temperature. The inset shows the ratio $++/+-$.

Vortex structures in Vanadium and Tantalum

Vanadium (V) and Tantalum (Ta) share the same valency with Niobium. Both also show superconductivity below 5.2 K and 4.42 K respectively. V is a type II superconductor, in Ta a type I/II transition is induced by doping with Nitrogen. Furthermore, both materials share large incoherent and absorption cross-sections, allowing only small samples. This is leading to a small signal. To observe a VL in these materials, the high flux instrument D 11 at ILL was used to map the phase diagram of V and Ta with the field also applied along

a four-fold (100) crystal symmetry axis. The VL in Ta was observed for the fist time by means of SANS. Preliminary results are shown in Fig. 3, Fig. 4 and Fig. 5, also showing a high field square VL phase for Va. Further data analysis will follow soon.

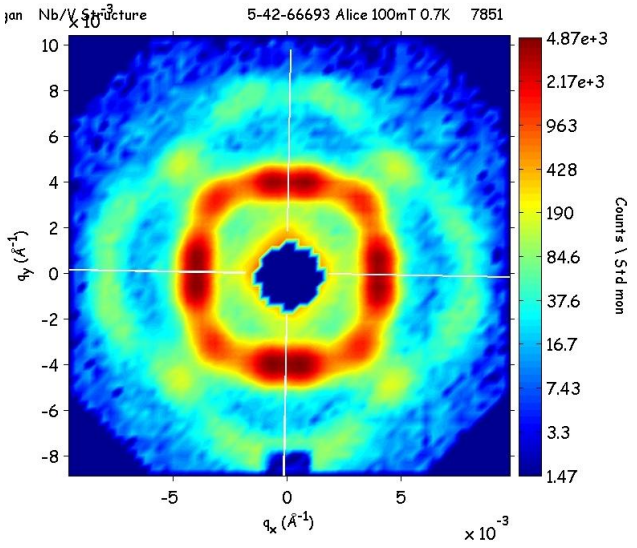

Figure 3: Scattering pattern of the VL in V, 0.7 K, 100 mT, showing a possible distorted hexagonal VL symmetry.

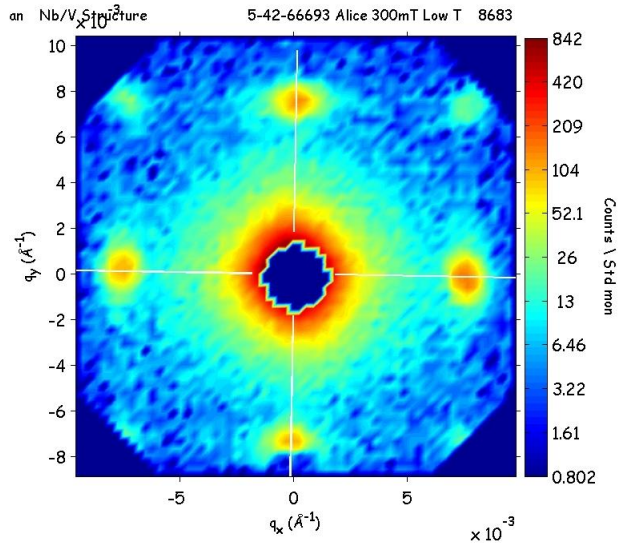

Figure 4: Scattering pattern of the VL in V, 0.7 K, 300 mT, showing a square VL symmetry.

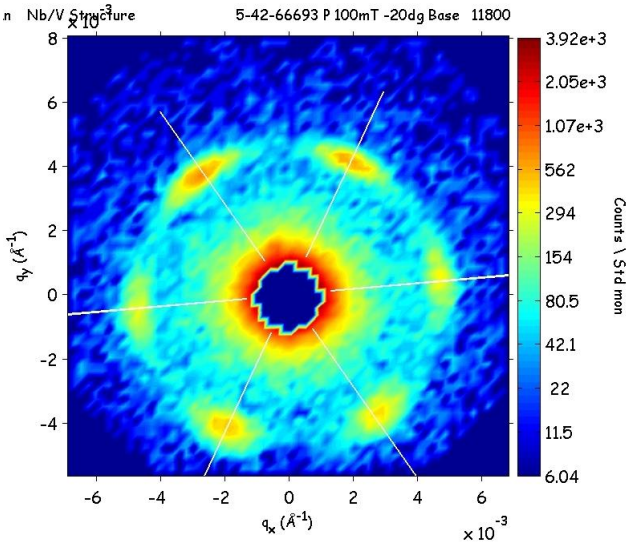

Figure 5: Scattering pattern of the VL in Ta, 0.7 K, 100 mT, showing a hexagonal VL symmetry.

Heavy fermion superconductors $Pr(Os_xRu_{1-x})_4Sb_{12}$, $CePt_3Si$

First measurements on the heavy-fermion superconductor $Pr(Os_xRu_{1-x})_4Sb_{12}$ - where conventional superconductivity in $PrRu_4Sb_{12}$ [5] and unconventional superconductivity in $PrOs_4Sb_{12}$ has been reported [6], have been performed on the spectrometer MIRA in order to study the evolution of unconventional superconductivity. Due to the long London penetration depth of these compounds, no signal of a VL could be observed yet.

The heavy-fermion superconductor $CePt_3Si$, shows both AF order and superconductivity under ambient pressure. The Pauli-Clogston limit for H_{c2} is exceeded substantially, leading to possible spin triplet pairing in this compound. The lack of inversion symmetry in $CePt_3Si$ is supposed to allow spin triplet pairing only if $d(k) = \hat{y}k_x - \hat{x}k_y$ [7]. A further consequence of the missing inversion symmetry is the prediction of a possible chiral structure of the mixed state. In order to observe a VL in $CePt_3Si$, measurements were performed to the Instrument D 22 at ILL:

Due to a strong field and temperature dependent background scattering (Fig. 6), possibly caused by distorted AF planes, locked along the crystal axes, no VL signal could be observed yet.

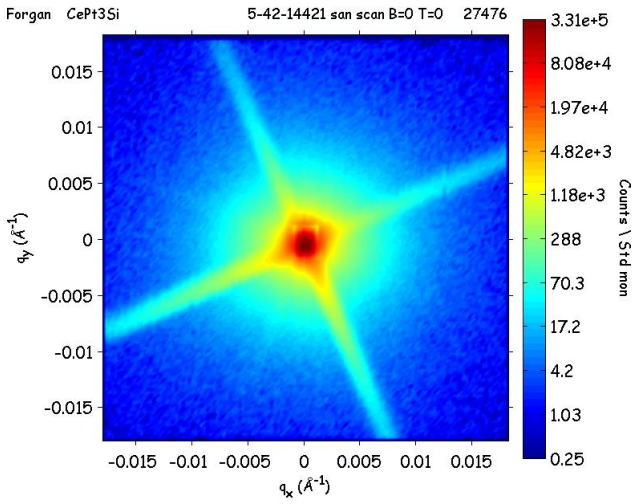

Figure 6: Background scattering in $CePt_3Si$, caused by distorted AF planes, locked along the crystal axes.

This work was partial supported by the European Union within the COST programme COST-STSM-P16-02280.

References

[1] M. Laver et al. Spontaneous symmetry breaking vortex lattice transitions in pure niobium. *Phys. Rev. Lett*, **96, 2006.**

[2] G. Eilenberger. *Z. Phys*, **214:195, 1968.**

[3] N. Nakai et al. 2002.

[4] E. M. Forgan. Investigation of flux line lattices by sans with unpolarized and polarized neutrons. *PNCMI conference proceedings, in press*, 2006.

[5] M. B. Maple et al. *J. Phys. Soc. Jpn*, 71:23, 2002.

[6] A. D. Huxley. *Phys. Rev. Lett.*, 93:187005, 2004.

[7] E. Bauer et al. *Phys. Rev. Lett.*, 92:027003, 2004.

1.8 Hall effect and magnetoresistance in MnSi

A. Neubauer [1], **C. Pfleiderer** [1], **P. Niklowitz** [1], **P. Böni** [1]
[1] *Technische Universität München, Physics Department E21, D-85748 Garching, Germany*

The intermetallic compound MnSi crystallizes in a non centro-symmetric cubic B20 structure with a lattice parameter of 4.58 Å. It orders magnetically at $T_c = 29.5$ K. The magnetic state is characterized by a helical modulation with a period of 180 Å along the $\langle 111 \rangle$ space diagonal in zero magnetic field. This alignment along $\langle 111 \rangle$ breaks up at an external field of 0.1 T and the helices start turning into field direction. Above 0.6 T the helical order is suppressed and a field induced ferromagnetic state is realized. Above T_c the magnetic susceptibility follows a Currie - Weiss dependence, where the spontaneous magnetic moment ($T \to 0$) $\mu_s = 0.4\mu_B$/Mn is much smaller than the effective Curie - Weiss moment $\mu_{eff} = 2.2\mu_B$/Mn in the paramagnetic region. This identifies MnSi as a typical weak itinerant-electron magnet.

In recent years MnSi has been the subject of great experimental and theoretical interest. The temperature dependence of the electrical resistivity suggests the emergences of an extended non-Fermi liquid (NFL) phase above $p_c = 14.6$ kbar [1, 2, 3]. Neutron scattering shows a partial magnetic order in a small pocket of the NFL phase [4]. An anomalous field dependence of the helical structure seen at ambient pressure near T_c [5] and the prediction of spontaneous skyrmion ground states at the border of helical order [6] may indicate certain similarities of the partial magnetic order and the properties near T_c at ambient pressure. This and the fact that the Hall effect in weakly magnetic metals has not been studied before let us to carry out a comprehensive study of Hall effect and magnetoresistance in MnSi [7]. Data were recorded in a standard 6 terminal configuration that allowed simultaneous measurement of ρ_{Hall} and ρ_{MR}. Measurements were performed in the temperature range 3 - 300 K at magnetic fields up to ± 9 T.

Figure 1(a) shows the field dependent Hall resistivity ρ_{xy} with an external magnetic field applied along the $\langle 110 \rangle$ direction. For temperatures around T_c there is an initial steep rise followed by a maximum around 0.7 T and an almost linear decrease. For low ($T < 10$ K) and high temperatures we see an almost linear decrease. The initial slope of the room temperature curve gives a value of $R_0 = -1,65 \cdot 10^{-2} \mu\Omega$cm/T for the normal Hall coefficient which is equivalent to a electron-like charge carrier density of $n \approx 3.78 \cdot 10^{22}$cm^{-3}. Figure 1(b) shows the magnetic field dependence of the longitudinal resistivity. For all temperatures there is a large and negative magnetoresistance with the maximum suppression around T_c. For temperatures $T < 30$ K two signatures (change of the slope) at around 0.1 T and 0.7 T can be seen, that coincide with the specific fields for the alignment and the breaking up of the helices. A complete account of this study is in preparation.

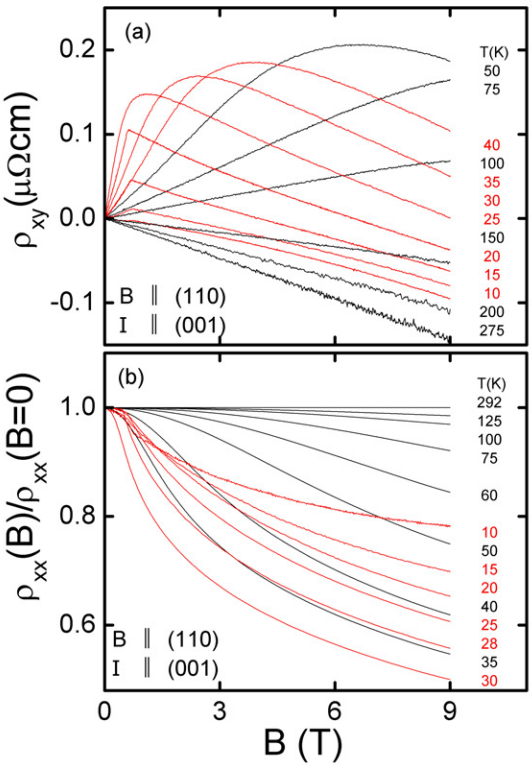

Figure 1: Field dependence of the specific Hall resistivity (a) and magnetoresistance (b) of MnSi for different temperatures.

References

[1] C. Pfleiderer, S. R. Julian, and G. G. Lonzarich. Non-Fermi liquid nature of the normal state of itinerant-electron ferromagnets. *Nature*, 414:427–430, 2001.

[2] C. Pfleiderer. The non-Fermi liquid puzzle of MnSi at high pressure. *Physica B*, 328:100–104, 2003.

[3] N. Doiron-Leyraud, I. R. Walker, L. Taillefer, M. J. Steiner, S. R. Julian, and G. G. Lonzarich. Fermi-liquid breakdown in the paramagnetic phase of a pure metal. *Nature*, 425:595–599, 2003.

[4] C. Pfleiderer, D. Reznik, L. Pintschovius, H. v. Löhneysen, M. Garst, and A. Rosch. Partial magnetic order in the non-Fermi liquid phase of MnSi. *Nature*, 427:227–230, 2004.

[5] D. Lamago, R. Georgii, C. Pfleiderer, and P. Böni. Magnetic-field induced instability in the A-phase of MnSi: Bulk and SANS measurements. *Physica B*, 385-386:385, 2006.

[6] U. K. Roessler, A. N. Bogdanov, and C. Pfleiderer. Spontaneous skyrmion ground states in magnetic metals. *Nature*, 442:797, 2006.

[7] A Neubauer. Hall-Effekt und Magnetwiderstand schwach magnetischer Metalle. Diplomarbeit, Technische Universität München, 2006.

1.9 Disentanglement of the low-energy excitations in Chromium

P. G. Niklowitz [1], **K. Hradil** [2, 3], **P. Böni** [1]
[1] *Physik Department E21, Technische Universität München, 85747 Garching, Germany*
[2] *Institut für Physikalische Chemie, Georg-August-Universität Göttingen, 37077 Göttingen, Germany*
[3] *ZWE FRM-II, Technische Universität München, 85747 Garching, Germany*

Elemental Cr provides an archetypal example of metallic antiferromagnetism. However, there are many open questions with respect to the phenomenology of the low-energy excitations. In this experiment we investigated, how many different types of low-energy excitations exist in the two magnetically ordered phases of elemental Cr.

Applying a magnetic field and then cooling through the Néel temperature T_N provides single-domain Cr (to which we refer from now on). Below $T_N = 311$ K, Cr (bcc, $a = 2.88$ Å) orders in a spin-density-wave phase with an incommensurate ordering wave vector $\vec{Q}_\pm = (1 \pm \Delta x, 0, 0)$ ($\Delta x \approx 0.045$).[1] The spin-density-wave phase is transversally polarised (TSDW) above $T_{sf} = 122$ K and longitudinally polarised (LSDW) below T_{sf}.[1] Prior to this experiment it was assumed that at least three types of magnetic excitations would exist in the TSDW phase: (i) very steeply dispersive excitations (spin-waves (SW)) around $\vec{Q}_\pm$,[1] (ii) so-called Fincher-Burke (FB) modes with a well-established excitation at (100) and 4 meV,[2, 3] which could be part of a less established set of excitations with a more moderate dispersion originating at $\vec{Q}_\pm$,[3] and (iii) 'new modes', which seem to originate at the crossing point of the FB modes and show a weak dispersion along [010].[4] In the LSDW phase only the SW excitations had been observed.

The reinvestigation of the low-energy excitations of Cr was carried out at the thermal triple-axis spectrometer PUMA at FRM-II. The final neutron energy was fixed at 2.66 Å^{-1} and the collimation of the neutron beam was chosen to be 60'-30'-30'-60'. A graphite filter was used to avoid higher-order contamination. The 26 g sample was 80% single domain. The sample was mounted on an Al holder and cooled in a closed-cycle cryostat.

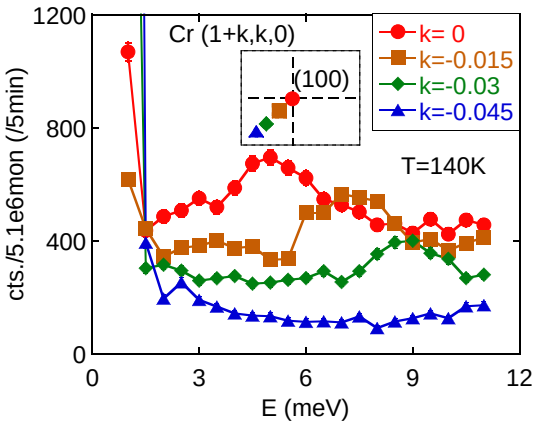

Figure 1: Fincher-Burke excitations around the (100) position.

First, we investigated whether the FB modes and the 'new modes' form in fact one set of excitations. This seemed possible, if one imagined, that the X-like dispersion of the FB modes along [100] through (100) is the cross section of two half cones originating in $\vec{Q}_\pm$. With this assumption the 'new modes' can be understood as a cross section along [010] through (100) of the same half cones. Therefore we performed a detailed set of E-scans from $\Delta E = 1$ meV to $\Delta E = 11$ meV in the rectangle in reciprocal space given by (1±0.045,0,0),(0,±0.06,0). As representative examples we show several energy scans taken at positions along a line in the [110] direction starting from (100) in reciprocal space (Figure 1). At the central (100) position the FB-mode is clearly visible as a broad peak with a maximum at 5 meV. Going away from the (100) position the peak shifts to higher energy and becomes weaker. The shift is strongest along the [100] direction and weakens along the [010] direction. The continuous change of the peak maximum in going through reciprocal space indicates that the 'new modes' are indeed part of the FB excitations. The observed peaks lie approximatively on the two half cones discussed above. However, peaks are only clearly resolved above 4 meV and the dispersion of the FB modes might be more complicated than initially assumed.

We also followed the temperature evolution of the FB-mode and found evidence for its existence in the LSDW phase.

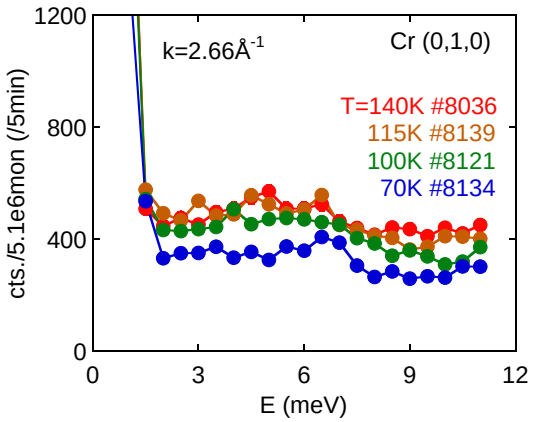

Figure 2: Fincher-Burke excitations at (010) at different temperatures. The excitations remain the LSDW phase. Inset: energy scans at 100 K.

Figure 2 shows the excitation at (010) which has been followed down to 70 K. With decreasing temperature the excitation are shifted to slightly higher energies. In the inset of Figure 2, for comparison, the energy scan at (100) at 100 K is shown, which does not contain any indication of a FB mode. This suggests that the FB mode maintains its longitudinal polarisation in the LSDW phase.

In conclusion, the low-energy excitations of Cr consist of spin-wave like excitations and the Fincher-Burke modes. Both types of excitations exist in both magnetically ordered phases.

References

[1] E. Fawcett. *Rev.Mod.Phys.*, 60:209, 1988.
[2] Jr. C. R. Fincher, G. Shirane, and S. A. Werner. *Phys. Rev. Lett.*, 43:1441, 1979.
[3] S. K. Burke, W. G. Stirling, K. R. A. Ziebeck, and J. G. Booth. *Phys. Rev. Lett.*, 51:494, 1983.
[4] H. Hiraka, Y. Endoh, P. Böni, M. Fujita, K. Yamada, and G. Shirane. *Phys. Rev. B*, 67:64423, 2003.

2

Multilayers and Interfaces

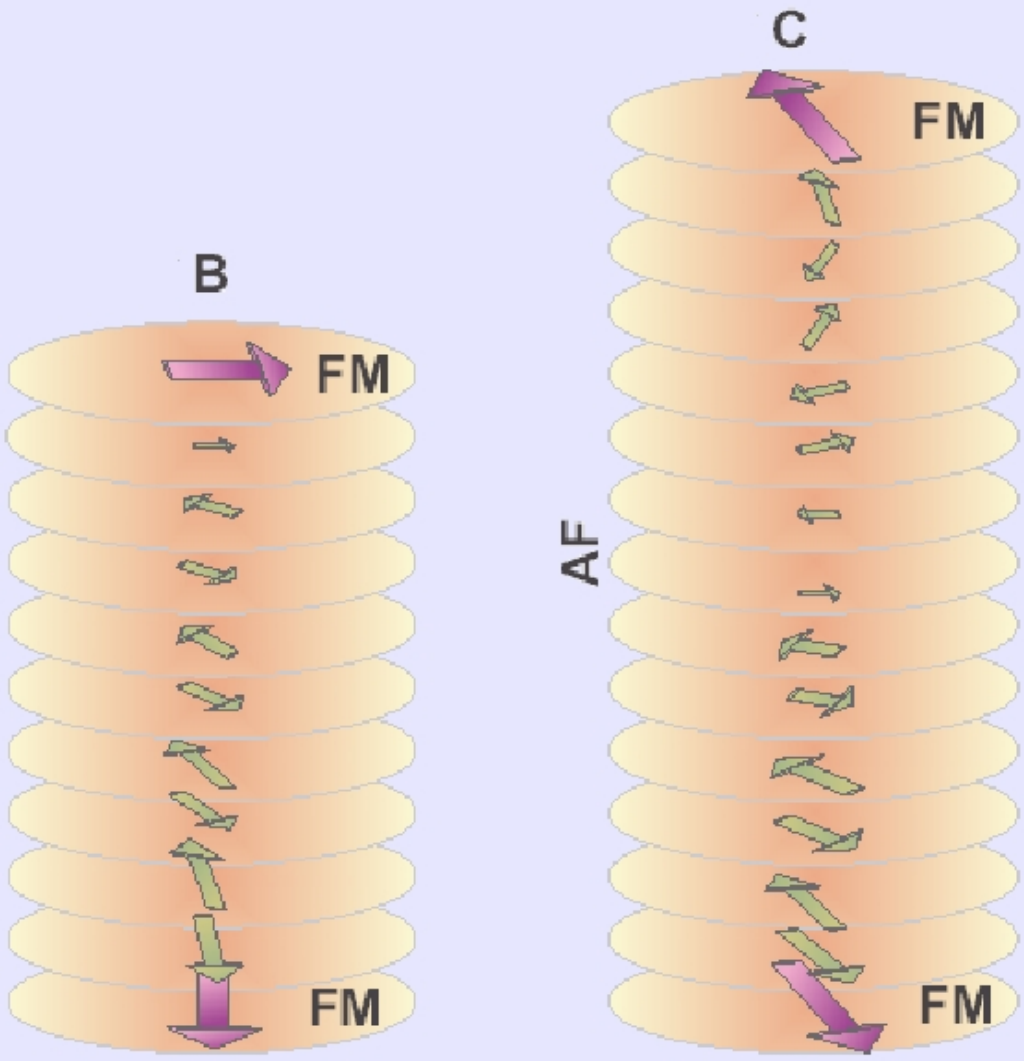

2.1 Measurement of the diffusion coefficient in amorphous $Pd_{40}Ni_{40}P_{20}$

Stefan Buschhorn [1], **Andreas Meyer** [2], **Robert Georgii** [3, 4]
[1] *Universität Göttingen, Göttingen, Germany*
[2] *Physics Department E13, Technische Universität München, 85747 Garching, Germany*
[3] *Physics Department E21, Technische Universität München, 85747 Garching, Germany*
[4] *ZWE FRM-II, Technische Universität München, 85747 Garching, Germany*

The aim of this experiment was to prepare neutron reflectometry measurements to determine the diffusion coefficient in amorphous $Pd_{40}Ni_{40}P_{20}$. $Pd_{40}Ni_{40}P_{20}$ is a massive bulk metallic glass former and a very good modell system to study transport mechanisms in glassy systems and undercooled melts. In a multilayer stack the Bragg peak intensity is expected to decrease with increasing annealing time, thus for each Bragg peak a diffusion coefficient can be determined.

As a first step [PdNiP/ZrAlCu] multilayer samples were prepared on a 2x4 cm^2 substrate to test the instrument geometry together with the sample holder and oven facility, which were used at MIRA for the first time. Figure 1 shows two [PdNiP/ZrAlCu] samples with ten and 15 periods, where the reflected intensity was collected for 240 and 10 seconds per step, respectively. The wavelength used was 10 Å, and in the plateau area the total intensity is about 1000 cps. The lines show first simulations of the reflectivity calculated with `Parratt32`, one data set is shifted for clarity.

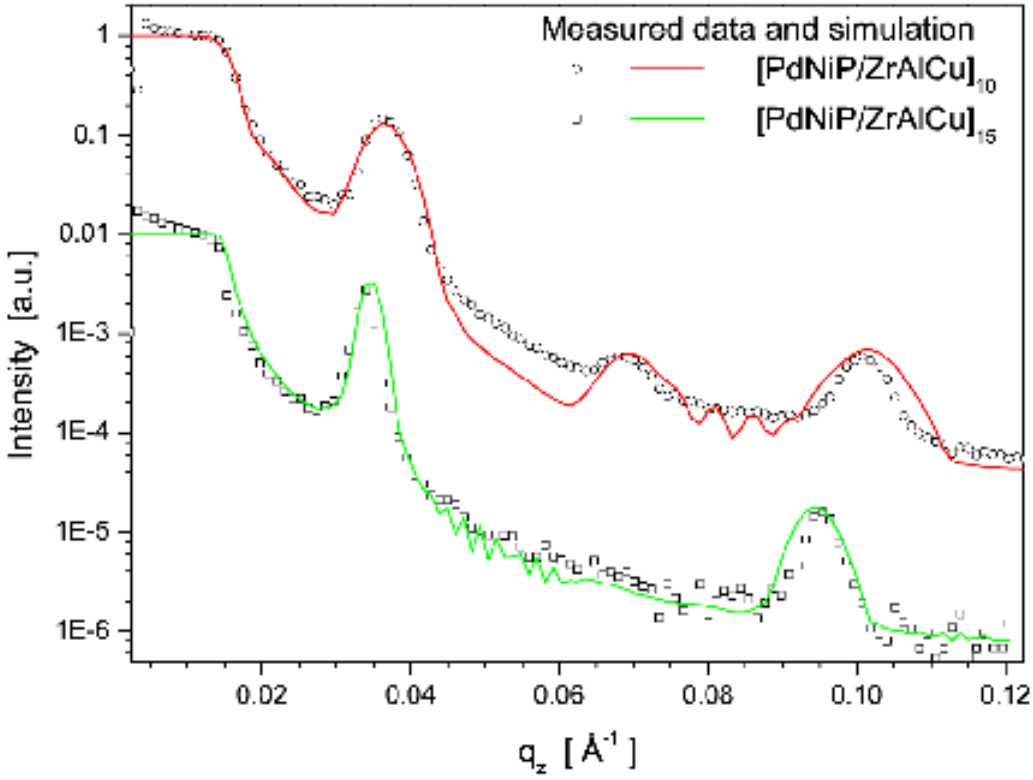

Figure 1: Reflectivity of two [PdNiP/ZrAlCu] samples, measured with $\lambda = 10$ Å.

A comparison shows a very good periodicity, especially in the case of 15 periods, where the even Bragg peaks vanish. The intensity of the first order Bragg peak is increased due to the higher number of layers, and no effects due to a possible change in the single layer thickness emerge. The simulated reflectivity gives an interface roughness of 9 Å. The simulations still have to be improved, but as a first result they confirm the homogeneity and periodicity of the multilayer structure. The samples can be prepared with a homogeneous thickness and low interface roughness on a 2x4 cm^2 substrate, but at $\lambda = 10$ Åthe accessible range in q-space is limited to ≈ 0.12 $Å^{-1}$, even if the counting rate is very long. Hence only the first and third order Bragg peak can be used to calculate a diffusion coefficient. The calculated contrast of [Pd^{60}NiP/Pd^{58}NiP] samples is increased compared to the used [PdNiP/ZrAlCu] multilayer system. Having done these first measurements, all technical aspects seem to be fixed now. With few minor changes and improvements of the experimental setup (at both MIRA and our sample holder) the resulting reflectivity data of [Pd^{60}NiP/Pd^{58}NiP] samples are expected to give a diffusion coefficient of Nickel in PdNiP. Thus it should in general be possible to determine diffusion coefficients via multilayer samples at MIRA.

2.2 Solvent content in thin spin-coated polymer films

J. Perlich [1], **V. Köstgens** [1], **L. Schulz** [1], **R. Georgii** [2, 3], **P. Müller-Buschbaum** [1]
[1] *Physics Department E13, Technische Universität München, 85747 Garching, Germany*
[2] *Physics Department E21, Technische Universität München, 85747 Garching, Germany*
[3] *ZWE FRM-II, Technische Universität München, 85747 Garching, Germany*

The detection of remaining solvent in thin polymer films is of importance due to its effect on chain mobility and film homogeneity. Moreover, it gives an estimate on possible aging effects caused by the reduction of the solvent content, which typically yield an increased brittleness. Here we use a well controlled model system, which consists of protonated polystyrene (PS) with different molecular weights Mw of 7, 27, 207, 514, 908, 1530 kg/mol, spin-coated out of protonated or deuterated toluene (solvent) onto silicon (Si) wafer substrates. Directly after spin-coating the thin PS films were investigated with neutron reflectivity (NR) at the MIRA instrument at a wavelength of 16 Å. A narrow q_z range (0 $Å^{-1}$ to 0.02 $Å^{-1}$) around the critical edge was probed with high resolution. The experiment focuses *on two different key parameters* which influence the solvent content: the molecular weight of PS and the film thickness investigated in the range of 10 to 100 nm. Focussing on the molecular weight, thin PS films with a fixed thickness of 50 nm are investigated: The expected shift of the critical edge position, which is observed in neutron reflectivity simulations on this model system, is verified by the MIRA measurements (Figure 1). In direct comparison the reflectivity of the sample prepared out of deuterated and protonated solvent is plotted. The data show a shift of the critical edge with increasing molecular weight, although the measured critical edges of much higher Mw shift not completely but rather indicate a slightly changed slope of the critical edge. For the investigation of the film thickness as the second key parameter, PS with a molecular weight of Mw = 207 kg/mol is dissolved in toluene-d8. The thickness of the thin PS film is depending on the viscosity of the solution and thus the concentration of PS in the solution. Therewith the concentration is chosen in such a way to achieve a desired film thickness. Figure 2 shows the obtained reflectivity data for films with thickness of 10, 30 and 100 nm at fixed molecular weight. The data of the critical edge indicate an influence on the film thickness, but prevent a definite conclusion about the behaviour in dependence of the film thickness without fitting the data. In summary, *the experiment was very successful*. A direct comparison indicates a clear distinction between thin films prepared of PS dissolved in protonated or deuterated toluene. This directly transforms into the amount of solvent remaining in the polymer film.

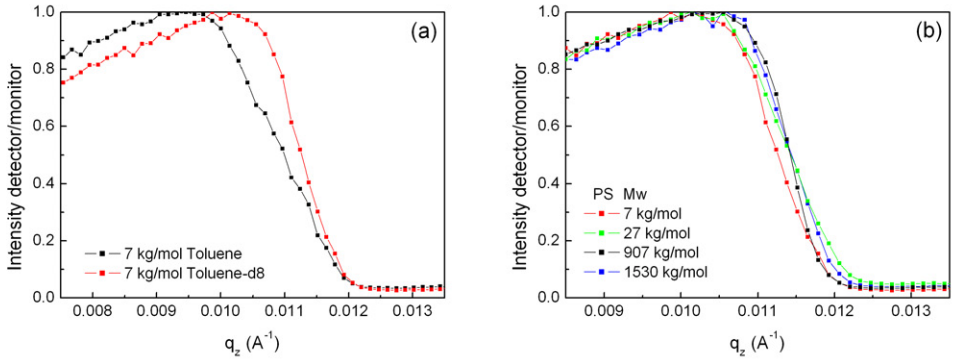

Figure 1: (Left) Neutron reflectivity data for spin-coated thin polystyrene (PS) films with a molecular weight Mw = 7 kg/mol and fixed film thickness. Depending on the use of protonated and deuterated (d8) toluene, the position of the critical edge shifts significantly. (Right) Neutron reflectivity data of thin PS films with different molecular weights and fixed film thickness. With increasing molecular weight the position of the critical edge shifts towards higher q_z values.

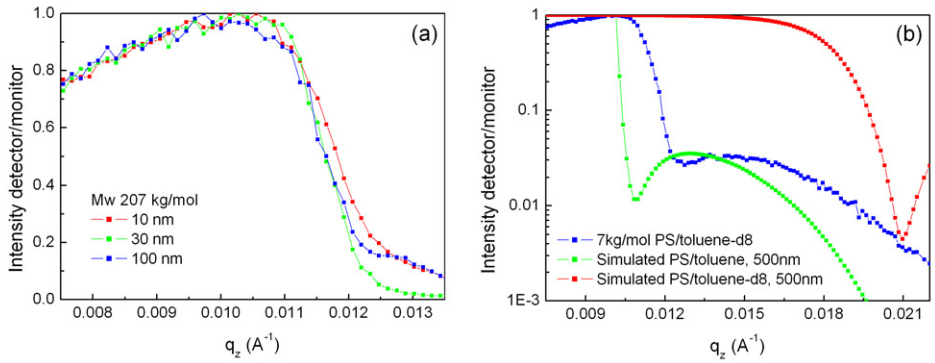

Figure 2: (Left) Neutron reflectivity measurements from spin-coated thin films with PS molecular weight Mw =207 kg/mol and different film thicknesses. (Right) Simulated data for a single PS film on top of bulk Si, for a film SLD of protonated PS and deuterated toluene. Since the measured data is a mixture of both, the measured reflectivity lies within the simulated borders.

2.3 Polarized neutron reflectivity on MIRA: Epitaxial Fe/Cr multilayers

Shah Valloppilly [1], **Christian Schanzer** [2], **Robert Georgii** [1, 3], **Peter Böni** [1]
[1] *Physics Department E21, Technische Universität München, 85747 Garching, Germany*
[2] *Laboratory for Neutron Scattering ETHZ & PSI, CH-5232 Villigen PSI, Switzerland*
[3] *ZWE FRM-II, Technische Universität München, 85747 Garching, Germany*

Fe/Cr thin films and multilayers remain as one of the most extensively investigated systems in thin film magnetism. Some pioneering discoveries in thin film magnetism like interlayer exchange coupling, giant magneto-resistance (GMR) etc. have been made on this system. Complex magnetic structure in Cr render intriguing magnetic properties in bulk as well as in thin films especially when Cr is used as a sandwich layer between two ferromagnet layers. Earlier models of interlayer exchange in Fe/Cr multilayers were based on an oscillatory RKKY-type exchange coupling and quantum-well behaviour of the electrons in the Cr spacer layer. Later, calculations based on the commensurate and incommensurate spin density waves (SDW) in Cr, and direct observation of SDW by neutron scattering suggested that Fe/Cr multilayers display more rich variety of magnetic phenomena. A variety of experimental techniques have been employed for the investigations that extend from bulk to layer resolved magnetometry like in Polarized Neutron Reflectometry (PNR). PNR reveals the vectorial layer magnetization and is very sensitive to the parallel and perpendicular components of magnetization with respect to the neutron polarization. Thus, bilinear and bi-quadratic types of layer configurations can be easily resolved with depth sensitivity. The origin of bi-quadratic exchange has been attributed to intrinsic properties of the spacer layer, dipolar fields resulting from rough surfaces, super-paramagnetic impurities within the spacer, spacer thickness fluctuations etc. It has also been pointed out that the bi-quadratic exchange coupling has a dependence on the SDW.

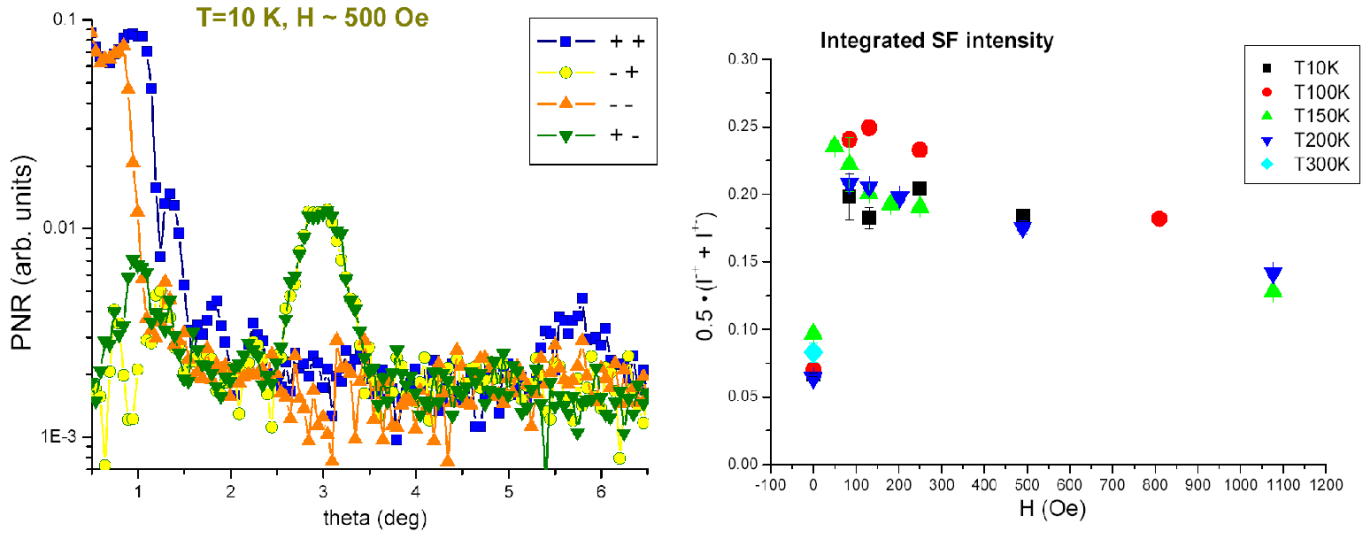

Figure 1: (Left) PNR of Fe/Cr multilayers at 10K and H ≈ 500 Oe. (Right) Dependence of SF intensity as a function of field and temperature.

The objective of the present work is to examine the magnetic configurations of the layers as a function of magnetic field and temperature of epitaxially grown [Fe(4 nm)/Cr(1.5 nm)]10 on MgO single crystal by PNR and corroborate with bulk magnetization results and to find a model to explain the temperature dependence of hysteresis behaviour. Epitaxial, Fe (4 nm)/Cr (1.5 nm)]10 multilayers were grown by magnetron sputtering on a MgO(100) single crystal wafer of 1 x 1 cm. Polarized neutron reflectometry with full polarization analysis was implemented at the MIRA reflectometer by using flipper coils in conjunction with polarizing benders. Due to small size of the sample, a clear total reflection region was not obtainable marred by the large footprint of the beam. Nevertheless, clear effects of PNR are immediately visible in the corrected data as illustrated for a typical case, T=10K and H=500 Oe in Fig. 1(left). The splitting of non spin-flip (NSF) channels + + and - -, and the presence of half order Bragg peak in the spin-flip (SF) channel + - and - + arising from the double periodicity of the magnetic lattice are indicative of the PNR with polarization analysis at MIRA. The experiments were performed around the magnetic (half-order) peak and its intensity as a function of applied magnetic field and temperature was measured. Fig. 1(right) summarizes the SF scattering intensity (integrated intensity of the half order peak) at selected fields and temperatures. In general, at remanence after exposing the sample to a high negative field, the Fe layers are found to order in an antiferroamgnetic configuration as indicated by a high NSF intensity and a low SF intensity. By the application of a small magnetic field of 50 Oe, the NSF intensity drops to low values and the SF intensity increases. With further high magnetic fields, the SF intensity reaches a maximum at a certain field and thereafter decreases gradually. The highest SF scattering indicates the highest deviation of magnetization from the collinear configuration and its field dependence indicates the evolution of magnetization in an exchange coupled magnetization reversal process. Clearly, the magnitude and behaviour of the field dependence of SF intensity at various temperatures, suggest the role of Cr on interlayer exchange and its temperature dependence.

2.4 Temperature dependence of interlayer magnetism in epitaxial Fe/Cr multilayers

V. R. Shah[*1], **C. Schanzer**[2], **S. Mühlbauer**[1], **R. Georgii**[1,3], **P. Böni**[1]
[1] *Physics Department E21, Technical University Munich, D-85747 Garching, Germany*
[2] *Laboratory for Neutron Scattering, ETHZ & PSI, CH-5232 Villigen PSI, Switzerland*
[3] *ZWE FRM-II, Technical University Munich, D-85747 Garching, Germany*

Bulk magnetization and magneto-resistance of epitaxial Fe/Cr multilayers reveals intriguing temperature dependent properties. Bilinear and biquadratic exchange coupling have been resorted to explain the observed peculiar magnetic properties of these multilayers [1]. Epitaxial [Fe(4 nm)/Cr(1.5 nm)]$_{10}$/MgO(100) multilayers grown by magnetron sputtering revealed interesting features in the magnetization reversal processe whose nature is dependent on temperature. The reversals occur in two steps up to $T \approx 100$ K that gradually turn into a multistep process for $T \geq 150$ K as shown in Fig. 1. Bulk magnetization and magneto-resistance at different temperatures had nearly one-to-one correspondence in their behaviour providing volume averaged information. We performed polarized neutron reflectometry (PNR) at different temperatures and fields in order to elucidate information on the magnetization configurations in the temperature and field regions of interest. PNR experiments on a 1 cm x 1 cm sample were performed at the reflectometer MIRA, FRM-II using a monochromatic beam of neutrons with $\lambda = 1$ nm, T = 10 - 300K and H = 0 - 1.1 kOe. Full polarization analysis, incorporating flipper and polarizer bender efficiencies have been performed to deduce the spin-flip (SF) and non spin-flip (NSF) reflectivities of the sample [2]. It has to be mentioned that PNR at low incidence angles on a 1 cm^2 sample is marred by the large foot print of the beam and will not be considered in the discussions. Nevertheless, a rigorous data reduction and identical experimental settings enable us a comparison of the data at different temperatures and fields. The majority of the experiments was performed in the region of interest, where the intensity of the magnetic Bragg peak is monitored at selected fields and temperatures.

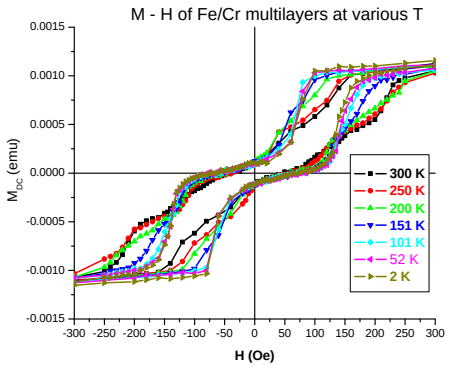

Figure 1: M-H dependence of Fe/Cr multilayers showing a transition from a two step to a multi step magnetization reversal process in the temperature region of 100 - 150 K.

PNR contained features like first order Bragg peak due to structural periodicity, Kiessig fringes that arise from the total thickness of the multilayer and a $\frac{1}{2}$-order Bragg peak due to a doubly periodic magnetic lattice typical for antiferromagnetically-coupled Fe layers. The $\frac{1}{2}$-order Bragg peak intensity is dependent on magnetic field since the applied field destabilizes the antiferromagnetic coupling and aligns the magnetic moments towards saturation. Figs. 2a-2d summarize the integrated intensity of the $\frac{1}{2}$-order Bragg peak as a function of the field and temperature. At $H = 0$ Oe, though a strong antiferromagnetic configuration exists (as seen from strong NSF intensity and weak SF intensity). It becomes easily destabilized by the application of a small magnetic field $H \approx 50$ Oe where the SF intensity increases and the NSF component gets suppressed. This is presumably due to an interplay between bilinear and biquadratic type exchanges that results in many field induced magnetic configurations. The maximum of the SF intensity and the nature of its field dependence is governed by the temperature (Fig. 2). An obvious feature from the graphs is that the maximum in the SF intensity and its field dependence occur also in the temperature region of $T = 100 - 150$ K, coinciding with that of the multi-step magnetization process.

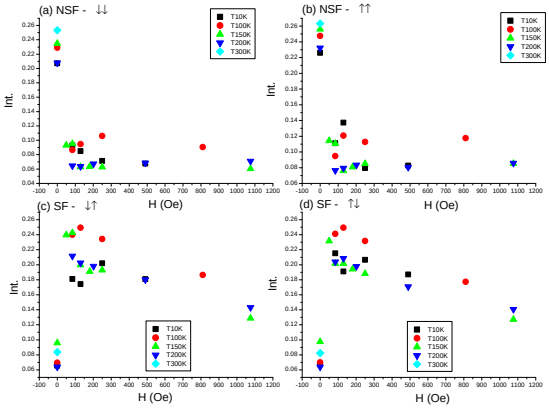

Figure 2: Integrated intensity of the $\frac{1}{2}$-order Bragg peaks in NSF and SF channels as a function of field at selected temperatures

We would like to point out here that this temperature region is also interesting as far as the magnetic properties of Cr are concerned. It is well known that in Cr, a transformation of transverse spin-density wave (TSDW) state to a longitudinal spin-density wave (LSDW) state occurs below the spin-flip temperature T_{SF}=123 K [3]. At the moment it is unclear if the observations of the bulk magnetization and PNR are correlated to the transformation of the SDW phase. Further investigations are needed for a detailed understanding of the magnetic state of both Fe and Cr and this project is being further investigated.

References

[1] D. T. Pierce, J. Unguris, R. J. Celotta, and M.D. Stiles. Effect of roughness, frustration and antiferromagnetic order on magnetic coupling of Fe/Cr multilayers. *J. Magn. Magn. Mater.*, 200:290, 1999.

[2] C. F. Majkrzak. Neutron scattering studies of magnetic thinfilms and multilayers. *Physica B*, 221:342, 1996.

[3] R. S. Fishman. Spin-density waves in Fe/Cr trilayers and multilayers. *J. Phys. Condens. Matter*, 13:R235, 2001.

*Present address: LENS, Indiana University Cyclotron Facility, Bloomington, IN-47408, Indiana, USA.

2.5 Temperature and field dependence of the magnetisation in the ferromagnetic semiconductor EuO

S. Mühlbauer [1], **R. Georgii** [1, 2], **P. Böni** [1], **J. Mannhart** [3], **A. Schmehl** [4], **D. Schlom** [4]
[1] *Technische Universität München, Physics Department E21, D-85747 Garching, Germany*
[2] *ZWE FRM-II, Technische Universität München, D-85747 Garching, Germany*
[3] *Elektronische Korrelationen und Magnetismus, Institut für Physik, Universität Augsburg, Germany*
[4] *Department of Materials Science and Engineering, Pennsylvania State University, Pennsylvania, USA*

EuO_{1-x} films exhibiting the spectacular magnetoresistance and metal-insulator-transition behavior [1] previously seen only in single crystals have been epitaxially integrated with silicon. Bulk EuO is known to be a half metal. Polarised neutron reflectometry is an elegant technique to measure the absolute magnetisation of a flat semi infinite material. For low incident neutron angles, the reflection on a flat surface can be described by means of a potential step function. The potential can by described by the real part of the classical scattering legth $b_{nucl} + b_{mag}$. b_{mag} describes the magnetic scattering length and dependens on the orientation of the magnetic moment with respect to the spin of the incoming neutrons. This yields to a spin-dependence of the angle of total reflection. The sample was therefore mounted inside a closed cycle cryostat, a magnetic field was applied parallel to the incident neutron beam and parallel / antiparallel to the neutron polarisation. The reflection profiles of the cross sections I^{++}, I^{--}, I^{+-}, I^{-+} were measured for temperatures from 20 K to 71 K in a magnetic field of 0 G, 125 G and 250 G, crossing the phase transition at 69 K.

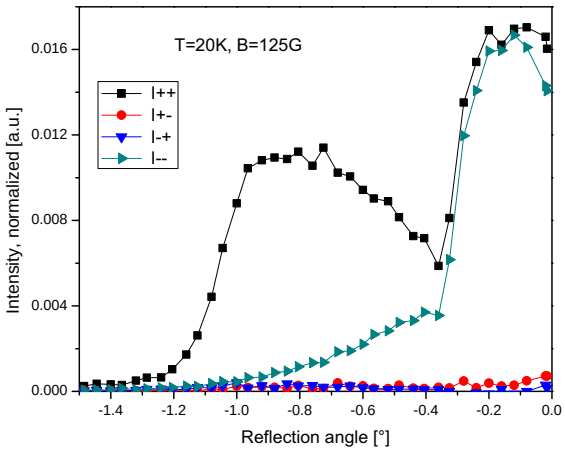

Figure 1: Reflectivity profile of EuO on Si (001), T 20 K, 125 G, full polarisation analysis.)

The absolute net magnetisation of a 500 nm EuO epitaxially grown layer has been determined as function of temperature and magnetic field by means of polarised neutron scattering. The results summarize as follows: Fig. 1 shows a typical reflectivity profile of the EuO sample recorded at 20 K and 125 G. No spin-flip intensiy is observed. The differece between $\Theta_{c1} = \sqrt{\frac{\rho(b_n+b_m}{\pi}}\lambda$ and $\Theta_{c2} = \sqrt{\frac{\rho(b_n-b_m}{\pi}}\lambda$ is cleary visible. Here, b_n and b_m designate the nuclear and magnetic scattering length, respectively. The spin-flip intensity has been corrected for contaminations arising from non-perfect polarisation of the beam. Fig. 2 shows the temperature dependence of reflectivity profile for the non-spin-flip channel $(++)$, Fig. 3 extracts the temperature dependece of the critical angle at 0, 125 and 250 G for $(++)$ and $(--)$. A merging of the critical angles for $T = T_c$, where the ferromagnetism of the sample vanishes, is obvious. At 6,5 K and 125 G, $b_m(Eu^{2+}) = 2.6 \cdot 10^{-12}$ cm is calculated. Compared with literature ($b_m(Eu^{2+}) = 1.904 \cdot 10^{-12}$ cm), this yields a slight systematic alignment error, as also the measured values for $b_n(Eu^{2+})$ and $b_n(O)$ are slightly too large. Normalizing the data to the angle of total reflection of the nuclear contribution of $b_n(Eu^{2+})$ and $b_n(O)$, this yields a value $b_m(Eu^{2+}) = 1.78 \cdot 10^{-12}$ cm that is within 6.5 percent of the literature value.

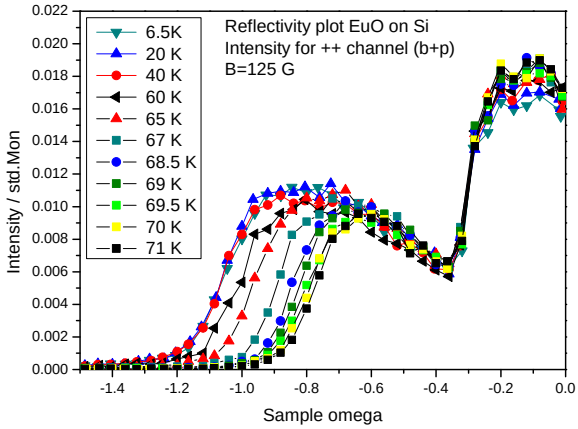

Figure 2: Reflectivity profile of EuO on Si (001), T 6.5-71 K 125 G, ++ channel.

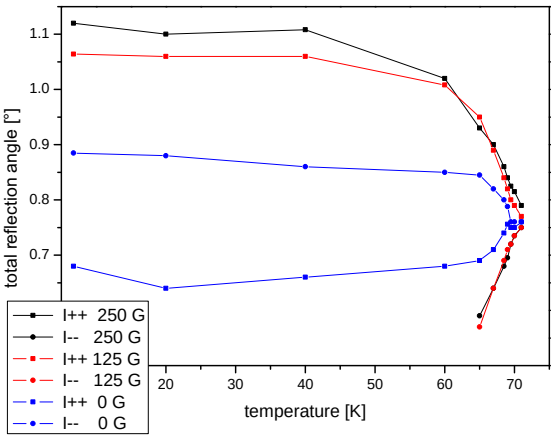

Figure 3: Temperature dependence of the critical angle of EuO on Si (001), ++ and - - channel.

References

[1] G. Petrich et al. *Phys, Rev. Lett.*, **26:885, 1971.**

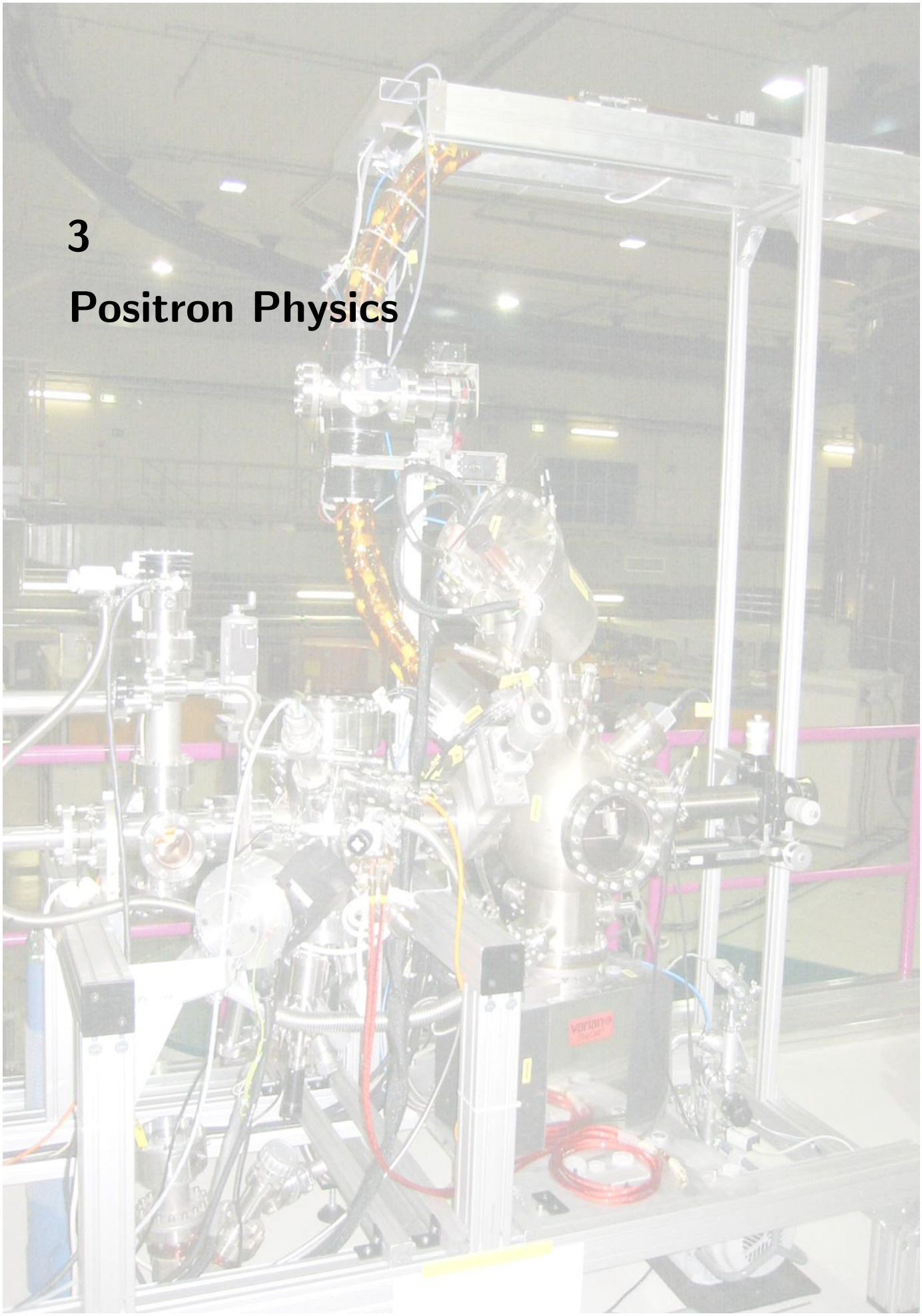

3

Positron Physics

3.1 The Positron Beam Facility NEPOMUC and Instrumentation for Positron

Christoph Hugenschmidt [1, 2], **Thomas Brunner** [1], **Stefan Legl** [1], **Benjamin Löwe** [1], **Jakob Mayer** [1], **Philip Pikart** [1], **Christian Piochacz** [2], **Ning Qi** [1], **Reinhard Repper** [2], **Martin Stadlbauer** [1], **Klaus Schreckenbach** [1, 2]

[1] *Physics Department E21, Technical University Munich, 85747 Garching, Germany*
[2] *ZWE FRM-II, Technical University Munich, 85747 Garching, Germany*

The intensive positron beam at NEPOMUC

In 2006 various experiments were performed at the high intensity positron beam facility at NEPOMUC (NEutron induced POsitron source MUniCh) in order to improve the beam characteristics such as intensity, available energy range and beam brilliance. The maximum positron yield is up to $5 \cdot 10^8$ moderated positrons at a kinetic energy of 1 keV. At present, the lowest available beam energy is 15 eV with an intensity of $4 \cdot 10^7$ positrons per second. The maximum beam energy is limited to the high voltage, that can applied at the platinum foils of the in-pile source components and amounts to about 3 kV. A survey of the beam performance and positron beam experiments can be found in [1, 2]

A decrease of the positron intensity was observed within about 20 h which is attributed to surface contaminations adsorbed at the platinum moderation foils. The regeneration of these foils is achieved by exposure to a small amount of oxygen ($\approx 10^{-1} mbar$) for a few minutes.

In the longitudinal magnetic guide field of 7 mT the diameter of the positron beam amounts typically to 15-20 mm. Since a more brilliant beam (lower divergence and to reduced beam diameter of about 2 mm) is desirable for a variety of experiments several efforts have been made to develop devices for beam enhancement. For this reason an additional remoderation unit based on a tungsten single crystal in reflection geometry was tested at NEPOMUC (section 3.2). Another approach is presently developed, which benefits from inelastic positron scattering in a gas-filled drift-chamber, in order to improve the beam brilliance.

Figure 1: The positron beam facility NEPOMUC and positron spectrometers in the experimental hall of FRM II: CDB spectrometer (TUM), PAES-facility (TUM, not shown), apparatus for Ps^--production (MPI nuclear physics, Heidelberg), and components of the pulsed-beam facility PLEPS (UniBW, Munich).

Instrumentation at NEPOMUC

Fig. 1 shows experiments connected to the positron beam facility NEPOMUC.

The coincident Doppler-broadening spectrometer (CDBS) is routinely operated with a primary beam energy of 1 keV. The beam is focused to about 1 mm and can be accelerated to 31 keV onto the sample in order to allow spatially resolved defect studies. Various experiments have been performed in order to investigate the chemical surrounding at open-volume defects of ion-irradiated metal samples (section 3.3) or defects in metals after mechanical load.

Great efforts have been made in order to reduce the γ-induced electron background for studies with positron annihilation induced Auger-electron spectroscopy (PAES). With new parameter settings of the electrostatic beam guidance at the entrance of the analysis chamber PAES-spectra were recorded within only 3 h acquisition time. Low-energy positrons (15 eV) were focused onto Au-covered surfaces of single crystalline silicon and poly-crystalline copper in order to study sample surfaces with highest sensitivity. (section 3.4).

Two additional experimental setups were installed at the multi-purpose beam port:

An apparatus for the production of the negatively charged positronium (Ps^-) was developed at the Max-Planck-Institute for nuclear physics and connected to the open beam port of the positron beam line. This year first measurements were performed in order to improve the energy dependent production rate of Ps^- and the signal-to-noise ratio. It was shown that the production rate is at least a factor of 25 higher than in previously performed lab experiments which would allow experiments for QED-tests.

The angular correlation and the Doppler-shift of the annihilation photons were detected in coincidence with a second experimental device at the open beam port of NEPOMUC. For this reason two segmented high-resolution germanium detectors were installed in collaboration with E12. At present the data analysis is in progress in order to reconstruct the electron momenta in three dimensions for each annihilation event.

References

[1] C. Hugenschmidt, K. Schreckenbach, M. Stadlbauer, and B. Straßer. *Nucl. Instr. Meth. A*, 554:384–391, 2005.
[2] C. Hugenschmidt, M. Stadlbauer, B. Straßer, and K. Schreckenbach. *Appl. Surf. Sci.*, 252:3098–3105, 2006.

3.2 Positron remoderation facility for the slow positron beam at FRM-II

Christian Piochacz [1, 2, 3], **Christoph Hugenschmidt** [1, 2], **Gottfried Kögel** [3], **Klaus Schreckenbach** [1, 2], **Günther Dollinger** [3]

[1] *Physics Department E21, Technical University Munich, 85747 Garching, Germany*
[2] *ZWE FRM-II, Technical University Munich, 85747 Garching, Germany*
[3] *UniBw München, Institut LRT2, Werner-Heisenberg-Weg 39, D-85577 Neubiberg*

In order to enhance the brightness of the positron beam produced by the NEPOMUC source, a positron remoderator was developed. It has been installed at the first accessible point of the beam facility and first measurements have been done in order to obtain the efficiency of the setup and the quality of the remoderated beam. The idea of using remoderation for brightness enhancement was first described by [1] and has been realized in several table top setups [2] [3]. The remoderation unit described here was designed according to the ideas of the remoderator utilized in [3] but with improvements to accept a beam with a greater phase space volume.

For the remoderation process, positrons are focused on a solid, where they stop and thermalize. There is a certain possibility that the thermalized positrons diffuse back to the surface where they can leave the solid with a sharp energy and a small angular divergency. The whole process depends on the properties of the solid, which is used for moderation. Materials, such as tungsten, nickel and platinum are known to be efficient positron moderators. There are basically two possibilities for remoderating a positron beam, depending on which surface the positrons are emitted: the reflection or the transmission geometry. The presented remoderatoration device works in reflection geometry with a W(100) single crystal. The moderated positrons leave the crystal surface with an energy of about (3 ± 0.03) eV and an angular spread of about 0.1 eV.

Experimental setup

The remoderation setup is shown in Fig. 1. The positrons from the NEPOMUC source are guided by magnetic solenoid fields to the entrance of the device. At the last 60 cm in front of the setup a magnetic field gradient could be varied in order to adjust the ratio of longitudinal and transversal momentum of the beam. The longitudinal magnetic guiding field is terminated by a novel field termination, in order to avoid a complicated and unwished superposition with the electric and magnetic fields inside the remoderator. The field termination is build up of 30 10 μm thick and in the center 2 mm broad metglass stripes. This solution has the advantage of a high transparency even for a beam with a great diameter up to 60 mm and ensures nevertheless an abrupt termination of the magnetic field. After passing this device the positrons fly without a guiding field till they enter the field of the magnetic lens and get focused on the tungsten crystal. The remoderated positrons can pass the field of the magnetic lens adiabatically because of their low energy and are formed electrostatically to a beam. This beam is bent to the outlet by a perpendicular magnetic dipole field which is located at the beam seperator. The electrodes and the dipole have nearly no effect on the primary beam due to its much higher energy in the range between 0.5 and 2 keV. On the outlet two variable apertures permit an adjustment of the remoderated beam onto the center of the axis and allow the determination of the beam diameter. After the remoderation unit the positrons are guided by magnetic solenoidal fields to the different experiments installed at the NEPOMUC facility. Additional electric lenses are installed at the outlet to ensure an optimal injection of the remoderated beam into the magnetic field. The hole setup is magnetically shielded by a mu-metal housing because the slow positrons are very sensitive on magnetic disturbances.

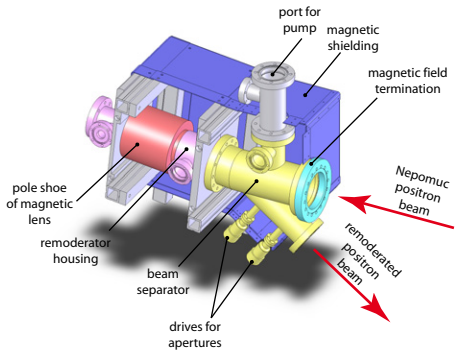

Figure 1: Schematic view of the positron remoderator. The magnetic dipole and magnetic correction coils are not shown.

Results

In order to measure the remoderation efficiency two equivalent and removable annihilating targets in front of the remoderator and behind the outlet of the remoderator were connected. The quality of the primary and the remoderated beam could be evaluated due to pictures taken by two systems consisting of a MCP, phosphor screen and CCD camera. We succeeded to produce very well formed remoderated positron beams at several energies of the primary beam (see fig. 2). At an energy of 1.5 keV a remoderating efficiency of nearly 2 % was attained and the beam diameter of the remoderated beam was about 2 mm (FWHM). This beam could be guided to the open beam port of the NEPOMUC facility and to the PAES experiment for further measurements. The shape of the beam could be conserved perfectly due to the small diameter and the small energy spread of the remoderated beam.

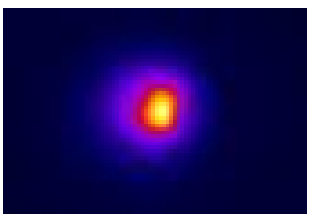

Figure 2: The picture of the profile of the remoderated positron beam taken with a system of MCP, phosphor screen and CCD camera. The beam has a diameter of 2 mm (FWHM).

References

[1] A. P. Mills Jr. *Appl. Phys.*, 23:189, 1980.
[2] W.E. Frieze, D. W. Gidley, and K.G. Lynn. *Phys. Rev. B*, 31(9):5628, 1985.
[3] G. Kögel and SPM-Group. The münchen. *Appl. Surf. Sci.*, 116:108–113, 1997.

3.3 Investigation of AZ31 and ion irradiated Mg with the coincident Doppler broadening spectrometer CDBS

Martin Stadlbauer [1, 2], **Christoph Hugenschmidt** [1, 2], **Klaus Schreckenbach** [1, 2]
[1] *Technical University Munich, Physics Department E21, D-85747 Garching, Germany*
[2] *Technical University Munich, ZWE-FRM2, D-85747 Garching, Germany*

Introduction

The chemical vicinity of open volume defects in alloys is of great interest in material science since it is crucial for the stiffness and tensile strength. The coincident Doppler broadening spectroscopy (CDBS) with positrons allows very sensitive measurements of the electron momentum distribution in defects due to the efficient trapping therein [1]. After annihilation with core electrons from the neighboring atoms, the Doppler shifted 511 keV annihilation radiation reveals the momentum distribution of the involved electrons which depends in particular on the periodic number of the element. A detailed description of CDBS and the CDB-spectrometer at NEPOMUC has been published in [2].

Sample Preparation

Samples with $20 \times 20 \times 3\text{mm}^3$ consisting of pure, polished and annealed Mg have been irradiated with Mg-, Zn- and Al-ions at the 3 MeV-Tandetron in Rossendorf. The energy of the ions were chosen between 1.4 and 3 MeV according to 2.3 μm mean implantation depth. Implantation of Mg-ions into a Mg-sample ensures that only defects change the CDBS-signature. Zn and Al ions were implanted into Mg in order to study the influence of these elements to the CDBS-signature in combination with defects. Single defects and dislocations created by this treatment in magnesium anneal already below 200 K but vacancy clusters survive up to 400 K [3]. For each ion type a set of 4 samples was produced with doses between 3×10^{13} and 3×10^{16} ions/cm^{-2} in order to find a sensitivity threshold for the low doses on the one hand and to get into the region of saturation trapping of positrons for the high doses on the other hand.
The diameter of the ion beam from the tandetron was reduced to 5 mm since spatially resolved positron scans with a resolution of 2 mm should image the ion beam spot on the sample.
Additional samples consisting of pure, polished and annealed AZ31 were irradiated with Mg-ions of 1.4 MeV energy. The same doses were applied as described above.

Measurements and Results

The samples with the maximum ion dose were measured up to now. First, the width of the annihilation line vs. position and energy was recorded with a spacial resolution of 2 mm and positron energies between 1 and 9 keV, since the most obvious variation of this parameter was expected to occur at low energies due to results from previous measurements of the annihilation line width in the irradiated area (see fig.1) which can be clearly detected between 1 and 6 keV. For higher energies the irradiated region could not be separated from the untreated one which is an unexpected result, since the mean penetration depth of the Mg-ions was 2.3 μm corresponding to 17 keV positrons. A possible explanation for this is the very high ion dose (c_{ion} = 35 % in the irradiated region), which may have led to local annealing effects due to local heating during the irradiation procedure.

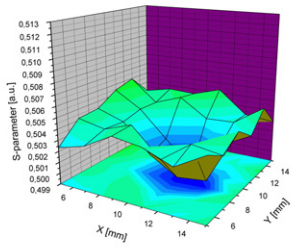

Figure 1: S-parameter vs. position on the Mg-ion irradiated AZ31-sample measured with 4.5 keV *positron energy.*

The coincident spectra of pure Mg irradiated with Mg-, Al- and Zn-ions showed a clear deviation from the pure and untreated Mg-samples 2. Nevertheless the signatures of the irradiated samples are statistically not distinguishable among each other within the error bars between 511 and 513 keV. In particular there is no Zn-signature in the Zn-ion irradiated Mg-sample detectable. This signature is shifted to lower values between 513 and 514.5 keV in contrary to the Zn-curve which shows a large deviation in the high momentum region.

Outlook

Since the high ion dose may have led to local annealing effects in the samples, the next important step is to measure the samples with lower ion dose. First investigations on these samples were very promising.

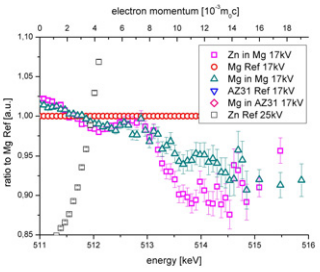

Figure 2: CDB ratio curves of pure Mg and irradiated Mg with Zn- and Mg-ions. The Zn-ion irradiated Mg-sample shows no Zn-signature and is clearly shifted towards the signature of the Mg-ion irradiated sample.

References

[1] M. J. Puska and R. M. Nieminen. *Rev. Mod. Phys.*, 66:841–897, 1994.
[2] M. Stadlbauer, C. Hugenschmidt, C. Piochacz, B. Strasser, and K. Schreckenbach. Spatially resolved investigation of thermally treated brass with a coincident doppler-spectrometer. *Appl. Surf. Science, accepted for publication.*
[3] P. Ehrhart. Mg. In H. Ullmaier, editor, *Atomic Defects in Metals*, page 242. Springer-Verlag GmbH, San Diego, CA, 1991.

3.4 PAES-measurements of pure Cu and Cu coated Si(100)

Jakob Mayer [1], **Christoph Hugenschmidt** [1, 2], **Klaus Schreckenbach** [1, 2]
[1] *Physics Department E21, Technical University Munich, 85747 Garching, Germany*
[2] *ZWE FRM-II, Technical University Munich, 85747 Garching, Germany*

Experimental setup

A spectrometer for positron annihilation induced Auger electron spectroscopy (PAES) has been installed at the high intensity positron beam NEPOMUC. PAES is based on the same principle as conventional electron induced Auger electron spectroscopy (EAES), but with different preceding ionization process. Since electrons in an atom are bound with high energy, the incoming electrons need an energy of at least a few keV to ionize the atoms by impact. At PAES the ionization is realized by electron-positron annihilation and hence positrons with a very low kinetic energy are sufficient ($E_{e^+} \leq 40\,\mathrm{eV}$). Due to the low positron energies, there is no background in the higher energetic regions of the Auger peaks. (n,γ)-reactions of surrounding experiments in the experimental hall at the FRM-II initially led to a higher background than expected (see fig. 1). With the help of a lead shielding this external background has been reduced considerably.

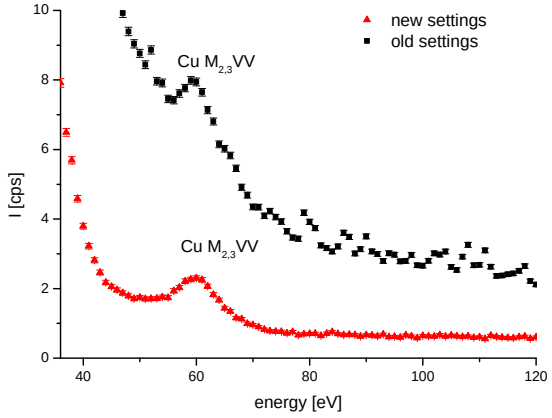

Figure 1: Old PAES-measurements of Cu in comparison with the new measurements (without background). The background was reduced by lead shielding and improved settings of the electric lenses at the entrance of the analysis chamber.

Characteristics of the positron beam at the sample site

The energy of the positrons is defined by the electric lenses and platinum structure in the tip of the NEPOMUC-beamtube [1]. In order to measure the energy distribution of the primary positron beam, the energy of the 30 eV positrons at the entrance of the analysis chamber was measured using a retarding grid in the longitudinal magnetic guiding field and a NaI-detector. In addition the geometric dimensions of the beam have been specified with a MCP and a CCD.

Since only a little fraction ($< 0.6\%$) of the positrons has an higher energy than the expected 30 eV the influence of them to the background is almost negligible. The diameter of the beam was determined to 20 mm.

Measurements and results

Figure 1 shows the reduction of the background due to the lead shielding and enhanced settings of the electric lenses at the entrance of the Auger chamber. The signal to noise ratio with PAES was increased from 1/2 to 2 and is hence a factor of 6 higher than with conventional EAES.

Another feature of PAES, the very high surface sensitivity, was demonstrated with a measurement of clean silicon and of the same sample covered with 1.5 monolayer of copper (see fig. 2). At the coated sample almost 1/5 of the whole Auger-signal, i. e. the sum of all detected Auger electrons, originates from copper. With EAES this quotient is only 1/13, since the electrons penetrate deeper into the Si-substrate. This shows the high surface sensitivity of PAES.

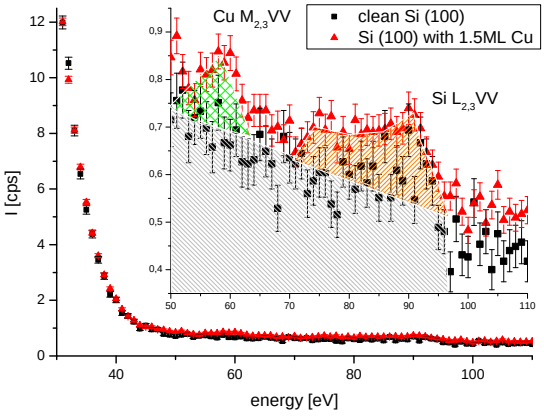

Figure 2: Single crystalline clean silicon and the same sample covered with 1.5 atomic layers of copper.

Outlook

The results of the recent year show the high potentials of this unique facility. For a further reduction of the measurement time a new electron energy analyzer is required, since the current analyzer has an extremely low detection efficiency. With a new analyzer the detectable area will be enlarged and with nine channeltrons instead of one or even a MCP the measurement time is expected to be reduced at least by a factor of 50. With this investment and a new sample holder for the heating and cooling of the samples the PAES-spectrometer enables temperature dependent surface investigations.

References

[1] C. Hugenschmidt, G. Kögel, R. Repper, K. Schreckenbach, P. Sperr, and W. Triftshäuser. First platinum moderated positron beam based on neutron capture. *Nuclear Instruments and Methods in Physics Research B*, 198:220–229, 2002.

3.5 Spectrometer for the investigation in the temperature dependent positronium formation and moderation efficiency

Thomas Brunner [1, 2], **Christoph Hugenschmidt** [1, 2]
[1] *Physics Department E21, Technical University Munich, 85747 Garching, Germany*
[2] *ZWE FRM-II, Technical University Munich, 85747 Garching, Germany*

Introduction

When positrons are implanted in a sample, some of them thermalise and diffuse back to the surface. In the case of a negative positron workfunction, some of the thermalised positrons leave the bulk with a narrow energy distribution as moderated positrons.
Additionally, positrons are trapped in surface states where they form positronium. These positronium atoms exist in either ortho– or para–positronium states (o–Ps and p–Ps) and might leave the surface as thermally activated positronium . Due to the short vacuum live time of 125 ps (p–Ps) or 141 ns (o–Ps) and the thermal energy, positronium annihilates near the surface. Therefore, the p–ps annihilation in two 511 keV γ–quants can not be separated from positrons annihilating in the sample. But the continuous ortho positronium annihilation spectrum [1] leads to a change in the γ spectrum. This allows the determination of positronium formation by observing the annihilation spectrum with a high resolution germanium detector. If ortho–positronium is formed, the 511 keV photo–peak intensity is reduced and the count rate in the valley between Compton edge and peak increases. For this reason the production of positronium can be determined by comparing the ratio of the counts in the photo peak and valley (peak to valley ratio).

Setup

To separate the detection of remoderated positrons and positronium, detailed simulations were performed in order to gain an optimal setup. These simulations let to the setup shown in figure 1. There, the positrons enter from the left side after they have passed a magnetic field termination. Afterwards, they are guided and focussed on the sample electrostatically. At the sample surface positronium formation is observed with a germanium detector. Remoderated positrons leave the sample and travel backwards to the deflecting grid where they are reflected onto the annihilation target. Comparing the count rate at the target with the stopping grid potential, one can determine the positron workfunction.
This novel spectrometer was constructed and installed at the ^{22}Na based laboratory positron beam and first measurements were performed. A closed–cycle cryostat allows to control the sample temperature. The implantation depth can be varied due to variable sample potentials up to 15 keV.

Measurements

Because the peak to valley ratio is an abstract value, it is convenient to calibrate the ratio. Therefore two annihilation spectra were taken. According to the prohibition of positronium formation in metals, positrons with 10.5 keV were implanted in the bulk where no positronium is formed. Another spectrum was taken at hot germanium (T=800 K) with 1 keV incident positron energy and hence the positronium formation amounted to 0.8 according to literature values [2]. The normalised spectra in figure 2 illustrate the change in the spectrum if positronium annihilation occurs.
First temperature dependent measurements were performed on solid CO_2 and presently, rare gases will be investigated and compared.

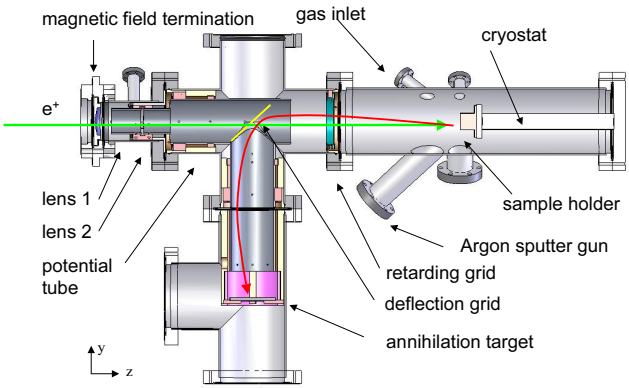

Figure 1: Setup of the Spectrometer. The Positrons enter from the left side (green) and hit the sample. Afterwards, remoderated positrons travel back (red) and are reflected by the deflection grid.

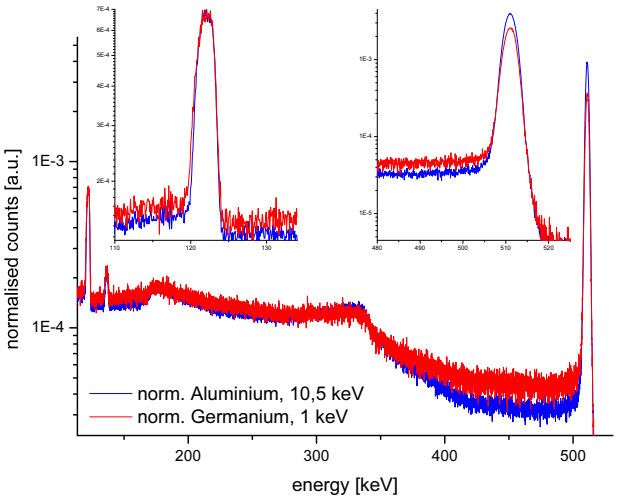

Figure 2: Positron annihilation spectrum in aluminum (no positronium formation, blue) and on the surface of hot germanium (efficient positronium formation, red)

References

[1] A. Ore and J. L. Powell. Three-Photon Annihilation of an Electron-Positron Pair. *Phys. Rev.*, 75(11):1696–1699, June 1949.
[2] A. P. Mills, Jr. Positronium Formation at Surfaces. *Phys. Rev. Lett.*, 41(26):1828–1831, December 1978.

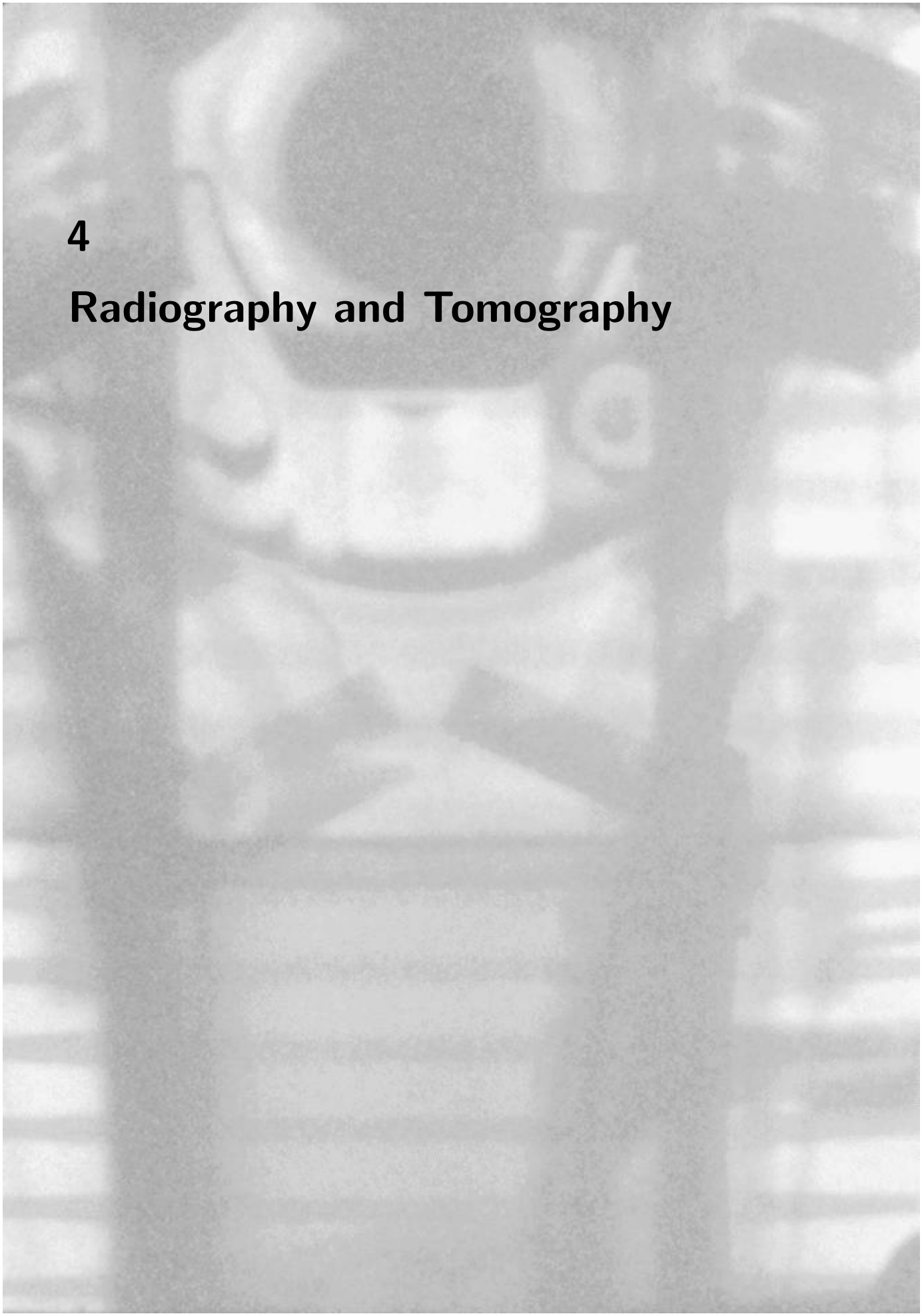

4

Radiography and Tomography

4.1 Neutron phase contrast tomography

Klaus Lorenz [1], **Burkhard Schillinger** [1, 2]
[1] *Physics Department E21, Technical University Munich, 85747 Garching, Germany*
[2] *FRM-II, Lichtenbergstraße 1, 85747 Garching, Germany*

Experimental Setup

In neutron phase contrast imaging the variation δ of the real part of the refractive index $n = 1 - \delta + i\beta$ from unity is used to get an additional contrast besides absorption contrast. The easiest way to get this phase contrast is to use a propagation based method. Unlike interferometric measurement methods, no complicated experimental setup is necessary. Basically the same setup as for conventional neutron radiography can be used with two additional requirements: The neutron beam must have a high transversal spatial coherence at the sample position and the detector must have a certain distance from the sample [1]. The high coherence is achieved by the introduction of pinhole apertures with a diameter of 2mm and less in the beam in a distance of 14m to the sample position (see fig. 1). Due to the drastically reduced neutron flux, exposure times in phase contrast measurements are much longer than in conventional neutron radiography, what makes this method much more sensitive to background noise.

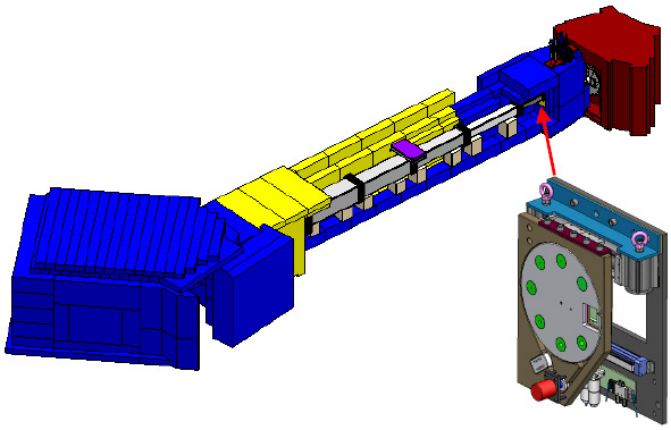

Figure 1: Implementation of the pinhole apertures at ANTARES.

Main causes for noise are epithermal neutrons and gamma radiation in the beam, secondary radiation due to activation and inherent noise of the detector system. Until recently, the noise level in long time exposure radiographies with a CCD detector system was much too high for phase contrast imaging. Good results were only achieved with image plate detectors [2], which have the big disadvantage of not allowing normalization and tomographies. After some modifications of the pinhole apertures, the improvement of the shieldings in the sample and detector area and the installation of the new multi filter (see corresponding report), the signal-to-noise-ratio in long time exposure measurements with the CCD detector improved significantly and allowed the step from phase contrast radiography to phase contrast tomography.

Applications

In figure 2 the results of a conventional tomography are compared with those using the phase contrast effect. The effect is only used in a qualitative way for contrast enhancement at edges and interfaces, the phase shift is not measured directly (no phase retrieval).

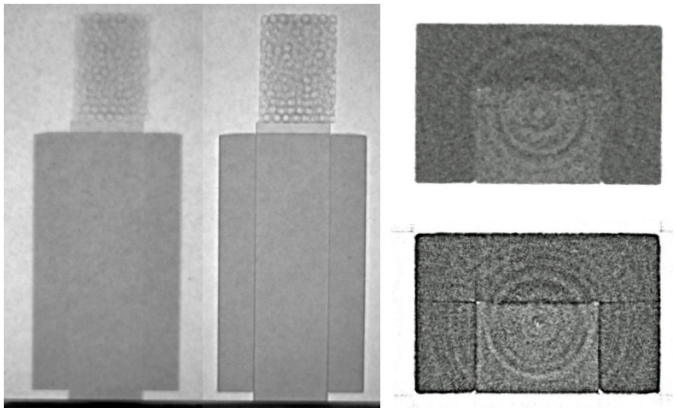

Figure 2: Comparison of conventional and phase contrast radiography (left) and tomography (reconstructed slice, right).

The test sample is a step wedge out of $AlMg_{4.5}Mn$ with another aluminum alloy ($AlSi_9Cu_4$) cast around it (see fig. 3). Both alloys have very similar attenuation coefficients. Because of this and the fact, that the sample has a constant thickness in beam direction, there is no contrast between the different steps in conventional neutron imaging. Under phase contrast conditions, due to the fact that Manganese causes a negative and Copper a strong positive phase shift, phase contrast occurs at the inner interfaces which are parallel to the direction of the neutron beam.

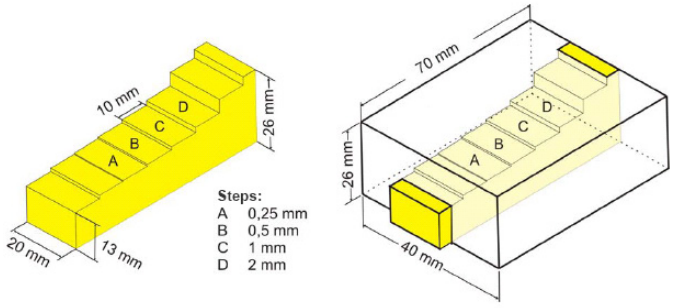

Figure 3: Schematic of the test sample.

References

[1] John M. Cowley. In *Diffraction Physics*. Elsevier, Amsterdam, Netherlands, 1995.
[2] Eberhard Lehmann, Klaus Lorenz, Erich Steichele, and Peter Vontobel. Non-destructive testing with neutron phase contrast imaging. *Nucl. Instr. and Meth. in Phys. Res. A*, 542:95–99, 2005.

4.2 Implementation of the new multi filter at ANTARES

Klaus Lorenz [1], **Elbio Calzada** [2], **Martin Mühlbauer** [1, 2], **Michael Schulz** [1, 2], **Burkhard Schillinger** [1, 2], **Karl Zeitelhack** [2]

[1] *Physics Department E21, Technical University Munich, 85747 Garching, Germany*
[2] *FRM-II, Lichtenbergstraße 1, 85747 Garching, Germany*

Design efforts

A new multi-filter is ready for application at the ANTARES facility at FRM-II. Between fast shutter and aperture wheel [1] a very compact filter package was installed (fig. 1) allowing the quick and precise positioning of four different crystal filters in the neutron beam. Due to the limited space at this position, the maximum thickness for the filters was 50mm, which is the thickness of all but the beryllium filter (only two 20mm thick beryllium plates were available, which were combined to a 40mm filter). The effect of the different filters on the neutron spectrum was investigated with TOF measurements (fig. 2). The cause for the offset in the raw TOF data are epithermal and also a fraction of the thermal neutrons, that penetrate the Gd coatinng of the chopper wheel.

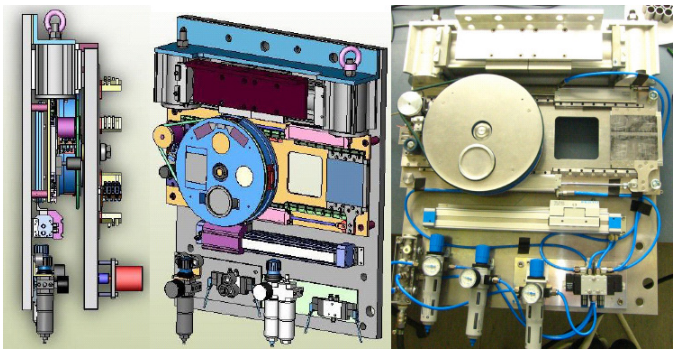

Figure 1: The new multi-filter (schematic (left) and photograph (right).

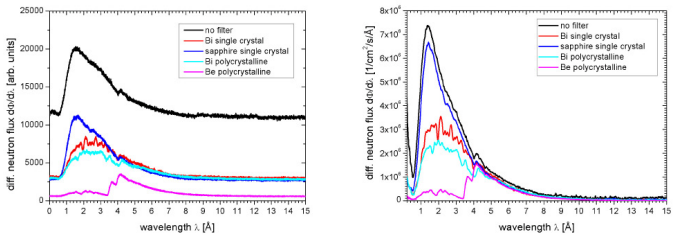

Figure 2: TOF measurements of the neutron spectrum at ANTARES with the different crystal filters (raw data on the left side and corrected data on the right side).

Sapphire single crystals are well known as good filters for epithermal neutrons [2, 3] and the TOF measurement confirms that the installed filter efficiently blocks epithermal neutrons without remarkable modifications of the spectrum in the thermal an cold range. This is e. g. very useful for phase contrast imaging with a LiF-scintillator [1, 4], where epithermal neutrons are a major cause for noise. Another reason for background noise is X-ray and gamma radiation. Because of its high atomic number and transparency for cold and thermal neutrons, bismuth is a very good gamma filter. Beside the single crystal gamma filter a polycrystalline bismuth filter was installed to investigate the utilization of certain bragg edges in neutron imaging. Finally a beryllium filter was installed to suppress thermal neutrons (below 3.96Å[5]). This modification of the spectrum is on the one hand useful for measurements, where only cold neutrons contribute to the measured signal (e. g. phase contrast imaging with gratings), on the other hand it can be used in a primitive way for energy selective radiography (fig. 3).

Applications

In fig. 3 neutron radiographies of step wedges of different materials are shown. The upper was done without a filter, the one below with the beryllium filter and the lowest picture displays the result of the division of the upper two. In the radiography without a filter the attenuation of the neutron beam by iron is only slightly higher than of the lead. With the beryllium filter this changes and the lead attenuates the beam stronger than the iron. The contrast is still not high, but if the radiography without filter is divided by the radiography with beryllium filter, the contrast becomes clearly visible. This method is an easy way to increase the contrast for certain materials in neutron radiographies.

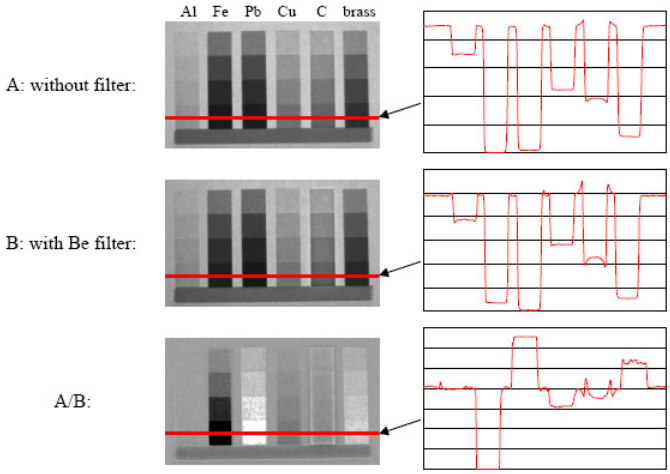

Figure 3: Method to increase the contrast for certain materials in neutron radiographies with a beryllium filter.

References

[1] Eberhard Lehmann, Klaus Lorenz, Erich Steichele, and Peter Vontobel. Non-destructive testing with neutron phase contrast imaging. *Nucl. Instr. and Meth. in Phys. Res. A*, 542:95–99, 2005.

[2] Schneider J. R. Born R., Hohlwein D. and Kakurai K. Characterization of a sapphire single crystal for the use as filter in thermal neutron scattering. *Nucl. Instr. and Meth. in Phys. Res. A*, 262:359–365, 1987.

[3] Stamatelatos I. E. and Messoloras S. Sapphire filter thickness optimization in neutron scattering instrumen. *Rev. Sci. Instr.*, 71:70–73, 2000.

[4] John M. Cowley. In *Diffraction Physics*. Elsevier, Amsterdam, Netherlands, 1995.

[5] Webb F. J. The leakage of thermal neutrons through beryllium filters. *Nucl. Instr. and Meth.*, 69:325–329, 1969.

4.3 Investigation of an early medieval sword by neutron tomography at ANTARES

Martin Mühlbauer [1, 2], **Elbio Calzada** [1, 2], **Brigitte Haas-Gebhard** [3], **Rupert Gebhard** [3], **Klaus Lorenz** [1, 2], **Burkhard Schillinger** [1, 2], **Michael Schulz** [1, 2]

[1] *Technische Universität München, Physics Department, Institute E21, D-85747 Garching, Germany*
[2] *Technische Universität München, ZWE FRM-II, D-85747 Garching, Germany*
[3] *Archaeologische Staatssammlung, München, Germany*

Abstract

We have studied a sword of the 6th century AD from Pforzen near Kempten, Germany. During a complex restoration parts of the scabbard that was constructed of different layers of leather and wood could be conserved. It was presumed that these parts still contain organic material. Therefore it was of interest for us to compare the results of the x-ray analysis to neutron radiography and tomography measurements, as neutrons are sensitive to the hydrogen in the remaining organic material, which is completely invisible for x-rays. This assumption could be verified by the examination results.

Introduction

The preservation of archaeological artifacts depends on the various corrosion processes of the artifacts during burial. Since wetland finds are scarce in Bavaria and dry or cold preservation is missing, organic material is very rare. There are however a few cases of preservation of organic parts sticking to metallic artifacts in early medieval burials. They are mainly conserved by iron oxides diffusion into the organic parts. In most cases the organic material was totally converted into iron or copper oxides, sometimes however organic material could remain. The results of the neutron tomography allow a reconstruction of the organic scabbard. It was constructed of two wooden parts that have been covered at the inner side with leather or skin and leather at the outer side. This construction has been strengthened by winding a string around near the top part of the scabbard. Additionally some bronze parts are mounted at the tip of the scabbard and where it is attached to the belt. The center part of the sword blade was decorated in damask technique. This however could also be observed by x-ray techniques. The organic parts are shown very well by neutron tomography. The attenuation of the neutron beam caused by the organic material is enhanced due to the conservation treatment by resins. The diffusion of these resins within the object is uneven. Neutron tomography could therefore be used to check the conservation process as well. The investigated sword is property of the Free State of Bavaria and kept in the Archaeological State Collection (Archäologische Staatssammlung) in Munich [1].

The neutron radiography and tomography facility ANTARES at FRM II

The measurements were carried out at the neutron radiography and tomography facility ANTARES at the Froschungsneutronenquelle Heinz Maier-Leibnitz (FRM II) in Garching, Bavaria, Germany. This facility is operated by the Institute for experimental Physics E21 [2]. The E21 and FRM II are both part of the Technische Universität München (TUM). By exchanging a part of the main collimator the effective aperture diameter of the collimator system can be reduced from 4.1 cm to 2.15 cm. Thus two main beam geometries are available at ANTARES, which result in L/D ratios of 400 and 800 respectively. The corresponding neutron flux at the sample position after a 16 m flight path is $1.0 \cdot 10^8\,s^{-1}cm^{-2}$ or $2.5 \cdot 10^7\,s^{-1}cm^{-2}$. Additional apertures made of cadmium allow to increase the L/D ratio up to about 16000. These apertures are used for phase contrast measurements predominately. The energy spectrum of the neutron beam can be described by a Maxwellian distribution for thermal neutrons with an enhancement in the cold energy range due to the cold source filled with liquid deuterium at 25 K in front of the radiography beam tube. The maximum beam size at the sample position is 40 cm by 40 cm.

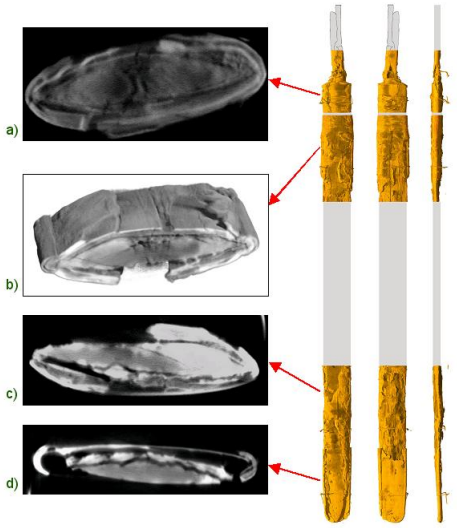

Figure 1: right: overview of the four tomography data sets taken from the sword and the scabbard, left: different slices and cuts of the reconstructed data.

The detector system we used for the measurement was a CCD-camera in combination with a scintillation screen. The field of view was set to 14 cm by 14 cm and a L/D ratio of 800 was used. One scan showing the complete sword and four tomography data sets showing only parts of the sword were taken. Two of the data sets display an upper part and two form a lower part of the scabbard and the sword (fig. 1). The distance of the axis of rotation of the sample to the scintillator was 10 cm and the minimum distance of the sample surface to the scintillator was about 8 cm. For each radiograph the exposure time was 20 seconds. As 400 projections over 180 degrees were taken for each tomography data set, it required 3 hours to acquire the raw data of one tomography (readout time included). The achieved resolution was limited by the scintillator to about 0.5 mm.

Results

The scabbard is composed from the inside to the outside of different layers: fur, wood, leather, cord, bronze. The structure of the composition of the scabbard is visible in cuts

through the three dimensional dataset. So it is possible to check the existence and condition of the different layers over the whole length of the sample.

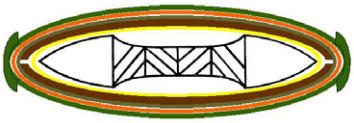

Figure 2: sketch of the structure of the scabbard, from the inside to the outside it is built from fur, wood, leather, cord, bronze.

These layers are not existent on the whole scabbard, e.g. the bronze strengthening is only placed at the tip of the scabbard and where it is attached to the belt of the warrior. For a sketch showing the different layers of the scabbard see figure 2. The two edges of the sword are still in good condition (fig. 3). The corrosion process starts in the center region of the sword where different iron material was used for the damask technique. A thin intermediate layer is found between the sword and the scabbard. Here small connections are found built from the fur on the inner side of the scabbard and the corrosion products of the sword. Cracks in the wooden parts of the scabbard or in the sword can be found and followed. The same is true for the damask structure in the core of the sword.

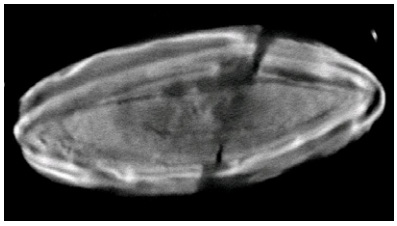

Figure 3: cut through the reconstructed 3D data set showing a crack in the scabbard.

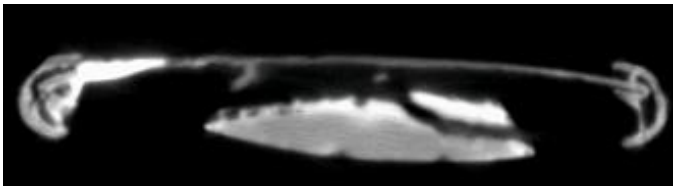

Figure 4: small piece of the blade apart from the rest of the sword.

At the tip of the sword a small part has broken away from the rest of the sword (fig. 4). This is not visible from outside because of the bronze cover. We found a heavily attenuating part at the cone end of the scabbard. At first we were wondering if it could be a part of the sword, which had been separated from the blade. We could not explain why its position was so close to the border of the scabbard. It seemed not to belong to the sword, because it was too far away from the rest of the sword and did not merge to it on either end. Then we compared the x-ray radiograph with the neutron radiograph again, and it turned out that it had to be an organic part, because it was only visible in the neutron radiograph (see fig. 5). The existence of this part was not known before and it was unclear why it was placed there. It is likely that it was used to fix the tip of the sword when it was placed in the scabbard. This special construction was detected on early medieval swords for the first time. It takes further investigations to verify this construction element on other early medieval scabbards. It has to be discussed if this part was a general construction element or it was only applied at the sword of this study in connection with a repair after the loss of the bronze plate at the back side of the tip of the scabbard.

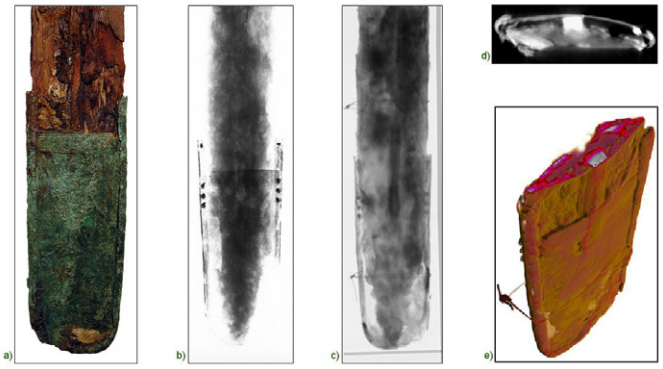

Figure 5: Comparison of x-ray radiography (b) and neutron tomography (c): A strip of wood could be detected under the bronze metal sheet that covers the front side of the scabbard. The bronze metal sheet of the backside has been lost in antiquity.

Conclusions

The application of neutron radiography and tomography methods in this field of archeology is a very useful non destructive technique for the study of the inner structure of archaeological artifacts. Comparable results could only be achieved by mechanical removal of the different layers of the object. This however would destroy the objects irreversibly. Neutrons are not the only tool to investigate archeological objects, but they give further information to complete the research results. In combination with x-ray measurements archeological objects can be investigated without damage or loss of material. X-rays show primarily the remains of the metallic sword while neutrons show the surrounding organic material in addition. Thus it is easy to focus on the sword using x-rays. The organic material of the scabbard is suppressed. This was very important to ensure that the strong attenuating part found at the cone end of the scabbard was wooden. Looking at the scabbard from the outside, the organic material does not give the impression of organic material due to the heavy uptake of metal oxides during the decomposition process. Often a comparison of the x-ray and the n-ray results with the structural details that are visible on the surface of the object gives enough information for the archeologists. The outer layer of the organic structure can be seen with the naked eye, but there are still some layers beneath which can not be investigated without removing the covering layers unless you are using neutrons to get this additional information. The wooden part to fix the tip of the sword is an example for a perfect complement of x-rays and neutrons.

Acknowledgment

We thank the restoration department of the Archeological State Collection Munich for sample preparation and providing the x-ray data.

References

[1] Archeologische Staatssammlung homepage:. http://www.lrz-muenchen.de/ arch/start.html.

[2] E21 homepage:. http://e21.frm2.tum.de/.

4.4 Observation of the filling level of the FRM II cold source by pinhole neutron radiography

Burkhard Schillinger [1, 2], **Elbio Calzada** [1, 2], **Christian Müller** [2]
[1] *Physics Department E21, Technical University Munich, 85747 Garching, Germany*
[2] *FRM-II, Lichtenbergstraße 1, 85747 Garching, Germany*

Abstract

The ANTARES facility for neutron imaging is situated at beam port SR4 facing the cold source. By using a 2 mm pinhole, the surface of the cold source was imaged onto the detector. At low power during reactor startup when the liquid D2 was not boiling yet, the filling level of the cold source was observed. From the geometrical parameters of this projection, the filling level of the cold source was calculated.

The cold source and the ANTARES facility

During reactor shutdown, the liquid D2 filling of the cold source of the FRM II reactor is transferred to a hydride storage system. The refilling of the cold source before startup is a difficult process, where the exact amount of deuterium filling of the cold source is not easy to determine.

The ANTARES facility is situated on beam port SR4b facing the cold source. (fig. 1) ANTARES posesses an external secondary shutter outside of the drum shutter in the biological shielding. Behind this secondary shutter, a selector wheel is mounted containing different pin hole apertures for phase contrast imaging (fig. 2) .

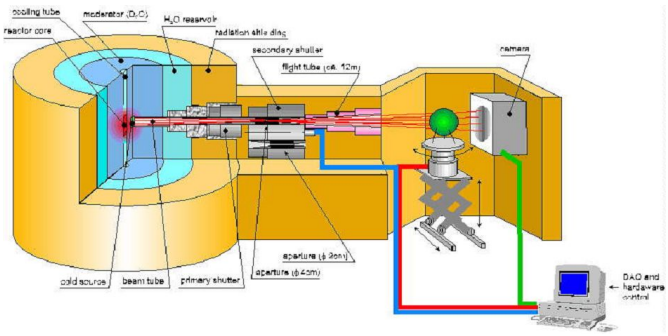

Figure 1: Schematic view of the ANTARES facility. The whole imaging facility is built in a pin hole camera geometry, imaging the surface of the cold source onto the sample area.

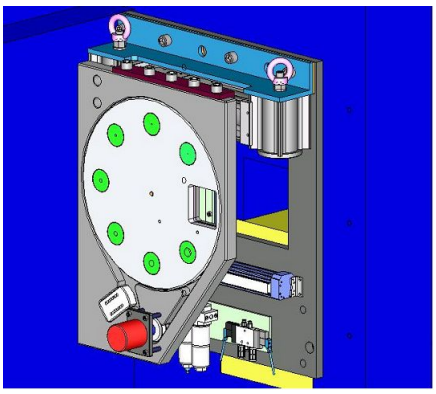

Figure 2: Selector wheel for various pinholes.

The cold source is a slightly tilted container filled with liquid D2. To homogenize the flux and to minimize self-absorption, it contains a hollow displacement body shaped like an inverted cup (fig. 3) (fig. 4) . After filling, the container and the cup contain liquid D2 to a certain filling level. When the reactor reaches power, the D2 starts to boil. The displacement body fills with gas and displaces the liquid inside, thus raising the liquid level outside the cup. The beam tube SR4 feeding the ANTARES facility faces the surface of the cold source. In normal operation, the effective pinhole camera geometry of ANTARES images an unsharp projection of the surface of the cold source onto the sample area, leading to a a homogenous flux distribution. If one of the small pinhole diaphragms intended for phase contrast imaging is used, a sharp well-defined projection of the surface itself is imaged onto the camera.

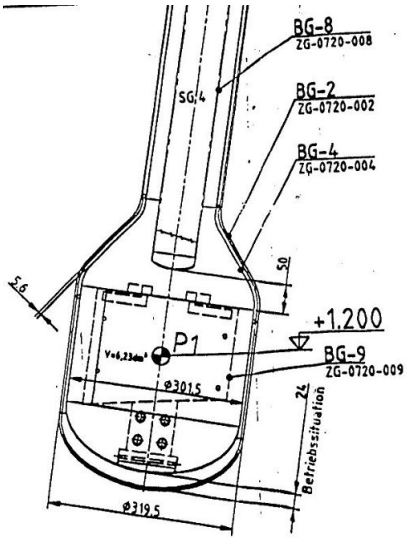

Figure 3: Drawing of the displacement body inside the cold source.

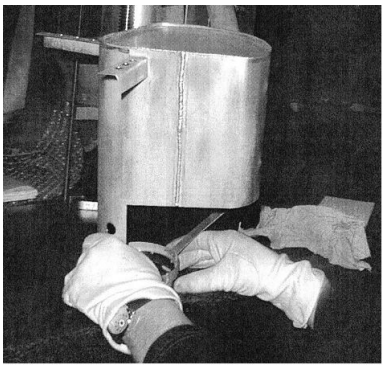

Figure 4: Photo of the displacement body.

Visualization of the filling level of the cold source

During a first reactor startup, reactor power was halted at several power levels between 300 kW and 5 MW. Pinholes with 1, 2, and 7 mm diameter were tested. Best results were obtained with the 2 mm pin hole at 3 MW reactor power. The very small pinhole required exposure times between 10 and 30 minutes. Since the pinhole camera shows an inverted image, the cold source is shown upside down with the liquid level from top to bottom. The liquid is seen as darker (less intensity) because neutrons emitted from the liquid D2 are moderated to lower average wavelength. On the way to the detector, the neutrons have to pass several walls and windows: The ZircAlloy wall of the cold source, the Aluminium beam tube nozzle and the vacuum windows of the beam tubes. The absorption and scattering cross sections increase with increasing wavelength, causing higher attenuation for cold neutrons than for thermal neutrons. Fig. 5 shows the upside-down image of the liquid level in the cold source at 3 MW reactor power, Fig. 6 shows the same field of view at 5 MW, with the visible liquid level gone as the cold source boils at this power.

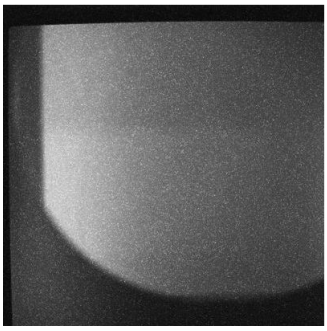

Figure 5: The cold source at 3 MW with the filling level visible

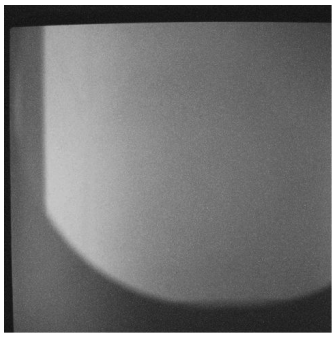

Figure 6: At 5 MW, the visible level is gone.

Measurement of the filling level of the cold source

At a following reactor startup, the experiment was repeated for attempted quantitative measurement. For gauging the image scale, and marking the beam center, two strips of borated polyethylen of known width were fastened at the beam exit, the horizontal strip was tilted to make the image asymmetric so there would be no doubt about the correct orientation of the image. Fig. 7 shows the image of the cold source with the polyethylen strips in the beam, Fig. 8 has the dimensions inserted.

Figure 7: The cold source at 3 MW with polethylen strips in the beam, with the geometric center marked by the upper corner of the horizontal strip.

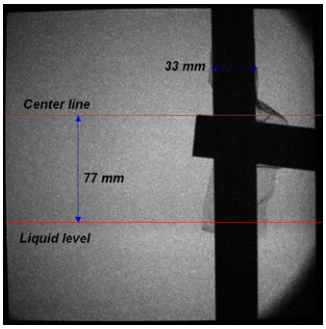

Figure 8: Gauging of scale and projection ratio from measured distances.

With the strip width of 33 mm, the scale of the image was determined. The liquid level was thus measured at 77 mm distance from the center line (Fig.8). With the known distances between the cold source and the pinhole and the pinhole and the detector, the projection ratio was calculated and the 77 mm distance at the detector correspond to 28 mm at the cold source. From the CAD model of the cold source, the filling volume of the cold source at the center line of the beam was determined as 10,636 cubic centimeters or roughly 10.6 liters, with one centimeter height difference corresponding to 704 cubic centimeters. The determined filling level was then calculated as 12,626 cubic centimeters, or roughly 12.6 liters. Only after these calculations, we asked the experts for the cold source for their estimate of the actual filling. They assumed that the best filling they obtained was 12.5 liters.

Conclusions

The surprising apparent accuracy of this measurement in spite of so many inaccuracies involved may be pure coincidence and luck At the time of writing, there had been no opportunity yet to repeat the measurement on a consecutive reactor startup. The results will be verified by a new experiment as soon as possible.

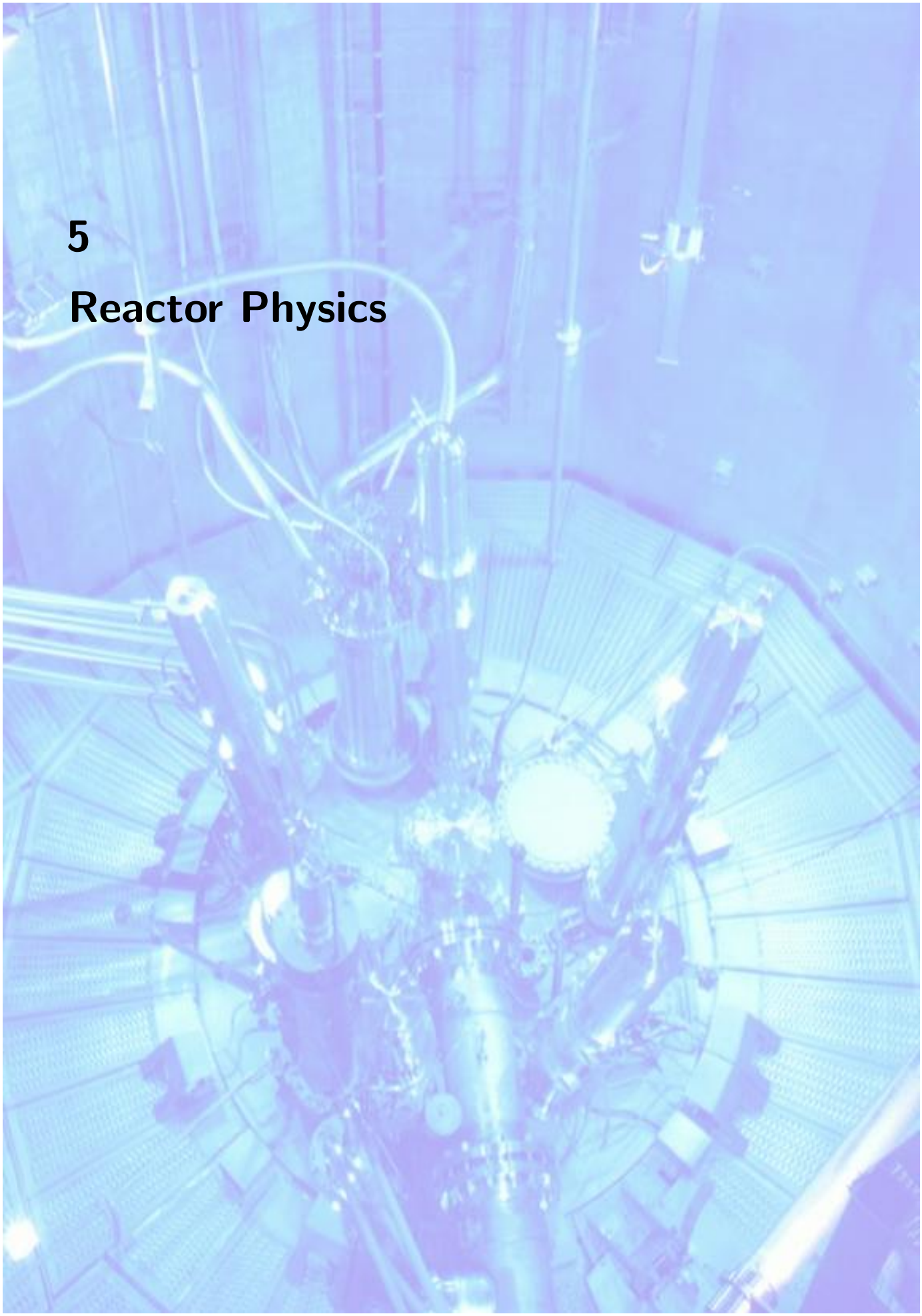

5
Reactor Physics

5.1 Calibration of the Control Rod of the FRM II in the Subcritical Regime

Klaus Schreckenbach [1]

[1] Technische Universität München, Physics Department E21 and FRM II, D-85747 Garching, Germany

For the performance and safety of a nuclear reactor the reactivity worth calibrations of the control and shut down rods are of major importance. The experimental verification of the calculated values are also a valuable bench mark for the validation of the programs used.

The FRM II is equipped with a control rod in the center of the light water cooled fuel element and five shut-down rods in the surrounding heavy water reflector. For routine operation all shut down rods are withdrawn and the reactor is stabilized by the control rod from the top. With the control rod fully inserted the reactor is subcritical with a high safety margin. In the present report the safety margin is deduced from measured data and compared with calculations.

The shut down reactivity for the inserted control rod was determined during the start up of the reactor by extrapolation of the reactivity worth measured above the critical position. A more quantitative measurement is the drop rod method or the calculation from the subcritical counting rates. In the present report the subcritical counting rate is evaluated.

In the subcritical regime the fuel element serves as a neutron amplifier of an external neutron source. During the first criticality a Cf-252 neutron source was used. For an already irradiated core the photo neutrons could serve as primary neutron source.

For a neutron source S_0 with the same distribution as the neutron induced fission reactions and for the point kinetic approximation the neutron density $n(x)$ as function of control rod position x is related to the neutron multiplication factor k by

$$n(x) = \frac{S_0}{1-k(x)}$$

$$k(x) = 1 - \frac{S_0}{n(x)}$$

$$S_0 = -\frac{dk}{dx} / \frac{d(\frac{1}{n})}{dx}$$

The reactivity ρ is related to k by $\rho = (k-1)/k$. In one of the cases discussed here, the reactor core was already used and photo neutrons were produced by gamma rays from the core in the heavy water. Criticality occurred at a higher control rod position (384 mm) compared to a fresh fuel (340 mm). For this case the above prerequisites are fulfilled approximately and the unknown parameter S_0 (here photo neutron source) can be determined from the derivative dk/dx as measured for the fresh core with the critical reactor at 340 mm. The neutrons were counted in wide range detectors (WR) surrounding the heavy water vessel (see Fig.1), the counting rate $c_i(x)$ being proportional to $n(x)$ in the point kinetic approximation. The result is shown in fig.2. The middle plane of the core is at level 410 mm.

With the Cf-252 neutron source placed outside the core the geometry (see Fig.1) does even not approximately fulfil the above prerequisites. On the other hand the counting rates $c_i(dummy)$ in the wide range detectors WR were measured with a fuel dummy and the neutron source in place. Thus an approximate evaluation is possible by modifying the above equations:

$$c_i(x) - c_i(dummy) = c_i(0) \cdot k/(1-k)$$

The counting rate $c_i(0)$ corresponds to the part from the neutron source which reaches the fuel element and is amplified. The value of this parameter can again be deduced from the derivative dk/dx close to the critical point.

For the photo neutron case the data agree within the uncertainty with the calculation of A. Röhrmoser (FRM II) (estimated uncertainty for calculation and measurement of dk/dx in total 15%). For the radioactive neutron source the maximum deviation was less than 0,02 in k at $x = 0$ (shut down). It must be emphasized that the shut down margin of the control rod for a fresh fuel element is about $\rho = (k-1)/k = -0,12$ and high compared to -0,02 required by regulation. Thus the present evaluation is a methodical investigation and not a necessary prove for safety of the FRM II.

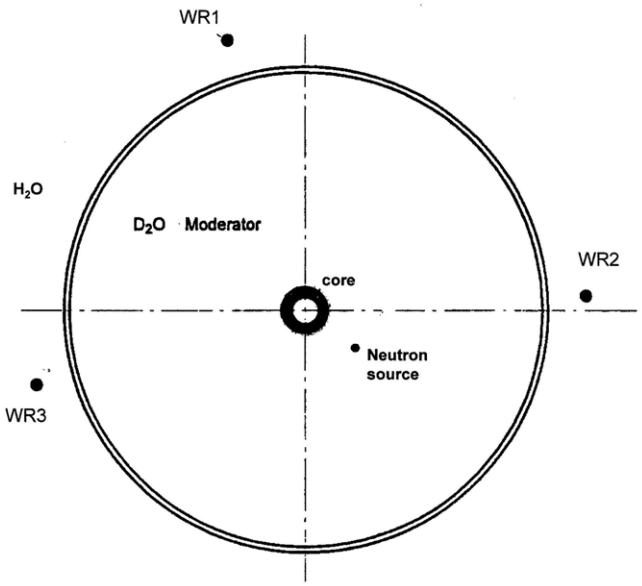

Figure 1: Schematic cross section of the reactor with start-up neutron source and the wide range neutron detectors WR.

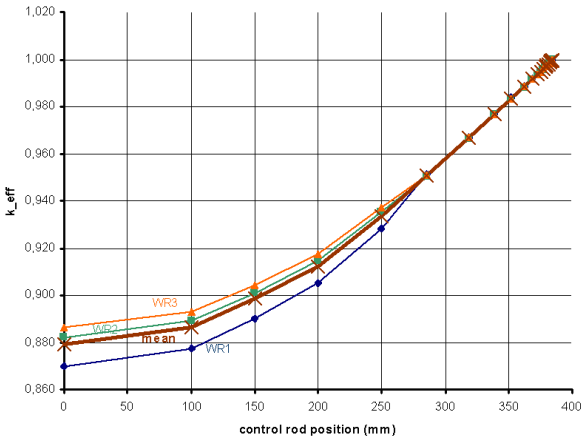

Figure 2: Multiplication factor as function of the control rod position for the photo neutron case.

5.2 A Low frequency modulation method for thermal and electrical conductivity measurements of high-density U-Mo/Al dispersion fuel

Rainer Jungwirth [1], **Christian Pfleiderer** [1], **Nico Wieschalla** [1, 2], **Wolfgang Schmid** [1, 2]
[1] *Technische Universität München, Physics Department, Institute E21, D-85748 Garching, Germany*
[2] *Technische Universität München, ZWE FRM II, D-85748 Garching, Germany*

Changes of thermal conductivity during in-pile irradiation are of central importance for the large-scale use of U-Mo/Al dispersion fuel. Recently it was shown [1], that heavy ion bombardment of U-Mo/Al dispersion fuel allows to simulate the effects of radiation damage during in-pile irradiation. Heavy ion bombardment avoids (strong) activation of the specimens. They may therefore be readily examined in simple laboratory experiments. We developed of a new method to determine changes of the thermal conductivity of U-6wt%Mo/Al and U-10wt%Mo/Al dispersion fuel due to ion bombardment. We derive changes of the DC thermal conductivity from a low frequency heat current as tracked by a digital lock-in technique. A comprehensive set of tests has been carried out that establishes the basic feasibility of our method to determine small changes under irradiation [2].

Figure 1 shows the experimental setup we used to determine the amplitude and the phase of the heat wave in our samples on two different points by means of thermocouples. Data were recorded at frequencies in the range 10mHz to 140mHz, where a typical example is shown in Fig. 2. The difference of the amplitudes and the phases of the temperature along the sample showed a strong frequency dependence, in excellent qualitative agreement with the simple model of a semi-infinite thermal conductor [3].

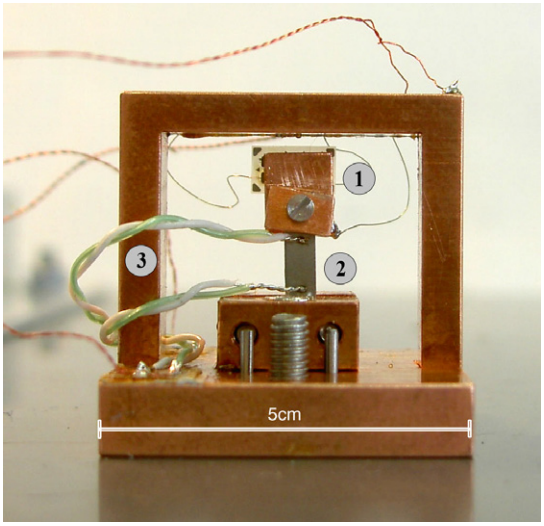

Figure 1: Experimental setup for low frequency measurements of a heat wave in small samples (2). A heater is mounted on top of the sample (1). The heat wave propagates from the heater through the sample into the Cu frame, which acts as a heat sink. The amplitude and the phase of the temperature wave are detected with two thermocouples at nV resolution (2).

The thermal diffusivity of the sample may be calculated independently from the frequency dependence of the difference of amplitude and phase of the heat wave, respectively (cf. Fig. 2). The thermal conductivity derived from the amplitude and phase were thereby in fair quantitative agreement. In particular, we were able to show that our method allows to resolve tiny changes of the thermal conductivity caused by heavy ion bombardment, when measuring the diffusivity of the samples before and after irradiation with the thermocouples kept in a fixed position. The changes in thermal diffusivity were confirmed through measurements of the electrical conductivity as related to the thermal conductivity in terms of the Wiedemann-Franz law. An unresolved issue is at present, that absolute values of the thermal diffusivity are a factor 30 smaller than typical values observed for other nuclear dispersion fuels such as U_3Si/Al [4]. We trace these differences to the rather strong approximations underlying the model that is presently used for data analysis.

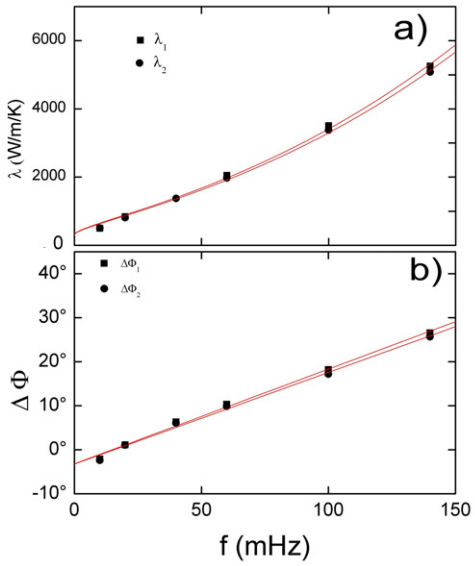

Figure 2: Inverse of the amplitude difference of the heat wave at two points of the sample (a) and the phase difference of the heat wave at two points on the sample (b) as function of frequency. The amplitude difference (a) is best fitted with a function of the form $y = P_0 \exp(P_1 \cdot x)$. The phase difference is well accounted for with a function $y = P_3 + P_4 \cdot x$ [3]. Parameters P_1 and P_4 may be used independently from each other to determine the thermal diffusivity of the sample.

References

[1] Nico Wieschalla. *Heavy ion irradiation of UMo/Al dispersion fuel.* Dissertation, TUM, 2006.
[2] Rainer Jungwirth. Thermische und elektrische Leitfähigkeit von hochdichten Uran-Molybdän-Kernbrennstoffen. Diplomarbeit, Technische Universität München, 2006.
[3] H. Carslaw and J. Jaeger. *Conduction of heat in solids.* Oxford Science Publications, 1959.
[4] C.K. Kim et al. Effect of particle shape and distribution on thermal and electrical conductivities in U_3Si-Al dispersion fuels. *Journal of nuclear materials*, 209:315–320, 1994.

6

Instrument Development

6.1 First quasielastic measurements at RESEDA

Wolfgang Häußler [1, 2], **Dominik Streibl** [1], **Reinhard Schwikowski** [2], **Andreas Mantwill** [1], **Bodo Gohla-Neudecker** [2], **Rodrigo Caballero** [2], **Peter Böni** [1]

[1] *Technische Universität München, Physics Department, Institute E21, D-85747 Garching, Germany*
[2] *Technische Universität München, ZWE FRM-II, D-85747 Garching, Germany*

In 2006, first quasielastic scattering measurements at the Resonance Spin Echo (NRSE) Spectrometer RESEDA have been performed. In order to prepare RESEDA for these experiments, intensity and polarization of the primary beam was optimized. At first, high radiation background produced in the first spectrometer arm and at the sample region (Fig. 1) was shielded with movable lead walls. Now, usage of the full beam is possible at RESEDA, in contrast to previous measurements using attenuators in front of the spectrometer.

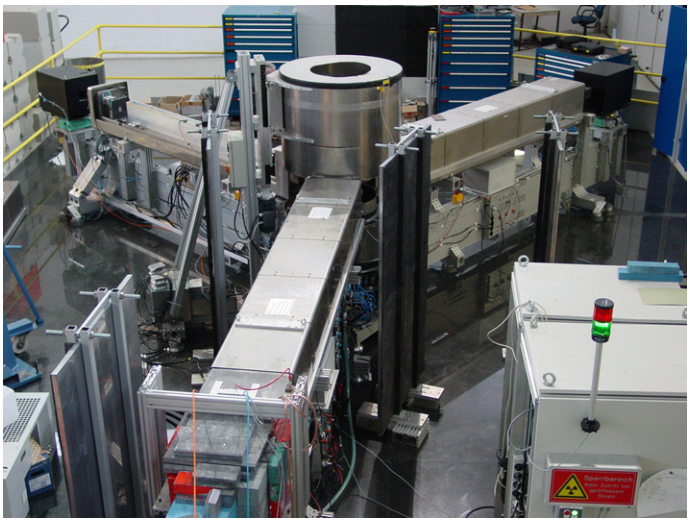

Figure 1: The instrument RESEDA with its two secondary spectrometer arms. The mumetal shielding of the left arm is removed and gives free view on the NSE and NRSE coils.

Test measurements of the polarization as a function of the wavelength of the primary beam and its divergence were performed. For the latter, movable slits were installed in the first spectrometer arm. The beam divergence was determined by the relative position of the slits. From measurements with the beam divergence varied it became clear, that the polarization decreased with increasing divergence, that means with increasing number of reflections in the NiTi guide. Thereafter, the guide field around the neutron guide was enforced from 80 G to 250 G. These measures improved the polarization. However, it was still not perfect, especially at high beam divergence.

Nonetheless, the performance of RESEDA could be demonstrated by first quasielastic test experiments. The sample consisted of the protein Cytochrome C (140 mg/ml) in aequeous solution. The velocity selector was accelerated to 22000 rpm, providing a mean wavelength 5.3 Å with a wavelength spread of 12 % (FWHM). We used the NSE setup at small spin echo times (0.01-0.064 ns), the NRSE setup at inter-mediate (0.16-1.2 ns) and the BNRSE setup at large spin echo times. The RF frequency was tuned to values between 35 kHz and 371 kHz leading to spin echo times up to 4 ns. Typical intermediate scattering functions are shown in Fig. 2, together with exponential fit functions. All data have been normalized by the resolution function determined by using a standard elastic scattering sample (graphite). As seen from Fig. 2, the decay rate of the relaxation function increases with increasing scattering vector $\mathbf{Q}$, as expected for center-of-mass diffusion. The decay rates are in good agreement with the Cytochrome particle size (15x17x17 Å^3). The size of the error bars is comparable to the symbol size, and was due to the still not optimum primary beam polarization.

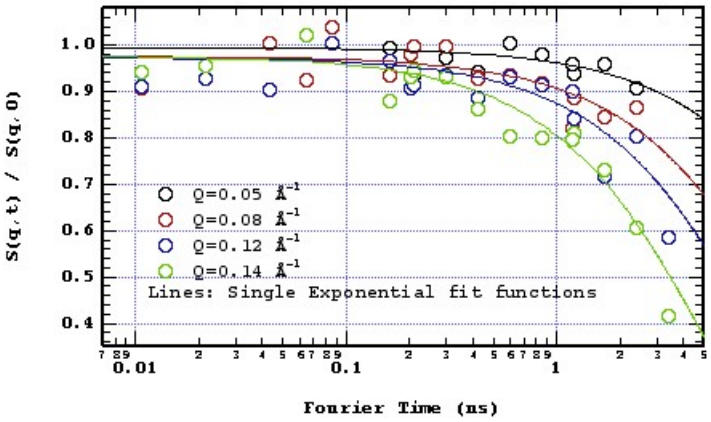

Figure 2: Intermediate scattering functions of Cytochrome C measured by means of NSE, NRSE and BNRSE. The scattering angle is varied between 2.5 and 7 degree, leading to the scattering vector values as indicated in the plot.

Further optimization of the polarization was abandoned, however, because the whole guide system had anyway to be removed after the quasielastic test experiments described above, due to non-tolerable activation of the polarizing guide. Therefore, the measurements at RESEDA were stopped in July 2006. Taking notice of the limited time-frame for experiments, it is clear that these results at RESEDA during 2006 were only possible thanks to the efficient use of the available neutrons. A new guide system is in preparation, and a new polarizer (cavity) will be installed in early 2007 in front of RESEDA.

During the second half of 2006, several improvements have been performed at RESEDA. Almost all axes were supplied with encoders, in order to prevent uncontrolled movement of instrumental components, for example of the sample environment and the detectors. In addition, the NRSE coils are going to be supplied with motorized goniometers and rotation tables, in order to provide fast and efficient positioning of the coils. Finally, new NSE coils, used for measurements at small spin echo times are in preparation. The previously used coils produced relatively inhomogeneous magnetic field integrals provoking a resolution gap between the NSE and the NRSE spin echo times. The new coils possess better field integral homogeneity, and, in addition, are designed more compact.

As soon as the new guide system, including the polarizer, is installed in early 2007, RESEDA will be finally commissioned, including readjustment of the coils, and usable for routine user experiments - provided enough staff is available.

6.2 Further progress with MuPAD at the FRM-II

M. Janoschek [1, 3], **R. Georgii** [1, 2], **P. Böni** [1]
[1] *Physics Department E21, Technical University Munich, 85747 Garching, Germany*
[2] *ZWE FRM-II, Technical University Munich, 85747 Garching, Germany*
[3] *Laboratory for Neutron Scattering ETHZ & PSI, CH-5232 Villigen PSI, Switzerland*

In 2005 we completed the R & D phase for the *Spherical Neutron Polarimetry* (SNP) device MuPAD (**Mu**-Metal **P**olarisation **A**nalysis **D**evice) in a joint venture with the Paul Scherrer in Switzerland (PSI) [1]. One full featured version of this device was already tested in September 2005 mounted on the cold three axis spectrometer TASP at PSI [2]. In January 2006 the construction of the second MuPAD device for the Munich research reactor FRM-II was finished as well. First tests were performed in February with the MuPAD option installed on the multi-purpose *very cold neutron* (VCN) beamline MIRA (s. Fig.1). A maximum of about 87 % in polarization could be guided through the zero field chamber of MuPAD. The four precession coils of MuPAD could be calibrated with ease. A calibration curve is shown in Fig.2.
Additionally to extensive tests on MuPAD itself we performed detailed checks to integrate MuPAD in the measurement environment of MIRA. E.g., the algorithm for the calculation of the currents in MuPAD's precession coils was integrated in MIRA's control program to guarantee an easy operation of the device. Further, it was tested that the FRM-II sample tube cryostat (CCR) can be operated inside MuPAD without disturbing the zero field sample environment.
The quality of the calibration can be tested by measuring a full polarization matrix on a nuclear Bragg peak. On such a peak all off-diagonal terms should be zero whereas the diagonal elements should have the magnitude of the initial polarization vector because a pure nuclear Bragg peak does not turn the polarization vector. On MIRA such a test could not be performed as the VCN spectrum of its neutron guide with a cutoff below 8 Å does not allow to reach any nuclear Bragg peak. Therefore the quality of the calibration was checked by measuring a matrix in the direct beam which should have a form similar to a matrix measured on a nuclear Bragg. A matrix observed in the direct beam is shown in Table 1. The deviations from zero on the off-diagonal terms are most probably due to the guidefields on the monochromator side of the instrument which enter the shielding of MuPAD. However, the matrix still shows that MuPAD performs excellently especially for the wavelength of 9.7 Å used in the experiments. To stress this point we note that the polarization vector of a neutron with 9.7 Å travelling through a field of 300mG (the order of magnitude of the Earth's magnetic field) over 1 cm is turned by 7.7°. Therefore already relatively weak fields disturb the experiment significantly and render it a very demanding task. The largest deviation in an off-diagonal term is about 0.071, which corresponds to 4.6°. We therefore conclude that despite the fact that MIRA in its present form is not an ideal host instrument for MuPAD due to the VCN spectrum we could demonstrate that MuPAD performs excellent under the given conditions.

Figure 1: MuPAD installed on MIRA at the FRM-II.

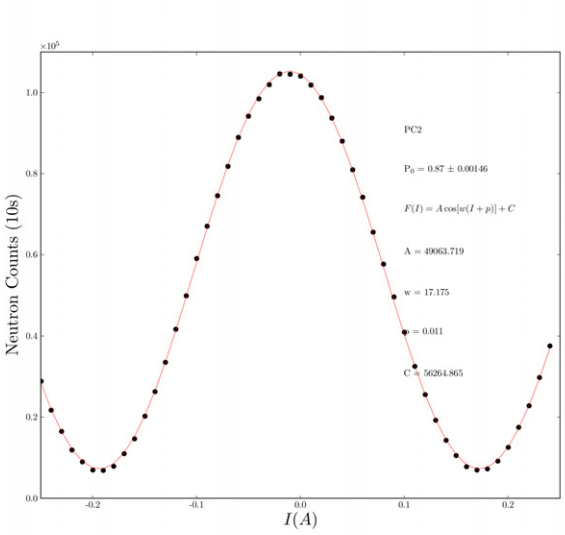

Figure 2: A calibration curve for one MuPAD precession coil on MIRA.

P_{out}		x	y	z
P_{in}	x	0.865(2)	-0.071(4)	0.061(4)
	y	0.069(4)	0.873(2)	0.009(4)
	z	-0.030(4)	0.005(4)	0.880(2)

Table 1: Polarization matrix measured in the direct beam. P_{ij}: i and j are the directions of incident and final polarization vector, respectively with x along the scattering vector, z perpendicular to the scattering plane and y completing the right hand coordinate system.

References

[1] S. Klimko, M. Janoschek, B. Roessli, R. Gähler, and P. Böni. *Annual Report E21*, pages 18–19, 2005.
[2] M. Janoschek, S. Klimko, B. Roessli, M. Medarde, and P. Böni. *Annual Report E21*, page 21, 2005.

6.3 MIRA – The beam line for very cold neutrons at the FRM-II

Robert Georgii [1, 2], **Peter Böni** [1], **Helmut Fußstetter** [2], **Andreas Mantwill** [1], **Reinhard Schwikowski** [2, 1]

[1] *Physics Department E21, Technische Universität München, 85747 Garching, Germany*
[2] *ZWE FRM-II, Technische Universität München, 85747 Garching, Germany*

MIRA is a versatile instrument for very cold neutrons (VCN) using neutrons with a wavelength $\lambda > 8$ Å (see Fig. 1). The flux at the sample position is $5 \cdot 10^5$ neutrons/(cm^2 s) unpolarised. It is situated at the cold neutron guide NL6b in the neutron guide hall of the FRM-II. As the instrument set-up can be changed quickly, MIRA is ideally suited as a testing platform for realizing new instrumental set-ups and ideas. In particular, MIRA is unique in its possibilities of combining different neutron scattering methods as:

- Polarized or non-polarized reflectometry.
- Sperical Polarimetry
- Polarized or non-polarized small angle scattering (SANS).
- Classical NRSE (Neutron Resonance Spin Echo) setup as well as using the MIEZE principle.

This year MIRA was successfully operated for 5 reactor cycles,**it means for 260 days (!)**. In total, 28 external and 33 internal proposals, several test and service measurements were performed. Selected examples are shown in the sections 1.5, 1.3, 2.1, 2.2, 6.11, 6.12, 2.3, 6.6. One Ph.D. thesis (Multi-Mieze measurements by Nikolas Arend (FRM-II)) and serval measurements for Diploma thesis were finished using mainly data from MIRA.
A new polarising multilayer monochromator was taken into operation. This allows now full polarisation analysis (see section 2.3), 3D-polarimetry (see section 6.2) and spin echo measurements. Both NRSE, in particular SESANS (see section 6.7) , and MIEZE (see section 6.4) measurements are now possible. The MSANS principle was tested (see section 6.5) for later operation on MIRA. The existing magnet was upgraded for automatic adjustment of the field perpendicular to the neutron beam and independent from the sample movement.

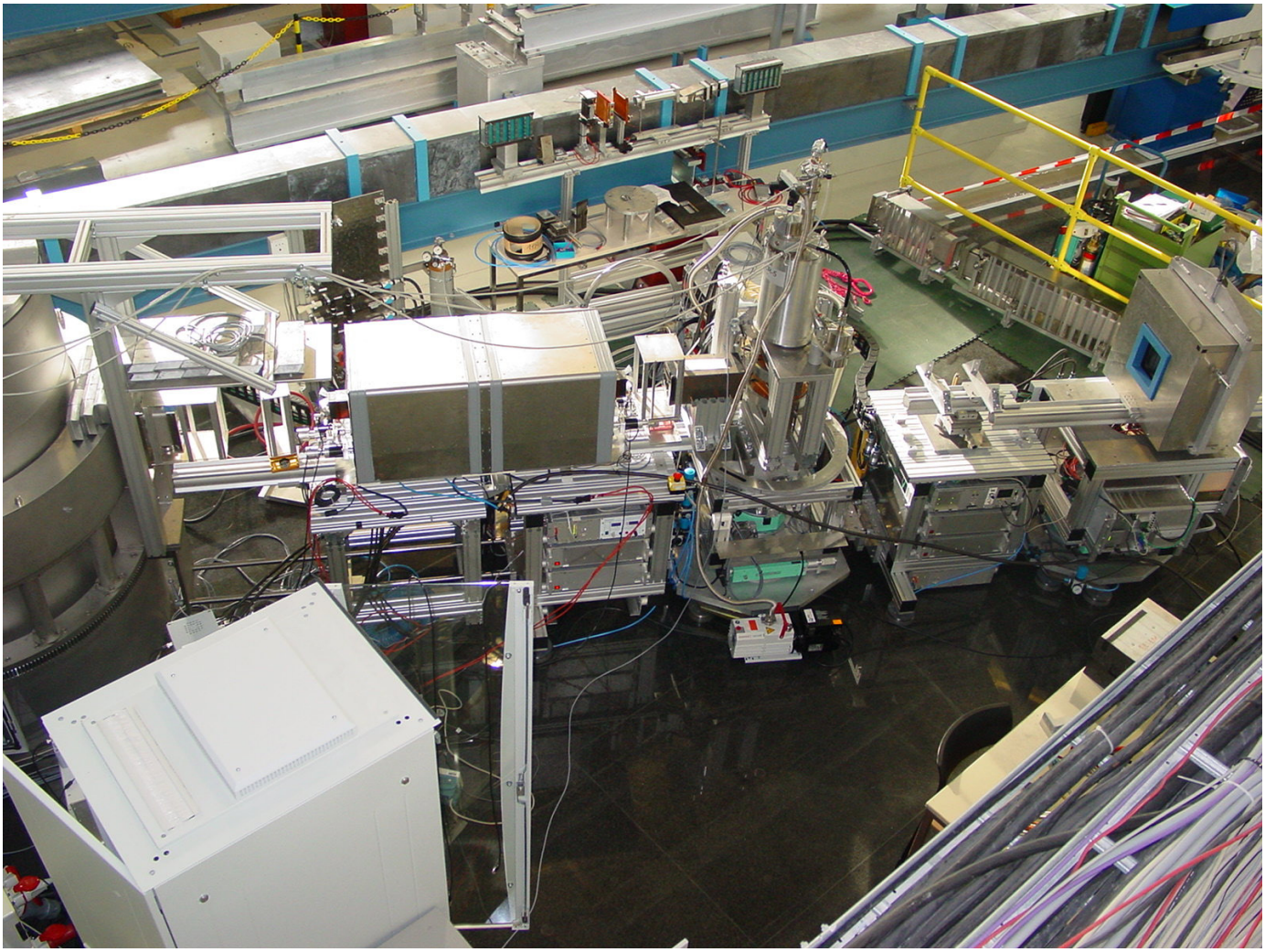

Figure 1: MIRA equipped with the MIEZE option, a closed cycle cryostat and a magnet.

6.4 MIEZE and Multi-MIEZE experiments at MIRA

N. Arend [1, 2], **R. Georgii** [1, 2], **W. Häußler** [1, 2], **S. Mühlbauer** [1, 2], **R. Gähler** [3], **P. Böni** [1]
[1] *Physics Department E21, Technical University Munich, 85747 Garching, Germany*
[2] *ZWE FRM-II, Technical University Munich, 85747 Garching, Germany*
[3] *Institut Laue-Langevin, F-38042 Grenoble, France*

In order to establish the MIEZE and NRSE techniques as standard measurement options at the instrument MIRA, new resonance spin echo hardware has been built and tested during the last few years. In 2006 several different measurements using MIEZE/NRSE have been performed, among those are

- verification of the Multi-level MIEZE principle
- SESANS measurements using NRSE (see 6.7)
- MIEZE measurements with strong magnetic fields and a cryostat at the sample region

Verification of the Multi-level MIEZE principle

The time-dependent, high-frequency sinusoidal signal of a MIEZE instrument can, just like the signal of an NSE/NRSE instrument, be used for quasi- and inelastic measurements with a wide range of applications. The MIEZE instrument, however, has a strong connection with a time-of-flight interferometer and is therefore potentially well-suited for fundamental physics experiments. One such application is the verification of the longitudinal Stern-Gerlach effect, which manifests itself in the temporal splitting of the spin-up and spin-down states of a cold neutron beam when passing through resonantly tuned fields of an NRSE flipper coil.

To actually see the splitting of a cold neutron pulse, such pulses must have a sharp width and a sufficient separation in time. These prerequisites are difficult to achieve by conventional beam chopping. A Multi-level MIEZE instrument, which could provide those kind of pulses, consists of several stacked single MIEZE parts, all tuned to have a common focusing point. This principle and the predicted pulse form and sharpening [1] was successfully verified at MIRA with a two-level setup. Fig. 1 shows the single and two-level signals and the respective non-linear fits.

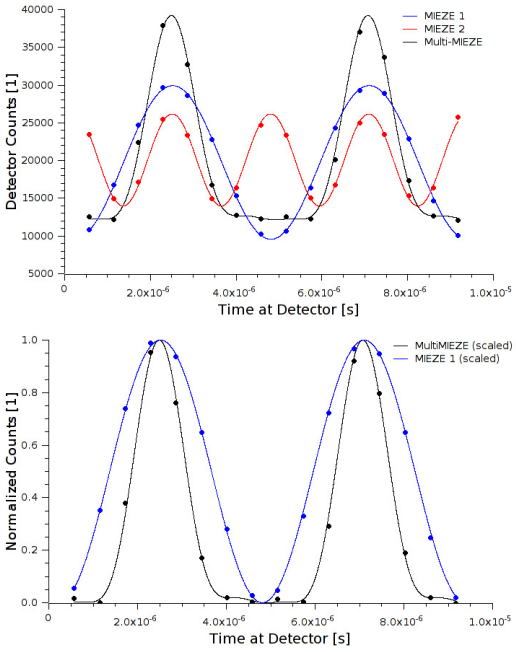

Figure 1: MIEZE and Multi-level MIEZE signal data with fits.

MIEZE measurements

One of the strengths of MIEZE is the freedom the experimenter has in arranging the sample region compared to conventional NRSE. Since the MIEZE signal is already prepared after the second analyzer, it is easily possible to e.g. apply strong magnetic fields, do measurements on ferromagnetic samples, or realize long scattering geometries.

Since these advantages do not seem to have been fully recognized in the past, we performed a showcase measurement: A MIEZE setup at MIRA was equipped with a 2 kG solenoid and a cryostat (see Fig. 2). The magnetic field at the sample region was gradually increased while monitoring the contrast of the MIEZE signal. If the strong magnetic field (i.e. its stray fields) would have destroyed the beam polarization, the initial contrast of $\approx 80\%$ would have decreased significantly. The 2D scan in Fig. 3 shows that this was not the case, proving the suitability of MIEZE for such measurement environments. An interesting sample to investigate with MIEZE is e.g. MnSi with its chiral magnetic structure that is revealed at low temperatures and high magnetic fields.

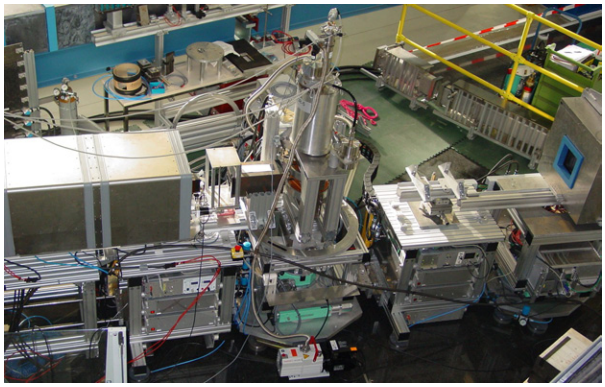

Figure 2: MIEZE setup with a strong solenoid and cryostat at the sample region.

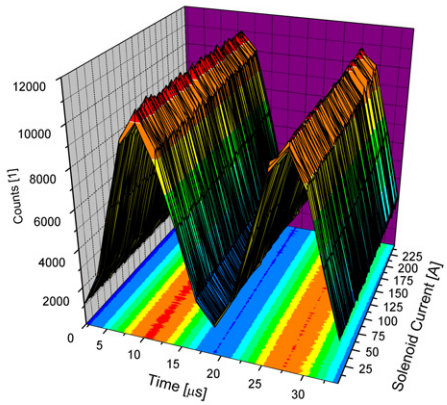

Figure 3: 2D scan of MIEZE signal vs. solenoid current. The signal contrast of approx. 80% is more or less unaffected.

References

[1] N. Arend, R. Gähler, T. Keller, R. Georgii, T. Hils, and P. Böni. *Physics Letters A*, 327/1:21–27, 2004.

6.5 Multiple Small Angle Neutron Scattering (MSANS) on MIRA

Thomas Hils [1], **Roland Gähler** [2], **Peter Böni** [1], **Robert Georgii** [1, 3]
[1] *Physics Department E21, Technische Universität München, 85747 Garching, Germany*
[2] *Institut Laue-Langevin, F-38042 Grenoble, France*
[3] *ZWE FRM-II, Technische Universität München, 85747 Garching, Germany*

Small angle neutron scattering (SANS) is a powerful method for measuring lateral correlation lengths in the 0.01 to 0.1 μm range. The method finds applications in biology, polymer physics, material science etc. The corresponding Q-range is around $5 \cdot 10^{-3}$ nm^{-1} to 5 nm^{-1}. The aim of our proposed MSANS (multiple SANS) is to increase the Q-resolution by at least an order of magnitude compared to SANS at equal intensity extending the measurement of correlations to a scale of several microns. In conventional SANS this would lead to an unacceptable loss of intensity by a factor of 10^{-4}. As an alternative one can overlay multiple individual beams (up to 10^4). With MSANS an incoherent superposition of multiple beams is achieved increasing usable divergence and thus intensity. Moreover, the scattering pattern is two-dimensional and not restricted to one dimension as in the commonly used USANS technique.

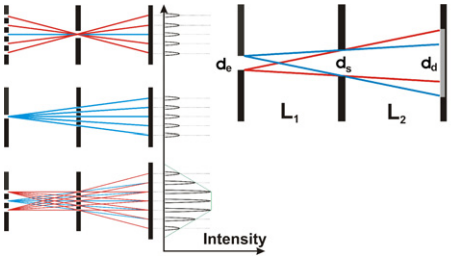

Figure 1: (Left) The number and the intensity of the spots depends on the number of holes of the sample and the entrance mask. (Right) The diameter d_d of the spots on the detector depends on the width of the entrance and sample apertures.

The proposed MSANS is a new USANS option for a standard long baseline SANS instrument. It uses the common SANS infrastructure except for the detector, which requires enhanced spatial resolution. We aim at improving the Q-resolution to about $10^{-5}\mathring{A}^{-1}$ at 10 Å, so that correlations up to 60 μm can be measured. Using multi-hole apertures at the entrance (M_e) of the collimator and near the sample (M_s) with lattice constants a_e, a_s and hole diameters d_e, d_s respectively and with the choice (Fig. 1)

$$G_{e,s} = \frac{2\pi}{a_{e,s}} \; ; G_e \cdot L_1 = (G_s - G_e) \cdot L_2 \; ; G_d = G_s - G_e$$

an intensity pattern of well separated peaks with lattice constant a_d in the detector plane is observed ($a_d = 2\pi/G_d$).

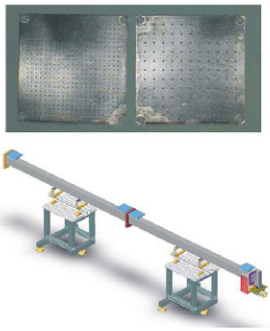

Figure 2: (Bottom) MSANS setup. The apertures are placed inside evacuated tubes at the beginning and at the centre of the flight path. (Top) Multi hole apertures made of Cd and coated with TiB.

Short range correlations in the sample may lead to significant overlap, however typical SANS intensities drop very rapidly with increasing Q and overlap will not be fatal in many cases. Sets of apertures (Fig. **??**) with different relations $a_{e,s}$ / $d_{e,s}$ can be used to adapt the pattern to the demand. For an ideal MSANS, the resolution is decoupled from the intensity, as long as the area of the openings of the apertures is kept constant. The increase in Q-resolution in MSANS is typically one order of magnitude, compared to SANS at equal intensity. The gain originates from the reduction in Q-range in MSANS and the increase of the cross section of the guide and its divergence.

Fig. 3 shows a preliminary MSANS pattern using an image plate detector and a cut along the y-direction. From the data we obtain a peak width at the detector of 1.5 mm. Therefore, lateral correlations of the order of 3.8 μm can be measured. This value is a lower limit because the detector was in saturation for the largest intensities. Of course, the resolution can be increased further by increasing the distance between the entrance and exit apertures from 6 m (MIRA) to 40 m (conventional SANS). In order to increase the intensity of the instrument, the apertures at the sample position may be replaced by small lenses [**?**].

This work was supported by the European Union within the Sixth Framework Program FP6 under contract no. 505925.

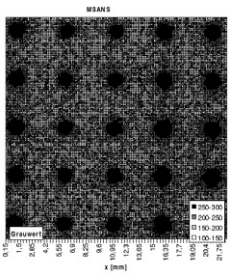

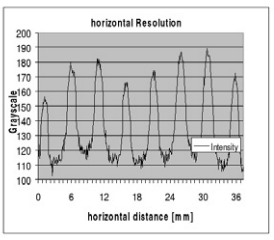

Figure 3: (Left) 2d-Intensity map (arbitrary units) showing resolution in real-space. (Right) Approximation of horizontal resolution due to direct superposition of intensity in y-direction.

6.6 MIRA test of a neutron polarizing ^{3}He spin flipper, the "Flipperizer"

Earl Babcock [1], **David Jullien** [1], **Alexander Petroukov** [1], **Robert Georgii** [2, 3]
[1] *Institut Laue Langevin, 38042 Grenoble, France*
[2] *Physics Department E21, Technische Universität München, 85747 Garching, Germany*
[3] *ZWE FRM-II, Technische Universität München, 85747 Garching, Germany*

The principle of AFP has been well know to atomic physics for many years. AFP uses an oscillating RF field at the ^{3}He Larmor precession frequency, $\nu = \gamma$B, where γ is the gyromagnetic ratio and B is the static magnetic holding field. This creates a circularly precessing effective field given by,

$$\mathbf{B_{eff}} = \left(B_0 + \frac{\omega}{\gamma}\right)\hat{\mathbf{k}} + B_1\hat{\mathbf{i}}. \quad (1)$$

This effective field only interacts with the ^{3}He spins near to the resonance created by the Larmor precession, if this rotating effective field is swept through the Larmor frequency, either by changing field or frequency, at a rate slow compared to the Larmor frequency in the rotating frame, then the ^{3}He will be flipped. In addition to the adiabatic condition we must also add the condition that the AFP sweep must be fast compared to the rate of transverse spin relaxation in the rotating frame. Combining these two conditions we arrive at the AFP parameters given as,

$$\gamma B_1 \gg \frac{\dot{\omega}}{\gamma B_1} \gg D\frac{|\Delta B_z|^2}{B_1^2} \quad (2)$$

where D us the diffusion coefficient and ΔB_z is the field gradient of the D.C. holding field.

For our AFP ^{3}He flipper we decided to take advantage of our standard ^{3}He passive magnetostatic cavity, the small Magic Box, and install a sweepable high power RF field inside it in order to perform the AFP. This allowed us to drive an AFP sweep at sweep rates of 2.5 to 7.5 ms with a frequency span of 2.5 kHz to 17 kHz at varying amplitudes which corresponded to a maximum RF magnetic field on the order of 1-2 G. To create the required transverse magnetic field inside the μ metal shielding of the magic box we utilized a rectangular solenoid designed to fit just inside the magic box. This solenoid consisted of 40 turns spaces approximately 4mm on center for the first 4cm, 1.2mm on center for 24cm and 4mm on center for the last 4cm making a 32cm long coil. A picture of the installation on MIRA is shown in figure 1.

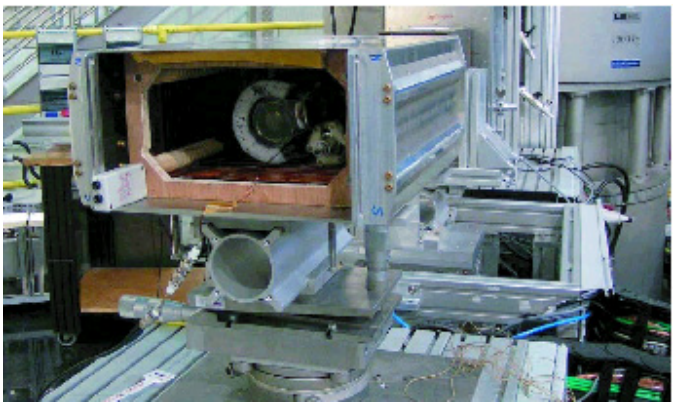

Figure 1: Picture of the AFP flipper coil in the magic box installed on MIRA.

Preliminary tests to determine the amount of ^{3}He polarization loss per flip where conducted at the ILL by monitoring the decay of the ^{3}He polarization using NMR FID to measure the relative ^{3}He polarization in situ in between AFP flips. These test showed that roughly 20.000 flips where required to relax the ^{3}He polarization by only 10% .

We then took the apparatus with the new solenoid coil described above to MIRA for final tests on neutron beam in order to show the on beam lifetime and neutron flipping efficiency. We used an incident beam of 10Å which was polarized with an S-bender with a 98.5% polarizing efficiency. This polarizing efficiency was verified using an opaque spin filter cell with approximately 12bar cm of ^{3}He. Polarized ^{3}He gas was provided in ILL spin filter cells by the HELEOS MEOP station at pressures from 0.7 to 1.2 bar.

Optimization was performed by varying parameters. A typical data sequence consisted of one NMR FID pulse to obtain relative ^{3}He polarization, count neutron transmission for anywhere from 10 to 30 seconds, perform 100 AFP flips of the ^{3}He, after which the ^{3}He polarization had a net reversal, then recount neutrons in the anti-parallel state. This cycle was repeated continuously for about 6 hours, after which the number of flips per sequence was changed to 1, holding the cycle time constant, thus allowing us to measure the ^{3}He T_1 decay in the absence of the extreme number of AFP flips.

Results of the test are shown in figure 2. As shown the ^{3}He polarization loss per AFP was 2×10^{-5}. The T_1 decay was measure to be only 30 hours however we postulate this was due to interference from electronics below the ^{3}He cell on the neutron beam position. To a large accuracy it was difficult to determine the optimal settings for the flipper, because it gave nearly indistinguishable results over a broad range of parameters. However it is certain that the highest amplitude settings, from 32 to 40 volts with the 7.5ms time and 17kHz width gave robust results like the ones shown in figure 2.

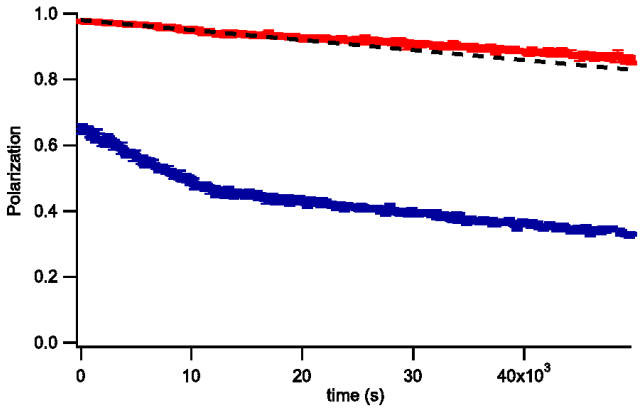

Figure 2: Results showing loss versus time, there was on average one flip per second during the fit portion of the data. Fit is and exponential.

6.7 First SESANS experiments at MIRA

W. G. Bouwman [1], **V. O. de Haan** [1], **J. Plomp** [1], **N. Arend** [2, 3], **R. Georgii** [2, 3], **W. Häußler** [2, 3]
[1] *Faculty of Applied Science, Delft University of Technology, Delft, the Netherlands*
[2] *Physics Department E21, Technical University Munich, 85747 Garching, Germany*
[3] *ZWE FRM-II, Technical University Munich, 85747 Garching, Germany*

SESANS is a neutron scattering method that combines the techniques of Small Angle Neutron Scattering (SANS) and (Neutron Resonance) Spin Echo to determine the structure of materials [1, 2, 3, 4]. To compensate the divergence of the neutron beam, the spin echo coils are tilted with respect to the beam direction. In contrast to conventional SANS, samples with particle sizes up to the μm range are accessible and the intensities can be significantly higher.

In the first half of the instrument a certain amount of Larmor precession is generated by the parallelogram shaped (tilted) magnetic field region with an inclination angle of ϑ_0. In the second half of the instrument this precession is compensated (echo) by a copy of the first half with an opposite magnetic field. The potential scattering of a sample, placed in the centre of the instrument, will disturb this echo condition and depolarize the neutron beam. The depolarisation is a function of the magnetic field amplitude B, coil distance L, and wavelength λ. We can introduce an instrumental parameter, the so-called spinecho length

$$z = \frac{2\,c\,B\,L\,\lambda}{\pi}\,\cot\vartheta_0$$

that is the distance over which correlations are measured in the sample, with $c = 4.6368 \cdot 10^{14}$ T^{-1}m^{-2}. The theoretically expected signal of the normalized polarization [5],

$$P_n = P(z)/P_0 = \mathrm{e}^{\sigma\,t\,(G(z)-1)}$$

depends on both instrument parameters and sample properties: the sample thickness t, the scattered beam fraction per unit length of sample thickness σ, and the SESANS correlation function $G(z)$.

In October 2006 first SESANS measurements were performed at MIRA in collaboration with the Delft University of Technology (MIRA proposal no. 76) in order to investigate the instruments capabilities and current limitations for this measurement technique. It was the hope that, due to the long wavelengths of ≈ 10 Å available at MIRA, a signal from samples that scatter too weakly for the SESANS instrument in Delft could be detected.

For the measurements on the Delft samples, MIRA was set up in NRSE mode with a non zero-field sample region. The beam polarization was coupled out of the first and into the second NRSE arm using coupling coils and a guide field (so-called „ferromagnetic setup"). Although it is possible to conduct measurements in this configuration, an intrinsic polarization loss of 50% happens at the sample region. Therefore, the initial polarization P_0 was only around 38% at 69 kHz (and even lower for higher frequencies), as shown in Fig. 1 (left).

Since the distance L between the coils could not be altered due to technical reasons, the coil inclination ϑ_0 was changed to scan the spin echo length z. Because of depolarization and scattering effects, P_0 is also a function of z. The measured sample was a diluted suspension of polystyrene spheres with a radius of 220 nm, the results are plotted in Fig. 2 (left).

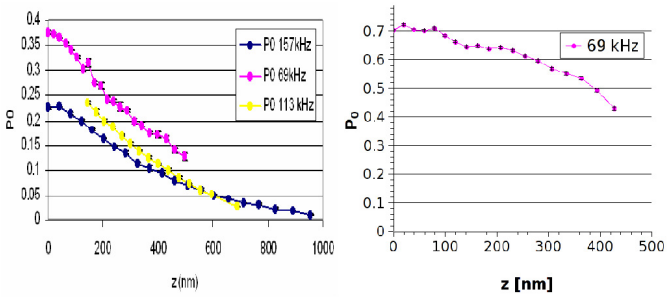

Figure 1: Initial polarization P_0 as a function of z: Delft proposal measurements (left) and repeated measurement at 69 kHz with zero-field sample region (right).

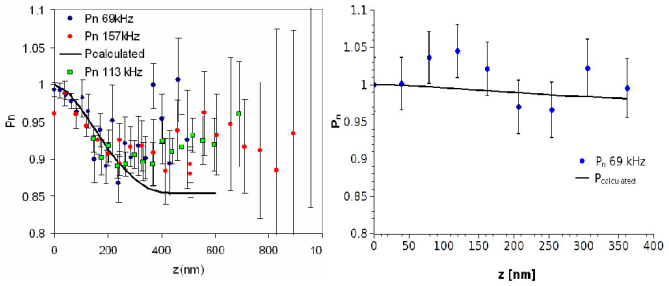

Figure 2: Normalized polarization of the measured sample as a function of z.

The low initial polarization and further depolarization and loss of scattered neutrons (most likely caused by the B_0 and coupling coils) led to significant errors and deviation from the predicted curve.

The proposal experiment was repeated shortly after, this time with a zero-field sample region installed. The initial polarization P_0 at 69 kHz was significantly higher (an expected factor of ≈ 2), as shown in Fig. 1 (right). Unfortunately, the only available sample of polystyrene spheres differed from the original sample with respect to dilution and sphere radius (472 nm). Therefore, the expected theoretical polarization decrease is relatively low, which the measurement supports (Fig. 2 (right)).

Although the first SESANS measurements at MIRA did not lead to results as good as we hoped for, the technical limitations were significantly improved with respect to the available polarization. With still further room for improvement, doing regular SESANS experiments at MIRA seems a promising task to pursue.

References

[1] T. Keller, R. Gähler, H. Kunze, and R. Golub. *Neutron News*, 6(16), 1995.
[2] R. Gähler, R. Golub, K. Habicht, T. Keller, and J. Felber. *Physica B*, 229(1), 1996.
[3] M. T. Rekveldt. *Nucl. Instr. and Meth. B*, 114(366), 1996.
[4] M. T. Rekveldt, W. G. Bouwman, W. H. Kraan, O. Uca, S. Grigoriev, S. Habicht, and T. Keller. In *Lecture Notes in Physics*, volume 601, pages 87–99. Springer, Berlin, 2003.
[5] W. G. Bouwman, W. Stam, T. V. Krouglov, J. Plomp, S. V. Grigoriev, W. H. Kraan, and M. T. Rekveldt. *Nucl. Instr. and Meth. in Physics Research Section A*, 529 (1-3)(16), 2004.

6.8 Performance of an elliptically tapered neutron guide - Measurements on MIRA and PANDA

Sebastian Mühlbauer [1], **Robert Georgii** [1, 2], **Peter Böni** [1], **Philipp Niklowitz** [1], **Peter Link** [2], **Martin Stadlbauer** [1, 2]

[1] *Technische Universität München, Physik Department E21, D-85747 Garching, Germany*
[2] *ZWE FRM-II, Technische Universität München, D-85747 Garching, Germany*

Supermirror coated neutron guides are used at all modern neutron sources for transporting neutrons over large distances. In order to reduce the transmission losses due to multiple internal reflection of neutrons, ballistic neutron guides with linear tapering have been proposed and realized. However, these systems suffer from an inhomogeneous illumination of the sample. We propose using elliptically tapered guides that provide a more homogeneous phase space at the sample position as well as a focusing at the sample. Moreover, the design of the guide system is simplified because ellipses are simply defined by their long and short axes. We have investigated the focusing properties of an elliptic neutron guide prototype with neutrons. The width and height of the entrance and exit of the guide is 4×8 mm and the length of the guide is 2 m. The focal points F_1 and F_2 are situated 80 mm from the ends of the guide. It is divided into four sections with an individual length of 500 mm. The walls are coated with supermirror $m = 3$. The experiments show that the predicted gains using the program package McStas are realized [1] and confirm earlier measurements [2].

Measurements on MIRA

In addition to the experiments performed on MORPHEUS at SINQ [2], further experiments have been performed on MIRA with a cold neutron beam (wavelength 10Å). The four sections of the elliptic guide were aligned by means of a theodolite. A point aperture of 1 mm diameter, followed by an isotropic scatterer (2 mm water) were placed in one focal point of the guide system. The guide system was inclined at an angle of 3°, to avoid contamination of the direct beam in the guide entrance aperture and to ensure a homogeneous illumination of the guide entrance. This was verified by imaging the empty beam profile without focusing guide. The neutron distribution after the guide exit was measured as a function of the distance from the guide exit to the detector plane. A ^{3}He wire detector (spatial resolution 2.2 mm) and an image-plate detector (spatial resolution 0.13 mm) were used.

Results

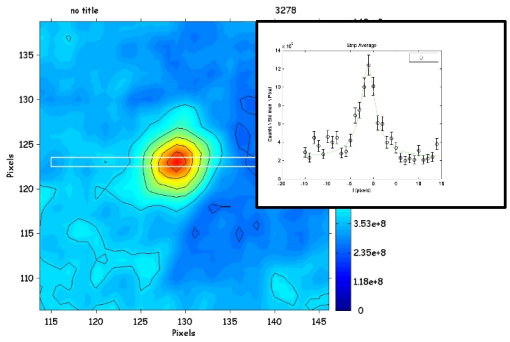

Figure 1: Neutron intensity distribution at the focal point f= 80 mm. The inset displays a horizontal cut through the focal spot.

Fig. 1 shows the neutron intensity distribution at the focal point. The sensitive detector area has a distance of 80 mm to the exit of the guide. The FWHM of the focal spot is only limited by the detector resolution. The FWHM of the focal point is 4±0.5 detector pixels or 2.8±0.35 mm. In Fig. 2 the focal spot is recorded with the image-plate detector, showing spot FWHM of 1.4 mm. Fig. 3 displays a horizontal cut, clearly showing the focusing properties of the elliptic guide.

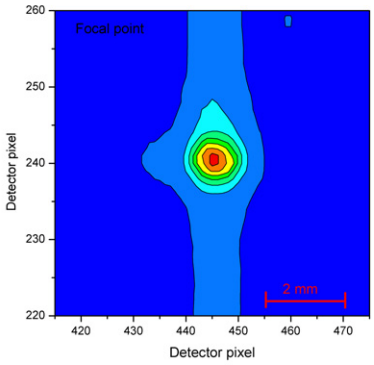

Figure 2: Neutron intensity distribution at the focal point f= 80 mm, recorded with the image plate detector.

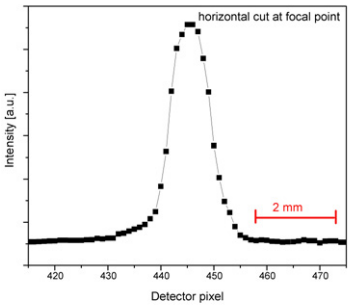

Figure 3: Neutron intensity distribution at the focal point f= 80 mm, horizontal cut through the focal spot.

Measurements on PANDA

To perform neutron diffraction experiments on a Ni_2S single crystal with a size of 1×1×0.1 mm, the elliptically tapered neutron guide was used on the cold triple axis spectrometer PANDA. For a more detailed description please refer to the report.

This work was supported by the European Union within the Sixth Framework Program FP6 under contract no. 505925.

References

[1] K. Nielsen and K. Lefmann. Mcstas, McStas webpage: http://neutron.risoe.dk/mcstas. *Physia B*, **283, 2000.**

[2] S. Mühlbauer et al. Performance of an elliptically tapered neutron guide. *Physica B*, **385-386, 2006.**

6.9 Elliptic neutron guide: focus on tiny sample for high-pressure experiments

P. G. Niklowitz [1], **S. Mühlbauer** [1], **P. Link** [2, 3], **P. Böni** [1]
[1] *Physik Department E21, Technische Universität München, 85747 Garching, Germany*
[2] *Institut für angewandte Physik, Technische Universität Dresden, 01062 Dresden, Germany*
[3] *ZWE FRM-II, Technische Universität München, 85747 Garching, Germany*

Elliptically shaped neutron guides are in principal ideally suited to concentrate the neutron beam in a small focal point with a very high neutron flux density.[1] Recently, the focusing capability of elliptic neutron guides has been demonstrated experimentally.[2] (See previous article in this report as well.) A 2 m long elliptic guide (4 parts with 50 cm length) with supermirror coating was used to increase the neutron flux density in a focal point with 0.8 mm diameter by a factor of 25 with respect to the original neutron beam.

An interesting application of elliptic neutron guides is their use in neutron scattering investigations of samples under pressure. In research areas like geoscience or magnetic quantum criticality often pressures of the order of 10^5 atmospheres have to be applied to the samples. Such pressures can be typically only created in a sample volume of the order of 1 mm^3.

In this experiment we have made use of the prototype of an elliptic neutron guide described above to focus a several centimeters wide neutron beam on a tiny sample. We chose NiS_2,[3] which crystallises in the cubic Pyrite structure with the Ni ions on an fcc sublattice. NiS_2 is an insulator with antiferromagnetic order below 39 K. NiS_2 becomes metallic at 25 kbar. At 75 kbar magnetism becomes completely suppressed in the low-temperature limit and magnetic critical phenomena can be studied. Therefore, neutron scattering measurements of NiS_2 at high pressure would be desirable. The sample dimensions were $1 \times 1 \times 0.1$ mm^3, which will be suitable to fit into appropriate pressure cells.

The experiment was carried out at the cold triple-axis spectrometer PANDA at FRM-II. The final wavevector was fixed to 1.5 $Å^{-1}$. A Be-filter was used to reduce higher-order contamination. The neutron camera DELCam built at FRM-II was used to measure the beam intensity at the sample position. The incoming beam was focused onto the sample with one 50 cm long end piece (focus 8 cm away from aperture). With the second end piece the focused beam was collected and converted back to a more parallel beam going to the detector. The sample, mounted on an Al holder with Cd and BN shielding, was cooled in a closed-cycle cryostat.

Due to the small size of the elliptic neutron guide's focus the alignment of the neutron guides with respect to the sample and spectrometer are important and difficult. The alignment was done in steps. Before mounting the sample in the cryostat the (200) and (020) nuclear Bragg peaks of the sample were used to align the two guide pieces with respect to each other, i.e. to ensure that the two focal points overlap. First, only the incoming focus was mounted and an intensity increase by a factor of 10 in a central spot with approximately 2 mm FWHM with respect to the original neutron flux density was observed with the DELCam neutron camera. Then, the sample was mounted, the outgoing focus added and the nuclear Bragg peaks maximised.

The sample was then mounted in the closed-cycle refrigerator and the nuclear Bragg peaks were recovered. Upon cooling the sample magnetic Bragg peaks appeared at (100) (see Figure 1).

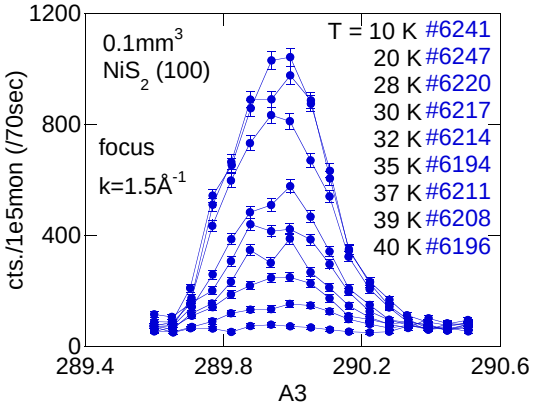

Figure 1: Formation of magnetic order upon cooling of NiS_2.

The (100) position is forbidden for nuclear Bragg reflections. In the low-temperature limit the magnetic moment of NiS_2 at zero pressure is 1 μ_B. The figure shows, that much smaller moments can be detected with reasonable counting time using the focusing neutron guides.

In order to measure the increase of the elastic signal by focusing the neutron beam the sample and elliptic guides were again carefully aligned. Then, the guides were replaced by diaphragms while leaving the remaining setup unchanged. A comparison of the $(0\bar{2}0)$ nuclear Bragg peak signals is shown in Figure 2.

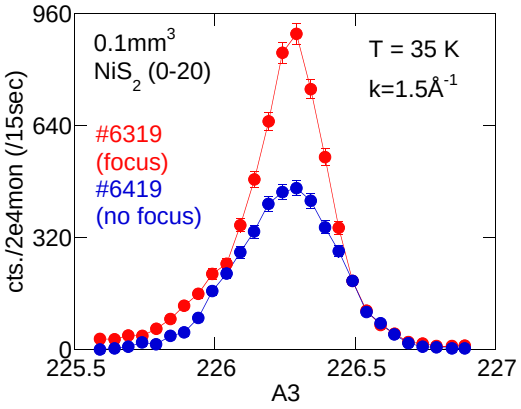

Figure 2: Increase of the elastic signal using elliptic neutron guides.

The increase is smaller than the intensity gain at the sample due to the increased divergence of the neutron beam around the sample, such that the Bragg condition is not fulfilled for all incoming neutrons. A much higher increase of the signal is expected for inelastic measurements.

This work was supported by the European Union within the Sixth Framework Program FP6 under contract no. 505925.

References

[1] C. Schanzer, P. Böni, U. Filges, and T. Hils. *Nucl. Instr. and Meth. A*, 529:63, 2004.
[2] S. Mühlbauer, M. Stadlbauer, P. Böni, C. Schanzer, J. Stahn, and U. Filges. *Physica B*, 385-386:1247, 2006.
[3] J. M. Honig and J. Spałek. *Chem.Mater.*, 10:2910, 1998.

6.10 An ultra-high-vacuum image furnace for intermetallic compounds

Andreas Neubauer [1], **Barbara Russ** [1], **Christian Pfleiderer** [1], **Andreas Erb** [2]
[1] *Technische Universität München, Physics Department E21, D-85748 Garching, Germany*
[2] *Walther-Meissner Institut, D-85748 Garching, Germany*

High-quality single crystals of intermetallic compounds are a prerequisite for detailed investigations of long-standing problems and the explorative search for novel electronic phases in condensed matter physics. Common techniques in the growth of intermetallic compounds include tetra-arc furnaces, Czochralsky systems and RF heated floating zone systems, while optically heated floating zone furnaces are widely used for oxide materials only. However, an advantage of image furnaces in floating zone techniques are, for instance, an improved stability of the molten zone. In recent years groups, e.g., in Dresden and Amsterdam, have successfully implemented image furnaces for the growth of intermetallic compounds [1, 2]. An important requirement are here high-purity conditions, notably that the sample space may be baked out to reach ultra-high vacuum (UHV) where the UHV conditions may be combined with an ultra-pure inert gas atmosphere.

We have implemented a four-mirror image furnace from Crystal Systems Incorporation (CSI), Japan, for the growth of single crystals of intermetallic compounds. The furnace was originally set-up in collaboration with H. v. Löhneysen at the University of Karlsruhe and recently transferred to München.

Figure 1 shows the central part of the image furnace, where four parabolic mirrors equipped with halogen lamps allow to heat samples to temperatures of up to 2200°C. First tests with the furnace as purchased showed the formation of oxide layers on intermetallic compounds. The sample chamber in our system has therefore been replaced completely by a UHV tight system that employs Helicoflex O-rings. When baking the system out we reach pressures of the order 10^{-9} mbar. An inert Ar atmosphere at pressures of up to 9 bar may be applied, where 6N Ar gas is additionally purified with a Pt-based hot catalytic getter furnace. Following these changes the oxide contamination was no longer present [3].

Since its transfer to München our image furnace has been tested on a number of oxide materials as well as certain intermetallic compounds. Figure 2 shows a typical picture taken during crystal growth. The molten zone may be seen in the central part of the picture. The resulting crystal (lower rod) and the feeding rod (upper rod) are typically rotated against each other. By moving the heating unit (lamps) upwards the molten-zone moves up as well and - in the best case, depending on the growth parameters - a single crystal grows.

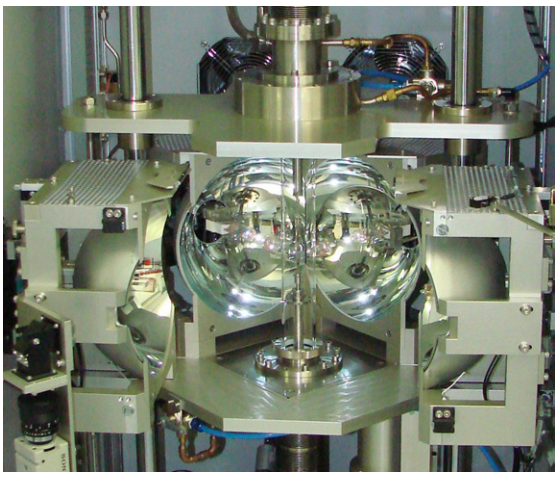

Figure 1: Central part of our modified CSI image furnace. Four parabolic lamps allow to heat samples in their focal point to temperatures of up to 2200° C. This is used for the growth of single-crystals by means of a floating zone method.

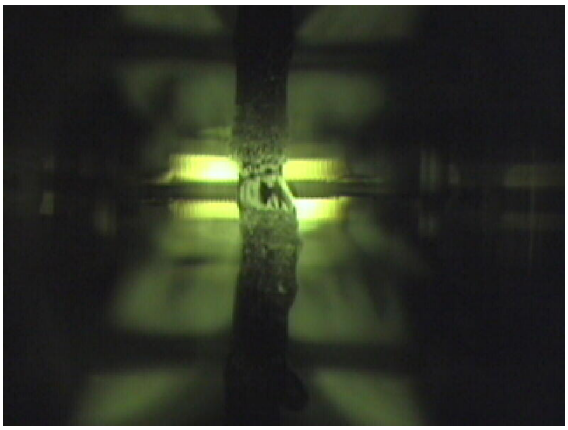

Figure 2: Picture of the growth zone in the image furnace as taken with a CCD camera.

References

[1] D. Souptel, G. Behr, W. Löser, A. Teresiak, S. Drotziger, and C. Pfleiderer. $CeSi_{2-\delta}$ single crystals: growth features and properties. *J. Crystal Growth*, 269:606, 2004.

[2] C. Pfleiderer, J. A. Mydosh, and Vojta M. Pressure dependence of the magnetization in URu_2Si_2. *Phys. Rev. B*, 74:104412, 2006.

[3] Julien Bœuf. *Untersuchungen an den antiferromagnetischen Übergangsmetallverbindungen Mn_3Si, CuMnSb und PdMnTe*. Dissertation, Universität Karlsruhe, 2003.

6.11 High m supermirrors with low internal stress

Christian Schanzer [1, 2], **Murat Ay** [1], **Jochen Stahn** [1], **Sebastian Mühlbauer** [3], **R. Georgii** [3, 4]
[1] *Laboratory for Neutron Scattering ETHZ & PSI, CH-5232 Villigen PSI, Switzerland*
[2] *SwissNeutronics, CH-5313 Klingnau, Switzerland*
[3] *Physics Department E21, Technische Universität München, 85747 Garching, Germany*
[4] *ZWE FRM-II, Technische Universität München, 85747 Garching, Germany*

New guide concepts, e.g. elliptic or parabolic guides, address the demands on future neutron optics. They enable i) to extract a proper phase space out of the source, ii) a transport of neutrons with low loss and iii) focusing beams onto small spots with high intensity. The later is adequate to probe e.g. novel materials, which are often only available in small quantities. Recently, the performance of an elliptic guide has been proven to be superior to conventional neutron guides by simulations. Moreover, the concept of an elliptic guide and according results of simulations has been experimentally verified using a miniaturized prototype. However, the reflection angles of the neutrons became rather steep within these devices, typically at short end sections where the radius of curvature is rather small. There, high m supermirrors are required to exploit the full performance. For large m values the number of layers increases drastically. Hence, interfacial roughness/interdiffusion and internal strain become crucial for the performance of the supermirrors, i.e. reducing the reflectivity and the stability of the supermirrors. Here we report on the performance of a supermirror with m = 5 showing high reflectivity but low film stress also.

The m = 5 supermirror was prepared by DC magnetron sputtering using the sputtering plant of SwissNeutronics. The substrate is float glass with a size of 50 x 500 mm^2. The sputter conditions where optimized to keep the stress in the film low. According measurements show a tensile stress of only ≈ 65 MPa. Neutron reflectivity measurements were performed at the instrument MIRA at the FRM-II using a monochromatic beam with $\lambda = 0.96$ nm.

Fig. 1 depicts the neutron reflectivity profile of the m = 5 supermirror. The reflectivity at the critical edge of the supermirror is about 68 %. Unfortunately a failure occurred during the deposition process. Therefore one layer is missing, causing the dip around m ≈ 3.2.

This result demonstrates the feasibility of high m supermirrors with excellent reflectivity and low film stress prepared by DC magnetron sputtering on large areas.

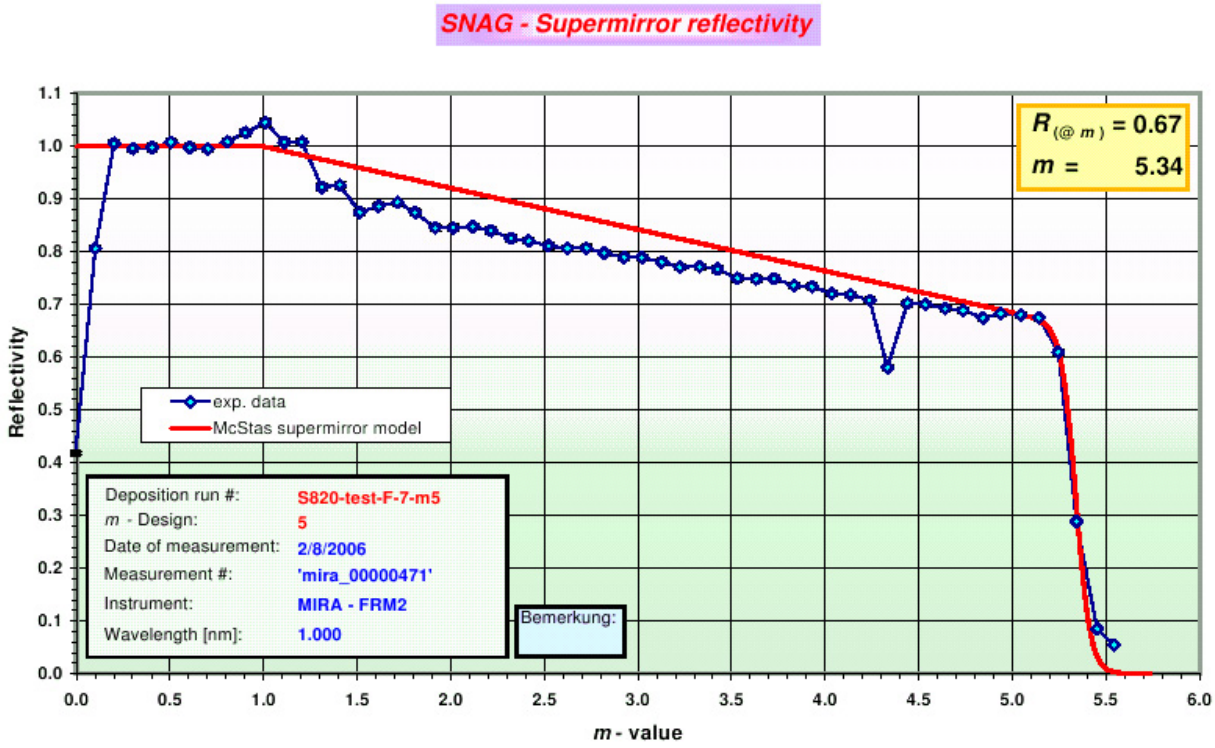

Figure 1: Neutron reflectivity profile of a m = 5 supermirror; m denotes the multiple of the regime of total external reflection of natural nickel. The dip around m ≈ 3.2 is caused by the lack of one layer.

This work was supported by the European Union within the Sixth Framework Program FP6 under contract no. 505925.

6.12 Polarizing supermirrors: Index matching in Fe/Si multilayer using reactive sputtering

Christian Schanzer [1, 2], **Murat Ay** [1], **Jochen Stahn** [1], **Sebastian Mühlbauer** [3], **R. Georgii** [3, 4]
[1] *Laboratory for Neutron Scattering ETHZ & PSI, CH-5232 Villigen PSI, Switzerland*
[2] *SwissNeutronics, CH-5313 Klingnau, Switzerland*
[3] *Physics Department E21, Technische Universität München, 85747 Garching, Germany*
[4] *ZWE FRM-II, Technische Universität München, 85747 Garching, Germany*

Polarizing supermirrors have established themselves as a dedicated method in neutron instrumentation to provide a polarized neutron beam and to analyze the polarization of the scattered beam. They are applied either in reflection or transmission mode. Latter provides the advantage that the beam trajectory is preserved when the polarizing/analyzing device is inserted. Fe and Si are dedicated materials for transmission mirrors due to low neutron absorption and since the scattering length density (SLD) of Si matches almost the SLD of Fe for one neutron spin state (b - p). Reactive sputtering enables to tune the SLD of Si in order to match precisely the b - p state of Fe. Moreover, the internal stress of the films can be manipulated in a way to create an anisotropic distribution, which results in a magnetic anisotropy via magneto-elastic coupling. Due to the magnetic anisotropy the polarizer/analyzer can be used in its 'remanent' state, i.e. at a rather low magnetic field (guide field) either with its magnetization parallel or even antiparallel to the applied field. This feature enables to switch the neutron polarization in the experiment by switching the magnetization of the mirror.

The goal of the present work is to reestablish the reactive sputtering process after the refurbishment of the sputtering plant at the Laboratory for Development and Methods, Paul Scherrer Institute, Switzerland. Moreover, it is aimed to improve the performance of Fe/Si polarizing supermirrors regarding their efficiency and magnetic anisotropy.

The reactive sputtering is tested using multilayers [Fe (7 nm) / Si (7 nm)]8 where Si is reactively sputtered varying the ratio of synthetic air from a flow rate of 7 to 30 sccm while the flow rate of the Ar sputter gas is fixed to 35 sccm. The samples are prepared on float glass. The SLD is supposed to vary dependent on the amount of nitrogen and oxygen which is incorporated during the growth of the Si layers. The SLD of the reactively sputtered Si layers is measured using polarized neutron reflectometry (PNR). These experiments were performed at the instrument MIRA, FRM-II, which uses a monochromatic ($\lambda = 0.96$ nm) and polarized (P $\approx$ 95 %) beam for PNR.

Fig. 1 shows spin dependent reflectivity profiles for selected flow rates of synthetic air. The Fe layers were magnetically saturated by an applied field of 1000 Oe. At low Qz the regime of total external reflection is not completely accomplished due to geometrical reasons while the foot print of the probing beam is larger then the length of the sample.

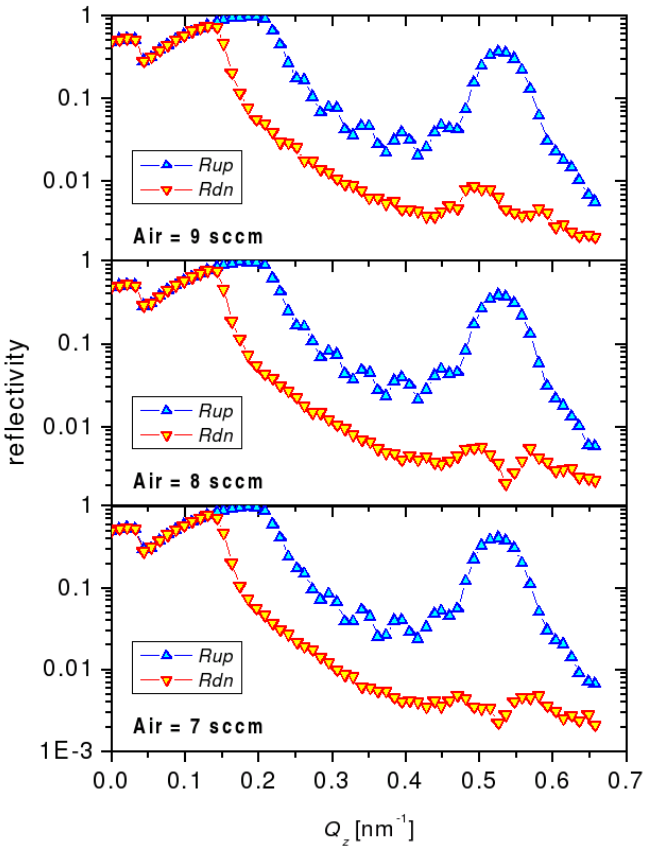

Figure 1: PNR of [Fe (7 nm) / Si (7 nm)]8 multilayers in an applied field of 1000 Oe. Si is reactively sputtered in Ar/synthetic air atmosphere with various flow rates of air. The data are corrected for the finite polarization of the incident beam.

The profile of the spin down reflectivity (Rdn) shows a dependence on the air flow rate around $Q_z \approx 0.5$ nm^{-1}. At a flow rate of 7 sccm almost no multilayer Bragg peak is observed indicating that the SLD of the Si layers is very close to the SLD of Fe for the b - p state. With increasing content of air a Bragg peak emerges at $Q_z \approx 0.5$ nm^{-1}. Hence the SLD of Si does not match well any more. Future experiments will focus to add information about less content of air and on the variation of the nitrogen/oxygen ratio in order to manipulate the magnetic properties while maintaining the index matching.

This work was supported by the European Union within the Sixth Framework Program FP6 under contract no. 505925.

6.13 Backface reflectometry - characterization of supermirrors

V. R. Shah* [1], **C. Schanzer** [2], **P. Böni** [1]

[1] *Physics Department E21, Technical University Munich, D-85747 Garching, Germany*
[2] *Laboratory for Neutron Scattering, ETHZ & PSI, CH-5232 Villigen PSI, Switzerland*

By employing back-face specular and off-specular x-ray reflectometry we have specifically investigated the interface properties of the initial layers of supermirror multilayers. This technique has been found especially useful in investigating thick multilayers e.g. neutron supermirrors with high values of the index m. The probed layers being the very bottom layers that dictate the growth of further layers in a multilayer, it becomes feasible to elucidate the properties of the initial layers, especially the initial interface roughness and its propagation, conformity, lateral correlations etc. We demonstrate that the observations from the x-ray analysis indicate already the neutron reflectivity performance of the supermirrors.

Ni/Ti supermirrors with $m \approx 2, 4$ and 5, produced by magnetron sputtering at LNS, PSI, Switzerland were analyzed. Two $m \approx 4$ supermirrors that showed good (case A) and poor (case B) neutron reflectivity were chosen for detailed analysis by means of specular and off-specular reflectometry. X-ray reflectometry on supermirrors in the conventional way (as deposited with thick layers on top) did not reveal any remarkable features compatible with neutron reflectivity. We investigated the initial layers by performing reflectometry at the bottom side of the multilayer. This was carried out after removing the multilayer film carefully from the original glass substrate and fixing it on another smooth substrate with bottom side up.

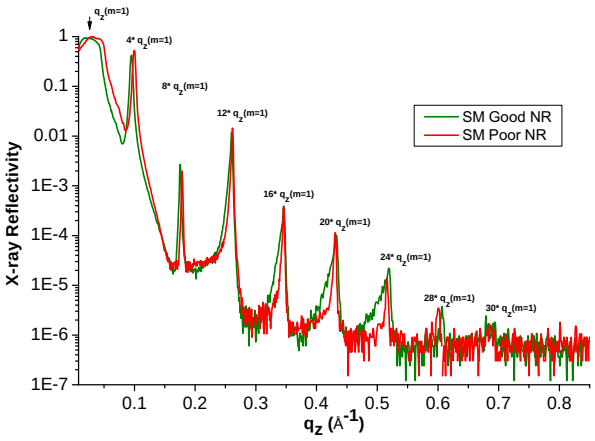

Figure 1: Specular reflectivity from the back face of the supermirrors having good and poor neutron reflectivity

Distinguishable features are observed in the backface specular and off-specular reflectivity revealing the signatures of the interface properties and lateral correlation. Fig.1 compares the specular x-ray reflectivity of cases A and B. Many higher order Bragg-reflections originating from depth-graded layers are seen as an indication of rather good interfaces. At lower order reflections reflectivity curves of both cases are rather alike however, at higher order reflections, a clear distinction is observed. The intensity distribution of the Bragg reflection is mostly localized around a particular q_z in case B, whereas it is rather distributed over a finite q_z range in case A. Moreover, the intensity diminishes only gradually towards lower q_z in case A. This is a clear indication that the vertical layer structure is very sharp and the interfaces clearly distinguish the gradation in bilayer thicknesses as designed in a supermirror. The loss of intensity along the specular ridge in case B does not imply enhanced interface roughness, but it is more likely to be caused by diffuse scattering. In order to verify this, we performed off-specular reflectometry on these bottom layers.

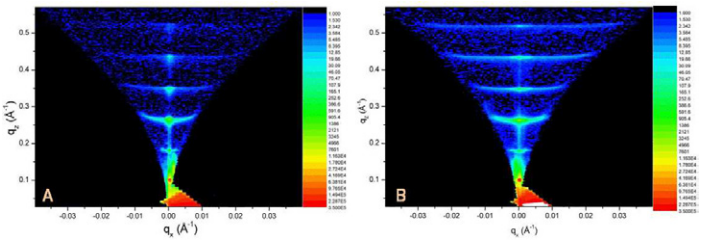

Figure 2: Off-specular reflectivity from the back face of the multilayers in cases A and B. Resonance diffuse scattering sheets are predominantly distinguishable in case B, presumably due to strong short-range lateral correlation of roughness.

Fig.2 shows a comparison of the reciprocal space maps of the off-specular intensity in both cases. Striking features along the resonance diffuse scattering sheets (RDS) in the q_x-direction [1] can be seen. The scattering is very pronounced and narrow and it spans over large q_x range in case B, whereas it is more confined around the specular Bragg spots and less spread along q_x in case A. These results indicate that the lateral correlation is very strong and of shorter length scale in case B compared to that of case A.

In conclusion, we demonstrate that the method of backface reflectometry using x-rays can be readily applied for characterizing neutron supermirrors and can predict the neutron reflectivity qualitatively. This characterization technique can be extended to other types of multilayers as well, where a post-synthesis analysis becomes necessary in troubleshooting the parameters that might have influenced the growth and interface quality.

This work was supported by the European Union within the Sixth Framework Program FP6 under contract no. 505925.

References

[1] In *High-Resolution X-ray Scattering from Thin Films to Lateral Nanostructures, Second Edition*, pages 235–272. Springer, New York, 2004.

*Present address: LENS, Indiana University Cyclotron Facility, Bloomington, IN-47408, Indiana, USA.

7

Activities 2006

7.1 Lectures, Courses and Seminars

P. Böni	Lecture "Experimentalphysik für Elektrotechniker" (SS 06)
	Exercises "Experimentalphysik für Elektrotechniker" (SS 06)
	Lecture "Festkörperphysik I" (WS 06/07)
	Tutorial "Festkörperphysik I" (WS 06/07)
	Exercises "Festkörperphysik I" (WS 06/07)
	Seminar "Neutronen in Forschung und Industrie" (WS 05/06, SS 06, WS 06/07), together with Prof. W. Petry, Prof. K. Schreckenbach and Dr. W. Häußler
	Seminar "Experimentelle Methoden der Festkörperphysik" (WS 05/06, SS 06, WS 06/07), together with Prof. C. Pfleiderer and Dr. C. Hugenschmidt
R. Georgii	Practical course "Fortgeschrittenenpraktikum für Physiker" (WS 05/06, SS 06, WS 06/07) (at FRM-II)
W. Häußler	Seminar "Neutronen in Forschung und Industrie" (WS 05/06, SS 06, WS 06/07), together with Prof. P. Böni, Prof. W. Petry and Prof. K. Schreckenbach
C. Hugenschmidt	Seminar "Experimentelle Methoden der Festköperphysik" (WS 05/06, SS 06, WS 06/07), together with Prof. C. Pfleiderer and Prof. P. Böni
M. Janoschek	Tutorial "Experimentalphysik für Elektrotechniker" (SS 06)
T. Keller	Practical course "Elektronikpraktikum" (WS 05/06, SS 06, WS 06/07)
S. Legl	Practical course "Anfängerpraktikum" (WS 05/06)
	Tutorial "Experimentalphysik für Elektrotechniker" (SS 06)
	Tutorial "Festkörperphysik I" (WS 06/07)
B. Löwe	Practical course "F-Praktikum Positronen-Annihilation" (WS 06/07)
K. Lorenz	Practical course "Elektronikpraktikum" (WS 05/06, SS 06, WS 06/07)
J. Mayer	Tutorial "Experimentalphysik I" (WS 06/07)
C. Morkel	Lecture "Physik mit Neutronen I" (WS 06/07)
M. Mühlbauer	Practical course "Elektronikpraktikum" (WS 05/06, SS 06, WS 06/07)
S. Mühlbauer	Tutorial "Experimentalphysik für Elektrotechniker" (SS 06)
	Tutorial "Festkörperphysik I" (WS 06/07)
A. Neubauer	Tutorial "Experimentalphysik I" (WS 06/07)
P. Niklowitz	Tutorial "Experimentalphysik 1 für Geodäsie und Geoinformation" (WS 05/06)
	Tutorial "Experimentalphysik 2 für Geodäsie und Geoinformation" (SS 06)
	Tutorial "Festkörperphysik I" (WS 06/07)
C. Pfleiderer	Seminar "Neue Supraleiter und Suprafluide" (SS 06), together with PD Dr. R. Hackl, PD Dr. D. Einzel and Prof. Dr. W. Zwerger
	Seminar "Experimentelle Methoden der Festköperphysik" (WS 05/06, SS 06, WS 06/07), together with Prof. P. Böni and Dr. C. Hugenschmidt
	Lecture "Experimentalphysik 1 für Geodäsie und Geoinformation" (WS 05/06)
	Tutorial "Experimentalphysik 1 für Geodäsie und Geoinformation" (WS 05/06)
	Lecture "Experimentalphysik 2 für Geodäsie und Geoinformation" (SS 06)
	Tutorial "Experimentalphysik 2 für Geodäsie und Geoinformation" (SS 06)

	Lecture "Experimentalphysik I" (WS 06/07)
	Tutorial "Experimentalphysik I" (WS 06/07)
P. Pikart	Practical course "F-Praktikum Positronen-Annihilation" (WS 06/07)
C. Piochacz	Tutorial "Experimentalphysik für Elektrotechniker" (SS 06)
	Tutorial "Festkörperphysik I" (WS 06/07)
	Practical course "F-Praktikum Positronen-Annihilation (WS 05/06, SS 06)"
R. Ritz	Tutorial "Experimentalphysik I" (WS 06/07)
M. Schulz	Practical course "Elektronikpraktikum" (WS 05/06, SS 06, WS 06/07)
B. Schillinger	Practical course "Elektronikpraktikum" (WS 05/06, SS 06, WS 06/07)
K. Schreckenbach	Lecture "Reaktorphysik und neue Methoden der Kerntechnik" (WS 06/07)
	Seminar "Neutronen in Industrie and Forschung" (WS 05/06, SS 06, WS 06/07), together with Prof. P. Böni, Prof. W. Petry and Dr. W. Häußler
	Practical course "Fortgeschrittenenpraktikum für Physiker" (WS 05/06, SS 06, WS 06/07)(at FRM-II)
M. Stadlbauer	Tutorial "Experimentalphysik für Elektrotechniker" (SS 06)
	Tutorial "Festkörperphysik I" (WS 06/07)
	Practical course "F-Praktikum Positronen-Annihilation" (WS 05/06, SS 06)

7.2 Invited Speakers at E21 in 2006

Date	Speaker	Title	Seminar
Jan 01	Dr. B. Schillinger, FRM-II	Curious new measurements at the neutron radiography and tomography facility ANTARES at FRM-II	Seminar 'Neutronen in Forschung und Industrie'
Feb 09	Dr. May Chiao, Nature Physics	How to publish in Nature Physics	Festkörperkolloquium
March 06	Dr. Benedikt Binz, University of California, USA	Theory of the helical spin crystal: a candidate for the partially ordered state of MnSi	E21 Seminar
April 27	Prof. Dr. Warren Pickett, KITP & UC Davis	Recent developments in superconductors, and what might have been	Festkörperkolloquium
May 14	Prof. Dr. Yasutomo J. Uemura, Columbia University, USA	Phase separation in crossover from itinerant ferromagnet to correlated paramagnet: MuSR studies in MnSi and $(Sr,Ca)RuO_3$	E21 Seminar
May 22	Dr. D. Reznik, Forschungszentrum Karlsruhe	Giant Phonon Anomaly Reflecting Strongly Correlated Nature of the Cuprates	Seminar 'Neutronen in Forschung und Industrie'
May 29	Prof. Dr. J.A. Mydosh, Universität zu Köln	Strongly correlated electron systems: hidden order and novel phases	Münchner Physik Kolloquium
June 19	Dr. O. Stockert, MPI for Chemical Physics of Solids, Dresden	Magnetism and superconductivity in heavy-fermion systems close to quantum criticality	Seminar 'Neutronen in Forschung und Industrie'
June 22	Dr. Christoph Bergemann, Cavendish Laboratory, University of Cambridge, UK	Electrons on the magnetic quantum roundabout – measuring Fermi surfaces and band renormalization in correlated materials	Festkörperkolloquium
July 10	Dr. N. Bernhoeft, Grenoble	Possible extension of neutron cross-section to Multiple Order Parameters	Seminar 'Neutronen in Forschung und Industrie'
Dec 4	Dr. P.S. Häfliger, Physik-Institut der Universität Zürich	Aspects of Unconventional Superconductivity	Seminar 'Neutronen in Forschung und Industrie'
Dec 14	PD Dr. Joachim Hemberger, Universtität Augsburg	Multiferroelectrics	Festkörperkolloquium
Dec 18	S. Mühlbauer, TU München	Flußliniengitter in Supraleitern - Untersuchungen mit Neutronenstreuung	Seminar 'Neutronen in Forschung und Industrie'
Dec 21	Dr. Sarah Dunsiger, Mc Master University, Canada	Quantum and frustrated antiferromagnets: disordered ground state systems	Festkörperkolloquium

7.3 Workshops 2006

Date	Title	Location
Sep 28/29	DGKK Arbeitskreis intermetallische Verbindungen mit Spin und Ladungskorrelation und workpackage meeting of the EU network Complex Metallic Alloys	Technical University Munich, Garching

7.4 Publications 2006

[1] K. H. Andersen, R. Cubitt, H. Humblot, D. Jullien, A. Petoukhov, F. Tasset, C. Schanzer, V. R. Shah, and A.R. Wildes. The ^{3}He polarizing filter on the neutron reflectometer D17. *Physica B*, 385-386:1134–1137, 2006.

[2] A. Aprahamian, X. Wu, S.R. Lesher, D.D. Warner, W. Gelletly, H.G. Börner, F. Hoyler, K. Schreckenbach, R.F. Casten, Z.R. Shi, D. Kusnezov, M. Ibrahim, A.O. Macciavelli, M.A. Brinkman, and J.A. Becker. Complete spectroscopy of ^{162}Dy nucleus. *Nuclear Physics A*, 764:42, 2006.

[3] A. J. Banchio, J. Gapinski, A. Patkowski, W. Häußler, A. Fluerasu, S. Sacanna, P. Holmqvist, G. Meier, M. P. Lettinga, and G. Nägele. Many-body hydrodynamic interactions in charge stabilized suspensions. *Phys. Rev. Lett.*, 96:138303, 2006.

[4] E. Blackburn, A. Hiess, N. Bernhoeft, M.C. Rheinstädter, W. Häußler, and G.H. Lander. Fermi surface topology and the superconducting gap in UPd_2Al_3: A neutron spin-echo study. *Phys. Rev. Lett.*, 97:057002, 2006.

[5] J. Bœuf, C. Pfleiderer, and A. Faißt. Low Temperature Properties of CuMnSb. *Phys. Rev. B*, 74:024428, 2006.

[6] P. Böni. Chiralität von Solitonen. *TUM-Mitteilungen*, 3:66–67, 2006.

[7] F. Demmel, A. Diepold, H. Aschauer, and C. Morkel. Temperature dependence of the de Gennes narrowing in liquid rubidium. *Pys. Rev. B*, 73:104207, 2006.

[8] F. Demmel, P. Fouquet, W. Häußler, and C. Morkel. De Gennes slowing in a liquid metal revisited: A neutron spin-echo study. *Phys. Rev. E*, 73:032202, 2006.

[9] F. Demmel, D. Pasqualini, and C. Morkel. Inelastic collective dynamics of liquid rubidium with increasing temperature by neutron scattering studies. *Phys. Rev. B*, 74:184207, 2006.

[10] G. Dosseh, C. Le Quellec, N. Brodie-Lindner, C. Alba-Simionesco, W. Häußler, and P. Levitz. Fluid-wall interaction effects on the dynamical properties of confined orthoterpheny. *J. Non-Cryst. Solids*, 352:4964–4968, 2006.

[11] G. Ehlers, J.S. Gardner, C.H. Booth, M. Daniel, K.C. Kam, A.K. Cheetham, D. Antonio, H.E. Brooks, A.L. Cornelius, S.T. Bramwell, J. Lago, W. Häußler, and N. Rosov. Dynamics of diluted Ho spin ice $Ho_{2-x}Y_xTi_2O_7$ studied by neutron spin echo spectroscopy and ac susceptibility. *Phys. Rev. B*, 73:174429, 2006.

[12] Yasuo Endoh and Peter Böni. Magnetic excitations in metallic ferro- and antiferromagnets. *J. Phys. Soc. Jpn.*, 75:111002–(1–11), 2006.

[13] B. Fåk, C. Rüegg, P. G. Niklowitz, D. F. McMorrow, J. Flouquet, P. C. Canfield, S. L. Bud'ko, Y. Jannsen, and K. Habicht. Magnetic phase diagram of heavy-fermion YbAgGe. *Physica B*, 378-380:669, 2006.

[14] P. Fischer, V. Pomjakushin, D Sheptyakov, L. Keller, M. Janoschek, B. Roessli, J. Schefer, G. Petrakovskii, L. Bezmaternikh, V. Temerov, and D. Velikanov. Simultaneous antiferromagnetic Fe^{3+} and Nd^{3+} ordering in $NdFe_3(_{11}BO_3)_4$. *J. Phys.: Condens. Matter*, 34:7975–7989, 2006.

[15] K. Grube, S. Drobnik, C. Pfleiderer, H. v. Löhneysen, E. D. Bauer, and M. B. Maple. Specific-Heat and AC-Susceptibility Studies of the Superconducting Phase Diagram of $PrOs_4Sb_{12}$. *Phys. Rev. B*, 73:104503, 2006.

[16] S. Gvasaliya, L. Keller, M. Kenzelmann, B. Roessli, J. Schefer, K. Conder, E. Pomjakushina, M. Janoschek, B. Harris, S. Jonas, C. Broholm, O. Vajk, Jeff W. Lynn, S. B. Kim, C.L. Zhang, and S.-W. Cheong. Low temperature magnetoferroelectrics. *PSI Scientific Report*, 1:42–43, 2005.

[17] C. Hugenschmidt and S. Legl. Novel time-of-flight spectrometer for the analysis of positron annihilation induced Auger electrons. *Rev. Sci. Instr.*, 77:103904, 2006.

[18] C. Hugenschmidt, K. Schreckenbach, M. Stadlbauer, and B. Strasser. First positron experiments at NEPOMUC. *Appl. Surf. Sci.*, 252:3098–3105, 2006.

[19] G. Knebel, R. Boursier, E. Hassinger, G. Lapertot, P. G. Niklowitz, A. Pourret, B. Salce, J. P. Sanchez, I. Sheikin, P. Bonville, H. Harima, and J. Flouquet. Localization of 4f state in $YbRh_2Si_2$ under magnetic field and high pressure: comparison with $CeRh_2Si_2$. *J.Phys.Soc.Japan*, 75:114709, 2006.

[20] G. Knebel, E. Hassinger, G. Lapertot, P. G. Niklowitz, J. P. Sanchez, and J. Flouquet. On the high-pressure phase diagram of $YbRh_2Si_2$. *Physica B*, 378-380:68, 2006.

[21] M. Senthil Kumar, P. Böni, and M. Horisberger. Relationship between neutron reflectivity, electrical resistance, stress, and embrittlement in reactively sputtered Ni/Ti multilayers and supermirrors. *Appl. Phys. Lett.*, 385-386:1265–1267, 2006.

[22] D. Lamago, R. Georgii, C. Pfleiderer, and P. Böni. Magnetic-Field Induced Instability in the A-phase of MnSi: Bulk and SANS Measurements. *Physica B*, 385-386:385, 2006.

[23] H. Li, B. Schillinger, E. Calzada, L. Yinong, and M. Mühlbauer. An adaptive alogorithm for gamma spots removal in CCD-based neutron radiography and tomography. *Nucl. Inst. and Meth. A*, 564:405–413, 2006.

[24] P. Maier-Komor, I. Altarev, A. Bergmaier, P. Böni, G. Dollinger, R. Krücken, S. Paul, and W. Schott. Design and advanced preparation of multilayer converters for ultracold-neutron detectors. *Nucl. Instr. Meth. A*, 561:45–51, 2006.

[25] S. Mühlbauer, P. Böni, U. Filges, C. Schanzer, M. Stadlbauer, and J. Stahn. Performance of an elliptically tapered neutron guide. *Physica B*, 385-386:1247, 2006.

[26] P. G. Niklowitz, G. Knebel, J. Flouquet, S. L. Bud'ko, and P. C. Canfield. Field-induced non-fermi-liquid resistivity of stoichiometric YbAgGe single crystals. *Phys.Rev.B*, 73:125101, 2006.

[27] P. G. Niklowitz, G. Knebel, J. Flouquet, S. L. Bud'ko, and P. C. Canfield. Magnetic properties near the non-fermi-liquid regime in the antiferromagnetic heavy-fermion compound YbAgGe. *Physica B*, 378-380:161, 2006.

[28] P. G. Niklowitz and C. Paulsen. From antiferromagnetic order to a field-polarised state in the heavy-fermion compound YbAgGe. *Phys.Lett.A*, 360:376, 2006.

[29] J. Padiyath, J. Stahn, M. Horisberger, M. Ay, and P. Böni. Polarizing neutron monochromator with reduced higher-order. *Appl. Phys. Lett.*, 89:253111, 2006.

[30] J. Padiyath, J. Stahn, M. Horisberger, and P. Böni. Multilayers with tailored blurred interfaces. *Appl. Phys. Lett.*, 89:113123, 2006.

[31] C. Pfleiderer, J. A. Mydosh, and M. Vojta. Pressure Dependence of the Magnetization of URu_2Si_2. *Phys. Rev. B*, 74:104412, 2006. cond-mat/06006641.

[32] W. C. Pilgrim and C. Morkel. State dependent particle dynamics in liquid alkali metals. *J. Phys.: Condens. Matter*, 18:585–633, 2006.

[33] M. C. Rheinstädter, W. Häußler, and T. Salditt. Dispersion relation of lipid membrane shape fluctuations by neutron spin-echo spectrometry. *Phys. Rev. Lett.*, 97:048103, 2006.

[34] M. C. Rheinstädter, T. Seydel, and W. Häußler et al. Exploring the collective dynamics of lipid membranes with inelastic neutron scattering. *Journ. Vac. Sc. and Techn. A*, 24:1191–1196, 2006.

[35] M. C. Rheinstädter, Tilo Seydel, Wolfgang Häußler, and Tim Salditt. The 'neutron window' of collective excitations in lipid membranes. *Physica B*, 385-386:722–724, 2006.

[36] U. K. Rößler, A. N. Bogdanov, and C. Pfleiderer. Spontaneous Skyrmion Ground States of Magnetic Metals. *Nature*, 442:797, 2006. condmat/0603103 & 0603104.

[37] M. Uhlarz H. v. Löhneysen D. Souptel W. Löser G. Behr S. Drotziger, C. Pfleiderer. Supression of Ferromagnetism in $CeSi_{1.81}$ under Temperature and Pressure. *Phys. Rev. B*, 73:214413, 2006. condmat/0604470.

[38] B. Schillinger, J. Brunner, and E. Calzada. A study of oil lubrication in a rotating engine ising stroboscopic neutron imaging. *Physica B: Condensed Matter*, 385-386:921–923, 2006.

[39] K. Schreckenbach. Nuclear and particle physics at the new neutron source FRM – II in Garching, Germany. *Nuclear Physics News*, 15:5, 2005.

[40] V. R. Shah, C. Schanzer, P. Böni, , and H. B. Braun. Interface and magnetic characterization of FeCoV/NiO/FeCoV trilayers. *The Physics of Metals and Metallography*, 101:S73–S77, 2006.

[41] V. R. Shah, C. Schanzer, P. Böni, and H. B. Braun. Interface and magnetic characterization of FM/AF/FM multilayers. *Proc. of the NATO Advanced Research Workshop NATO ARW PST.NUKR.*, ARW980688:179–194, 2006.

[42] M. Stadlbauer, C. Hugenschmidt, B. Strasser, and K. Schreckenbach. Spatially resolved investigation of thermally treated brass with a coincident Doppler-spectrometer. *Appl. Surf. Sci.*, 252:3269–3272, 2006.

[43] H. v. Löhneysen, H. Bartolf, S. Drotziger, C. Pfleiderer, O. Stockert, D. Souptel, W. Löser, and G. Behr. Rare-Earth Intermetallic Compounds at a Magnetic Instability. *J. Alloys and Compounds*, 408:9, 2006.

[44] H. v. Löhneysen, H. Bartolf, C. Pfleiderer, F. Obermair, M. Vojta, and P. Wölfle. Magnetotransport in $CeCu_{6-x}Au_x$ under Temperature and Pressure. *Physica B*, 378-380:44, 2006.

[45] N. Volkov, G. Petrakovskii, P. Böni, E. Clementyev, K. Sablina K. Patrin, E. Eremin, and V. Vasiliev. Magnetic and transport properties of $(La_{0.4}Eu_{0.6})_{0.7}Pb_{0.3}MnO_3$ single crystal: The key role of intrinsic inhomogeneity. *J. Magn. Magn. Mater.*, 300:e179–e182, 2006.

[46] N. Volkov, G. Petrakovskii, K. Patrin, K. Sablina, E. Eremin, V. Vasiliev, A. Vasilieva, M. Molokeev, P. Böni, and E. Clementyev. Intrinsic inhomogeneity in a $(La_{0.4}Eu_{0.6})_{0.7}Pb_{0.3}MnO_3$ single crystal: Magnetization, transport, and electron magnetic resonance studies. *Phys. Rev. B*, 73:104401–(1–10), 2006.

[47] F. Weber, A. Cosceev, S. Drobnik, A. Faißt, K. Grube, C. Pfleiderer A. Nateprov, M. Uhlarz, and H. v. Löhneysen. Low-Temperature Properties and Magnetic Order of $EuZn_2Sb_2$. *Phys. Rev. B*, 73:014427, 2006.

[48] K. Zeitelhack, C. Schanzer, A. Kastenmüller, A. Röhrmoser, C. Daniel, J. Franke, E. Gutsmiedl, V. Kudryashov, D. Maierand D. Päthe, W. Petry, T. Schöffel, K. Schreckenbach, A. Urban, and U. Wildgruber. Measurement of neutron flux and beam divergence at the cold neutron guide system of the new Munich research reactor FRM – II. *Nuc. Instr. and Methods A*, 560:42, 2006.

7.5 Conference, Workshop and Seminar Contributions 2006

[1] P. Böni. Anwendung von Polarisierten Neutronen in der Materialforschung. Seminar Talk, July 27 2006. Ludwig Maximilian Universität, München, Germany.

[2] P. Böni. Exploring Unconventional Materials with Novel Techniques. Talk. *Workshop 'Experimental Physics of Emergent Materials'*, January 15-17 2006. Max-Planck-Institut für Chemische Physik, Dresden, Germany.

[3] P. Böni. Incommensurate Magnets: Unraveling their intriguing properties. Talk. *40 Jahre Neutronenstreuung am Forschungszentrum Karlsruhe*, March 24 2006. Forschungszentrum Karlsruhe, Germany.

[4] P. Böni. JRA3: European Initiative for Neutron Optics. Invited Talk. *Polarized Neutrons in Condensed Matter Investigations PNCMI 2006*, September 28 2006. Berlin, Germany.

[5] P. Böni. Magnetic Correlations in Incommensurate MnSi and Cr: Investigations with Polarized Neutrons. Talk. *Joint Swiss-Russian Workshop on Quantum Magnetism and Polarized Neutrons*, March 1-4 2006. Paul Scherrer Institute, Villigen, Switzerland.

[6] P. Böni. Magnetic Excitations in Incommensurate Materials. Talk. *Physics Colloquium WS 05/06*, February 8 2006. ETH Zurich, Switzerland.

[7] P. Böni. Magnetic Excitations in Incommensurate Materials. Talk. *SFB Kolloqium*, July 18 2006. Universität Augsburg, Germany.

[8] P. Böni. Neutron Optics and Polarizing Elements. Lecture. *School on Polarized Neutrons*, September 19-22 2006. Hahn-Meitner-Institute, Berlin, Germany.

[9] P. Böni. Recent Advancements in Neutron Optics. Talk. *Seminar on Neutron Instrumentation*, April 6 2006. Laboratoire Léon Brillouin, Saclay, France.

[10] T. Brunner. Das Positron – Antimaterie als Mikrosonde. Talk. *DPG-Tagung*, March 2006. Dresden, Germany.

[11] T. Brunner. Temperature dependent moderation efficiency and Ps formation. Talk. *ICPA 14*, July 2006. Hamilton, Canada.

[12] R. Georgii. MIRA – a flexible instrument for long wavelength neutrons. Talk. *DPG-Tagung*, March 2006. Dresden, Germany.

[13] R. Georgii. MIRA – a flexible instrument for polarised VCN. Talk. *Polarised Neutrons in Condensed Matter Investigations (PNCMI)* , 2006. Berlin, Germany.

[14] R. Georgii. MIRA – the very cold beam line at FRM-II. Talk. *PSI workshop on very cold neutrons*, February 2 2006. Switzerland.

[15] W. Häußler. Development of new NRSE coils for large tilt angles and large beam areas. Talk. *NMI-FP6 meeting*, May 2006. Vienna, Austria.

[16] W. Häußler. Reseda – the new Resonance Spin Echo Spectrometer using cold neutrons at the FRM-II. Talk. *Polarized Neutrons in Condensed Matter Investigations*, September 2006. Berlin, Germany.

[17] C. Hugenschmidt. Die intensive Positronenquelle NEPOMUC und erste Experimente. Talk. *Seminar, Lehrstuhl für Kernphysik E12*, July 2006. Technische Universität München.

[18] C. Hugenschmidt. The Positron Beam Facility NEPOMUC and Positron Experiments at FRM-II. Invited Talk. *DPG-Tagung*, March 2006. Dresden, Germany.

[19] C. Hugenschmidt. Positron Experiments at NEPOMUC. Invited Talk. *Bothe-Kolloquium, Max-Planck-Institut für Kernphysik* , July 2006. Heidelberg, Germany.

[20] C. Hugenschmidt. Positron Experiments at the New Positron Beam Facility NEPOMUC. Invited Talk. *ICPA 14*, July 2006. Hamilton, Canada.

[21] C. Hugenschmidt. Untersuchung von Nanomaterialien mit Positronen. Invited Talk. *30. Edgar-Lüscher-Physikseminar*, April 2006. Zwiesel, Germany.

[22] M. Janoschek. Reduction of the ordered magnetic moment in $YMnO_3$ with hydrostatic pressure. Poster. *Hercules Course*, 2006. Grenoble, France.

[23] M. Janoschek. Reduction of the ordered magnetic moment in $YMnO_3$. Invited Talk. *8th SINQ User Meeting*, May 2006.

[24] M. Janoschek. Spherical Neutron Polarimetry Analysis with FullProf. Poster. *Annual Meeting of the Swiss Society for Crystallography*, October 2006.

[25] D. Lamago. Bulk properties and neutron diffraction of the magnetic phase diagram of MnSi. Talk. *DPG-Tagung*, March 2006. Dresden, Germany.

[26] S. Legl. Magnetization and Resistivity of Pr_5Si_3. Poster. *Prague Colloquium on f-Electron Systems & General Workshop of COST Action P16*, September 11 2006. University of Prague.

[27] S. Legl. A novel time of flight spectrometer for PAES. Talk. *ICPA 14*, July 2006. Hamilton, Canada.

[28] S. Legl. Time of flight spectrometer for the analysis of positron annihilation induced Auger electrons. Poster. *DPG-Tagung*, March 2006. Dresden, Germany.

[29] K. Lorenz. Viscosity measurements with dynamic neutron radiography. Poster. *Conference JCNS-Symposium and EU User Meeting* , February 16 2006. Jülich, Germany.

[30] J. Mayer. PAES: Positron annihilation induced Auger electron spectroscopy. Poster. *DPG-Tagung*, March 2006. Dresden, Germany.

[31] J. Mayer. Positron annihilation induced Auger electron spectroscopy of Cu and Si. Talk. *ICPA 14*, July 2006. Hamilton, Canada.

[32] M. Mühlbauer. Workshop. *Treffen von Europäischen Neutronenradiographiestationen* , March 17 2006. HMI, Berlin, Germany.

[33] M. Mühlbauer. Investgation of an Early Medieval Sword by Neutron Tomography. Talk. *Conference JCNS-Symposium and EU User Meeting* , February 16 2006. Jülich, Germany.

[34] M. Mühlbauer. Testing a compact tomography setup at Aerotest Radiographyand Research Reaktor, San Ramon, California. Talk. 8th *World Conference On Neutron Radiograpy (WCNR-8)* , October 16 2006. Gaithersburg, ML, USA.

[35] M. Mühlbauer. Vicosity measurements with dynamic neutron radiography. Poster. *Conference JCNS-Symposium and EU User Meeting* , February 16 2006. Jülich, Germany.

[36] M. Mühlbauer. Vorstellung des FRM-II/ANTARES. Talk. *Meeting FVV Diskussionskreissitzung Vorhaben* $Spritzlochgeometrie$*, Lehrstuhl für Verbrennungskraftmaschinen (LKV)* , September 26 2006. Munich, Germany.

[37] S. Mühlbauer. Polarised Neutron Scattering of the Flux Line Lattice of Superconducting Niobium. Poster. *DPG-Tagung*, March 2006. Dresden, Germany.

[38] S. Mühlbauer. Supraleitung in Schwer-Fermion Systemen. Talk. *Seminar Supraleitung und Suprafluidität*, July 3 2006. Technische Universität München.

[39] S. Mühlbauer. Vortex lattices in superconductors- studied with smaal angle neutron scattering. Talk. *Seminar Neutrons in science and industry*, December 18 2006. Technische Universität München.

[40] A. Neubauer. Hall-Effekt and Magnetoresistance in $CeSi_2$ and MnSi. Poster. *Prague Colloquium on f-Electron Systems & General Workshop of COST Action P16*, March 2006. Dresden, Germany.

[41] A. Neubauer. Hall-Effekt and Magnetoresistance in MnSi. Poster. *DPG-Tagung*, March 2006. Dresden, Germany.

[42] P. G. Niklowitz. The border of antiferromagnetism in the metallic state. Colloquium Talk.*Condensed Matter Seminar*, October 20 2006. Royal Holloway College, Egham, UK.

[43] P. G. Niklowitz. Field-induced non-fermi-liquid resistivity and magnetic properties of the heavy-fermion compound YbAgGe. Poster. *ICM conference*, August 21 2006. Kyoto, Japan.

[44] P. G. Niklowitz. From antiferromagnetic order to a field-polarised state in the heavy-fermion compound YbAgGe. Talk. *DPG Frühjahrstagung*, March 27 2006. Dresden, Germany.

[45] C. Pfleiderer. Crossover or stable phase? New experiments in MnSi. Talk. *Workshop on Quantum Criticality*, August 11 2006. Lorentz Center, University of Leiden.

[46] C. Pfleiderer. The department of physics at TUM. Talk. *Evaluation at Excellence Initiative of the German Federal Government*, June 26 2006. Technische Universität München.

[47] C. Pfleiderer. Neutron spin resonance experiments in MnSi under pressure. Workshop. *Prague Colloquium on f-Electron Systems & General Workshop of COST Action P16*, September 11 2006. University of Prague.

[48] C. Pfleiderer. Quantenphasenübergänge: Nur Buzz-Word Bingo? Tutorial Lecture. *Elitestudiengang University of Regensburg*, July 21 2006. Tagungszentrum Veillbronn.

[49] C. Pfleiderer. Quantum Order in Chiral Magnets. Colloquium Talk. *Gemeinsames Physikalisch-Chemisches Kolloquium*, December 20 2006. Max Planck Institut für Chemische Physik fester Stoffe.

[50] C. Pfleiderer. Weird, quantum or what? the case of MnSi. Talk. *Workshop on quantum complexities in condensed matter*, July 5 2006. University of Cambridge, UK.

[51] C. Piochacz. Implementation of the Munich SPM at NEPOMUC. Poster. *ICPA 14*, July 2006. Hamilton, Canada.

[52] C. Piochacz. Implementation of the Munich SPM at NEPOMUC. Talk. *DPG-Tagung*, March 2006. Dresden, Germany.

[53] C. Schanzer, P. Böni, and H.-U. Aebersold. Irradiation tests at SINQ. Talk. *Workshop on Neutron Guides*, April 26/27 2006. Institute Laue-Langevin, Grenoble, France.

[54] B. Schillinger. Workshop. *Treffen von Europäischen Neutronenradiographiestationen* , March 17 2006. HMI, Berlin, Germany.

[55] B. Schillinger. Workshop. *ESS Scandinavia Workshop on instrumentation for a long pulse target station*, April 20/21 2006. Lund, Sweden.

[56] B. Schillinger. Continuous neutron radioscopy with 1000 fps and 10 microsecond time resolution. Talk. *Conference 8th World Conference On Neutron Radiography (WCNR-8), NIST*, October 16-19 2006. Gaithersburg ML, USA.

[57] B. Schillinger. Continuous neutron radioscopy with 1000 fps and 10 microsecond time resolution. Talk. *Conference Imaging and Neutrons 2006, Spallation Neutron Source (SNS), Oak Ridge National Laboratories*, October 23-25 2006. Oak Ridge TS, USA.

[58] B. Schillinger. Detection of texture alteration in steel and al parts using small angle scattering in neutron radiography and computed tomography. Talk. *Conference 8th World Conference On Neutron Radiography (WCNR-8), NIST*, October 16-19 2006. Gaithersburg ML, USA.

[59] B. Schillinger. First neutron phase contrast tomography at the ANTARES facility. Talk. *Conference 8th World Conference On Neutron Radiography (WCNR-8), NIST*, October 16-19 2006. Gaithersburg ML, USA.

[60] B. Schillinger. Neutron Radiography and Tomography – a Strategy for Neutrograph. Talk. *ILL Millenium Symposium*, April 27-29 2006. Grenoble, France.

[61] B. Schillinger. Neutron radiography with multiple energy range filters at the ANTARES facility. Talk. *Conference 8th World Conference On Neutron Radiography (WCNR-8), NIST*, October 16-19 2006. Gaithersburg ML, USA.

[62] B. Schillinger. Observation of the filling level of the cold source by pinhole neutron radiography. Talk. *Conference 8th World Conference On Neutron Radiography (WCNR-8), NIST*, October 16-19 2006. Gaithersburg ML, USA.

[63] K. Schreckenbach. Der Tschernobyl Unfall vor 20 Jahren und die Frage nach inhärenten Sicherheit von Kernreaktoren. Talk. *MLL Kolloquium*, October 19 2006. Technische Universität München.

[64] K. Schreckenbach. Experiments on the Beat Decay of the Free Neutron. Talk. *SFB 375 Workshop*, October 9 2006. Gaissach, Germany.

[65] K. Schreckenbach. Moderation von Positronen in Gasen. Talk. *Seminar, Sektion Physik LMU*, June 26 2006. Garching, Germany.

[66] K. Schreckenbach. Technik und Forschung am FRM-II. Talk. *Workshop FANP Qualitätssicherung*, January 1 2006. Kassel, Germany.

[67] K. Schreckenbach. The Tschernobyl Accident 20 Years ago and the Quest for Inherently Save Nuclear Reactors. Talk. *Doktoranden Wokshop der Max Planck Institute*, July 18 2006. Ringberg, Germany.

[68] M. Schulz. Workshop. *Treffen von Europäischen Neutronenradiographiestationen* , March 17 2006. HMI, Berlin, Germany.

[69] M. Schulz. Neutron Imaging Methods at FRM-II. Talk. *Conference SNI* , October 4 2006. Hamburg, Germany.

[70] M. Stadlbauer. Element specific defect investigation on Mg-alloys by ion implantation with CDBS. Talk. *ICPA 14*, July 2006. Hamilton, Canada.

[71] M. Stadlbauer. Element specific defect investigation on Mg-alloys with Coincident Doppler Broadening Spectroscopy. Talk. *DPG-Tagung*, March 2006. Dresden, Germany.

7.6 Committee Memberships

P. Böni
- Instrument Subcommittee, Institut Laue-Langevin, Grenoble, France
- Reviewer of experimental proposals, GKSS, Geesthacht, Germany
- Projektbegleitender Beirat FRM-II, Garching
- Instrumentierungsausschuss FRM-II, Garching
- TUM-Beirat für den FRM-II, Garching
- Coordinator of Work Package on Neutron Optics, Joint Research Project JRA3: NMI3 FP6
- Conference on Polarized Neutrons in Condensed Matter Research PNCMI 2006, Berlin, Scientific Advisory Committee
- 8th International Conference on the Physics of X-Ray Multilayer Structures PXRMS'06, member of program committee
- Co-chairman of the European Workshop on Neutron Optics NOP'07, Villigen PSI, Switzerland

C. Pfleiderer
- M2S 8th International Conference on Materials and Mechanisms of Superconductivity and High-Temperature Superconductors, National Advisory Committee, Dresden
- Freunde der Physik an der Technischen Universität München e.V., Schriftführer
- Münchner Physik Kolloquium, Koordinator des Physik-Department
- Gemeinsames Festkörperkolloquium von Physik-Department, Walter-Meissner Institut und Walter-Schottky Institut, gemeinsame Organisation mit den Dozenten der Physik

K. Schreckenbach
- Advisory group, OPAL, Australia
- Chairman of the "Expert Advisory Comittee" at the Institut Laue Langevin, Grenoble

B. Schillinger
- Board Member of the International Society for Neutron Radiography
- Secretary of the European Society for Neutron Radiology

7.7 Accomplished PhD Theses

Angelika Elhardt	Aktivitätsbestimmung von Gamma-Emittern in grossvolumigen Objekten
Verena Kargl	Magnetic Properties of Low Dimensional Spin Systems
Sven Krimmel	Limited View Angle Tomography for Single Material Objects in Non-Destructive Testing with X-rays
Daniel Lamago	Critical Magnetic Fluctuations in Localized and Itinerant Magnets Studied by Neutron Scattering
Christian Schanzer	Investigation of Interlayer Exchange Coupling in Ferro-/Antiferro-/Ferromagnetic Trilayers
Nico Wieschalla	Out-Of-Pile Examination of the High Density U-Mo/Al Dispersion Fuel

7.8 Accomplished Master's Theses

Thomas Brunner	Spektrometer zur Untersuchung der temperaturabhängigen Positroniumbildung und materialabhängigen Moderationseffizienz
Rainer Jungwirth	Thermische und elektrische Leitfähigkeit hochdichter Uran-Molybdän Kernbrennstoffe
Stefan Legl	Aufbau eines Time-of-Flight-Spektrometers zur Analyse Positronenannihilaion-induzierter Auger-Elektronen
Jakob Mayer	Durch Positronenannihilation induzierte Auger-Elektronenspektrosskopie an Kupfer und Silizium
Andreas Neubauer	Hall-Effekt und Magnetwiderstand schwach magnetischer Metalle
Dominik Streibl	Aufbau und Test eines MIEZE-Setups an RESEDA

7.9 E21 Members

Phone/Fax: +49-89-289- PH: Physics Department, RS: Reactor Station

Name	Phone	Fax	Room	email
Arend Nikolas, Dipl. Phys.	-12180	-14997	RS, 124a	Nikolas.Arend@frm2.tum.de
Böni Peter, Prof. Dr.	-14711	-14713	PH 1, 2215	Peter.Boeni@frm2.tum.de
Böning Klaus, Prof. Dr.	-12150	-12191	FRM-II, UBA 0325	Klaus.Boening@frm2.tum.de
Brunner Thomas, Dipl.-Phys.	-12129	-14620	Flachbau 10	Thomas.Brunner@frm2.tum.de
Bundschuh Ralph, Dipl. Phys.	+49-89-41404570	+49-89-41404938	Klinik für Nuklearmedizin Ismaninger Str. 22 81675 München	Ralph.Bundschuh@ph.tum.de
Engelhardt Martin, Dipl. Phys.	+49-89-636-48051	+49-89-636-53810	–	zfp.student@mchp.siemens.de
Gläser Wolfgang, Prof. emerit.	-12476	-12474	PH 1, 2227	wglaeser@ph.tum.de
Hils Thomas, Dr.	-14721	-14724	PH 1, 2048	thomas.hils@hils-consult.de
Janoschek Marc, Dipl. Phys.	-14725	-14724	PH 1, 2373	marc.janoschek@psi.ch
Jones Sylvia, Secretary	-14712	-14713	PH 1, 2217	Sylvia.Jones@frm2.tum.de
Jungwirth Rainer, diploma student	-12515	-14724	PH 1, 2373	Rainer.Jungwirth@frm2.tum.de
Krimmel Sven, Dipl. Phys.	+49-89-636-45791	+49-89-636-53810	–	xray.external@mchp.siemens.de
Legl Stefan, Dipl. Phys.	-14740	-14724	PH 1, 2207	Stefan.Legl@frm2.tum.de
Löwe Benjamin, diploma student	-12161	-14620	Flachbau 10	Benjamin.Loewe@frm2.tum.de
Lorenz Klaus, Dipl. Phys.	-14741	-14997	RS, 146b	Klaus.Lorenz@frm2.tum.de
Mantwill Andreas, Mechaniker	-14887	–	–	–
Mayer Jakob, Dipl. Phys.	-12137	-14620	Flachbau 11	Jakob.Mayer@frm2.tum.de
Morkel Christoph, Dr. habil.	-12157	-14724	PH 1, 2373	Christoph.Morkel@frm2.tum.de
Mühlbauer Martin, Dipl. Phys.	-12106	-14997	RS, 125a	Martin.Muehlbauer@frm2.tum.de
Mühlbauer Sebastian, Dipl.-Phys.	-12515	-14724	PH 1, 2373	Sebastian.Muehlbauer@frm2.tum.de
Neubauer Andreas, Dipl. Phys.	-12512	-14724	PH 1, 2367	Andreas.Neubauer@frm2.tum.de
Niklowitz Philipp, Dr.	-14722	-14997	PH 1, 2207	Philipp.Niklowitz@frm2.tum.de
Pfleiderer Christian, Prof. Dr.	-14720	-14713	PH 1, 2206	Christian.Pfleiderer@frm2.tum.de
Pikart Philip, diploma student	-12161	-14620	Flachbau 10	Philip.Pikart@frm2.tum.de
Piochacz Christian, Dipl. Phys.	-12179	-14997	Flachbau 10	Christian.Piochacz@frm2.tum.de
Qi Ning	-12299	-14620	Flachbau 14	ning.qi@frm2.tum.de
Reingen Gabriel, Mechaniker	-12656	–	PH 1, 1321	–
Ritz Robert, diploma student	-12515	-14724	PH 1, 2373	Robert.Ritz@frm2.tum.de
Russ Barbara, Dipl. Ing.	-14717	-14713	PH 1, 2207	Barbara.Russ@frm2.tum.de

Phone/Fax: +49-89-289- PH: Physics Department, RS: Reactor Station

Name	Phone	Fax	Room	email
Schreckenbach Klaus, Prof. Dr.	-12183	-14713	PH 1, 2201	Klaus.Schreckenbach@frm2.tum.de
Schulz Michael, Dipl. Phys.	-14718	-14997	RS, 125a	Michael.Schulz@frm2.tum.de
Stadlbauer Martin, Dipl. Phys.	-14631	-14620	Flachbau 10	Martin.Stadlbauer@frm2.tum.de
Wieschalla Nico, Dipl. Phys.	-12111	-14997	RS, 124	Nico.Wieschalla@frm2.tum.de

7.10 Associated Members at FRM-II

Phone/Fax: +49-89-289- PH: Physics Department, RS: Reactor Station

Name	Phone	Fax	Room	email
Calzada Elbio, Dipl. Ing.	-14611	-14997	RS, 126	Elbio.Calzada@frm2.tum.de
Georgii Robert, Dr.	-14986	-14989	NL-Halle, UYH 0336	Robert.Georgii@frm2.tum.de
Häußler Wolfgang, Dr.	-14921	-14989	NL-Halle, UYH 0334	Wolfgang.Haeussler@frm2.tum.de
Hugenschmidt Christoph, Dr.	-14609	-14620	Flachbau 9	Christoph.Hugenschmidt@frm2.tum.de
Röhrmoser Anton, Dr.	-14890	-14995	FRM-II, UYH 0328	Anton.Roehrmoser@frm2.tum.de
Schillinger Burkhard, Dr.	-12185	-14997	RS, 127	Burkhard.Schillinger@frm2.tum.de
Schwikowski Reinhard, Techniker	-14915	-14995	NL-Halle, UYH 0336	Reinhard.Schwikowski@frm2.tum.de

PH: Physics Department
RS: Reactor Station

7.11 Guests

Phone/Fax: +49-89-289- PH: Physics Department, RS: Reactor Station

Name	Phone	Fax	Room	email
Gähler Roland, Dr. habil.	+33-4-7620-7189	+33-4-7648-3906	–	gahler@ill.fr
Keller Thomas, Dr.	-12164	-14997	RS, 106	Thomas.Keller@frm2.tum.de

PH: Physics Department
RS: Reactor Station

7.12 Guest Scientists

Name	Institute	Duration of stay
Volkov, Nikita, Dr.	Kirensky Institute of Physics SB RAS, Russia	May 2006

7.13 Guest Students

Name	Institute	Duration of stay
Schwab, Adele	MIT, USA	May 2006 – August 2006
Kung, Kevin	Princeton, USA	June 2006 – August 2006
Henry, Edward	Harvard, USA	August – September 2006
Williamson, Paul Nahai	Warwick, UK	August – September 2006

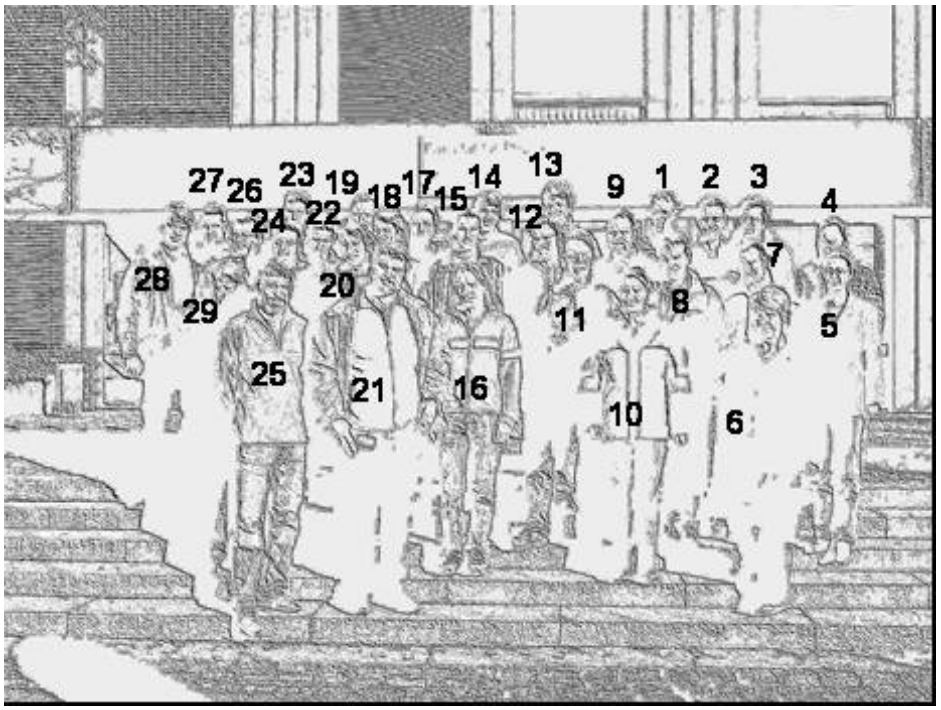

1	P. Böni	9	K. Schreckenbach	17	B. Löwe	25	E. Calzada
2	P. Pikart	10	S. Jones	18	S. Mühlbauer	26	R. Jungwirth
3	R. Georgii	11	R. Repper	19	C. Morkel	27	N. Arend
4	M. Mantwill	12	C. Piochacz	20	A. Neubauer	28	C. Pfleiderer
5	N. Qi	13	T. Brunner	21	B. Schillinger	29	W. Häussler
6	B. Russ	14	J. Mayer	22	S. Legl		
7	M. Stadlbauer	15	M. Mühlbauer	23	P. Niklowitz		
8	C. Hugenschmidt	16	M. Schulz	24	R. Ritz		

Missing: K. Böning, R. Bundschuh, M. Engelhardt, W. Gläser, T. Hils, M. Janoschek, K. Lorenz, G. Reingen, N. Wieschalla, A. Röhrmooser, R. Schwikowski, R. Gähler, T. Keller

7.14 Guided Tours at FRM-II

The FRM-II is open for everybody to come and visit the scientific and experimental facilities (Experimental Hall and Neutron Guide Hall). Therefore, Guided Tours are organized by a specially established division, the „Besucherdienst“, and conducted by the scientists and the technical personnel of FRM-II.
In 2006, the members of E21 guided approx. **140** officially registered tours and several others at various occasions, thus contributing a significant amount of time and personal effort to help making the Neutron Source FRM-II a publically transparent and accepted research facility.

7.15 E21 Gallery

At the begining of 2006 Germany felt like Alaska. Two E21-PhD students found their own way of making the best of it...

...but finally when summer gave us a warm surprise, the members of E21 took every chance to enjoy nature – and a barbecue, of course...

E21 showing its foreign members and students a Bavarian tradition: Biergarten...

It was a hot summer! E21 enjoing a cool bath in a lake...

...followed by a cool beer in „Weihenstephaner Biergarten“

Waiting for Santa Claus on Dec. 6...

A cool guy, isn´t he?

Santa Clause is gone, time to discuss the year that has passed so quickly...